The
University
Of
Sheffield.

High Refractive Index Silicate Fibres for Cure Monitoring of Epoxy Matrix Composites

Peter R Wilson

Supervisors: Dr Simon Hayes and Professor Russell Hand

Dissertation submitted to the University of Sheffield in partial fulfilment of the requirements for the degree of:

Doctor of Philosophy

Material Science and Engineering

The University of Sheffield

March 2015

Abstract

Fibre evanescent wave spectroscopy (FEWS) cure monitoring has previously been demonstrated with reinforcing fibres using low refractive index epoxy systems. To enable sensing of a range of aerospace grade epoxy systems, chalcogenide fibres with high refractive index (RI) and a large infra-red (IR) transmission were used for FEWS cure monitoring. However, chalcogenides have low chemical durability and poor mechanical properties resulting in fibre fractures and degradation of the optical properties with time. The aim of the project was to produce a high RI silicate glass, suitable for near infra-red (1000-2500nm) FEWS cure monitoring all possible epoxy resin systems throughout the entire curing process, whilst maintaining mechanical properties suitable for reinforcement.

A range of alkali and alkali free silicate glasses and epoxy systems were produced and their refractive indices optically characterised using ellipsometry. The glasses were thermally analysed for the liquidus and fibre forming temperatures for fiberisation. A fibre up-drawing jig was constructed and custom glass fibres were drawn. The composition was then mechanically characterised, demonstrating mechanical properties similar to reinforcing fibres.

Subsequently, the fibres were embedded into sunflower oil, liquid epoxy systems and epoxy pre-preg systems. Sunflower oil systems demonstrated proof of FEWS sensing showing excellent peak correlation. Liquid epoxy systems were successfully cure monitored by FEWS. Pre-preg systems did not display FEWS peaks, but were monitored using light intensity.

Acknowledgments

First and foremost I would like to thank Professor. Russell Hand and Dr. Simon Hayes for their continued support, guidance and supervision over my PhD.

I would like to also give special thanks to Dr. James Meredith, Dr. Austin Lafferty, Dr. Olga Amariutei, Dr. Joel Foreman and Dr. Peter Bailey. I am grateful for all of their advice and input towards my academic career.

I am very grateful for my parents for continues support financially and emotionally throughout my studies. I would also like to thank my sister Kathryn for her guidance when I have needed it throughout my degrees.

A special mention goes to Dr. Emma Lethbridge for putting up with me throughout our PhD's. It's been difficult and fun but, we have made it.

My PhD would have been a significantly more complex task without the experience and practical know how of Ian Watts, Dr. Lisa Gardiner, Ben Palmier, Bev Lane, Frank Fletcher and Richard Kangley.

My thanks goes out to Leslie Lyons from Bentham optics .Ltd and Adam Holland from Horbia .Ltd for all of their technical advice.

Finally, I would like to thank Professor. Gerard Fernando and Dr. Biqiong Chen for my viva.

Contents

1 INTRODUCTION

1.1 Polymer matrix composites

Polymer matrix composites (PMC) are a set of materials comprising of two or more phases which are held together using a polymer matrix. PMC’s have many benefits, including: high strength to weight ratio [1], tailorable mechanical properties that further increase weight savings [1, 2], relatively low temperature manufacture [1, 3] (typically between 120 °C and 200 °C) and corrosion resistance [4]. These advantages have drawn many industries towards their use, including many safety critical industries producing load bearing parts.

PMC’s are usually reinforced using carbon, aramid or glass fibres, or a combination of these. Reinforcements are usually either short random fibres or long fibres which can be aligned into unidirectional fabrics or woven into many weave styles and geometries.

1.2 Polymer matrices

Polymer matrices can be either thermoplastic or thermoset. Thermoplastics are characterised as non-cross-linked. Upon heating they can melt and the polymer chains are free to form a new shape. This is beneficial for reprocessing, however, in general they lack the mechanical properties, in service temperatures and solvent resistance when compared to thermosetting materials. There are exceptions to the typical thermoplastic properties, such as polyether ether ketone (PEEK) which has exemplary mechanical and thermal properties of tensile modulus 4.1 GPa and glass transition of 143 °C for Victrex PEEK 150UF10 [5]. However, many of these high mechanical property polymers with rigid backbones are inherently difficult to process, due to high melt viscosities requiring processing conditions of 380-400 °C [5].

On the other hand thermosets are polymerised during their processing, resulting in highly cross-linked networks. Typically thermosets have good mechanical properties for example, epoxy resins on average have a Young’s Modulus 2-3.5 GPa and tensile strength 0.05-0.09 GPa [3] and solvent resistance however, they cannot be reprocessed [3]. Thermosets are beneficial from a processing point of view due to low viscosities enabling good wetting-out of the reinforcement, leading to a good fibre/matrix interface and a resulting excellent stress transfer [1]. As a result they have the ability to be formed into complex shapes before curing into the final component.

The most common thermoset families include polyesters, vinyl esters and epoxy resins. Epoxy resins are commonly used for reinforced polymer composites and high value products [3]. Consequently, for the rest of this thesis only epoxy matrices will be considered.

1.3 Epoxy resins

Cured epoxy resins are a family of thermosetting polymers in which the constituent monomers contain a section with a minimum of two oxirane/epoxy groups which react with a curing agent to form a 3D network. This fully cured system, results in relatively high mechanical, thermal and chemical resistance as previously stated, accounting for their worldwide popularity [3, 6]. The epoxy group or oxirane is a highly stressed polar ring, which due to the differing electronegativities of carbon and oxygen, produce electrophilic carbon atoms which can undergo ring opening reactions towards nucleophiles [6]. There are extensive lists of possible curing agents and epoxy resins; this leads to many combinations resulting in highly tailorable properties [3].

Epoxy resins are separated into two groups, glycidyl and non-glycidyl. The non-glycidyl or aliphatic resins contain no aromatic rings producing UV resistant systems with lower viscosity, but at a cost to mechanical properties. Glycidyl epoxies possess aromatic rings and oxygen ether bonds producing a rigid back bone such as, those in Diglycidyl Ether of Bisphenol A (DGEBA) shown in Figure 1. These aromatic rings and ether bonds are electron withdrawing making the glycidyl resins highly reactive, reacting with a wide range of curing agents producing excellent mechanical properties [6]. Due to their superior properties glycidyl resins be discussed from this point onwards.

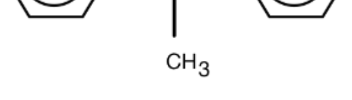

Figure 1 Diglycidyl Ether of Bisphenol A (DGEBA) [3]

1.3.1 Cure mechanism

Providing enough energy is supplied, usually in the form of heat, the reaction with an epoxy resin and a hardener occurs, initially forming oligomers and progressing to a highly branched molecule. This continues until the branched molecules have reacted into one macromolecule stretching across the entire sample; this is defined as the gel point. This highly branched macromolecule is no longer capable of being placed into solution and is a rubbery visco-elastic solid. From the gel point the sample continues to network until all the remaining small molecules have reacted and the sample is considered cured [3]. The curing process is shown in Figure 2:

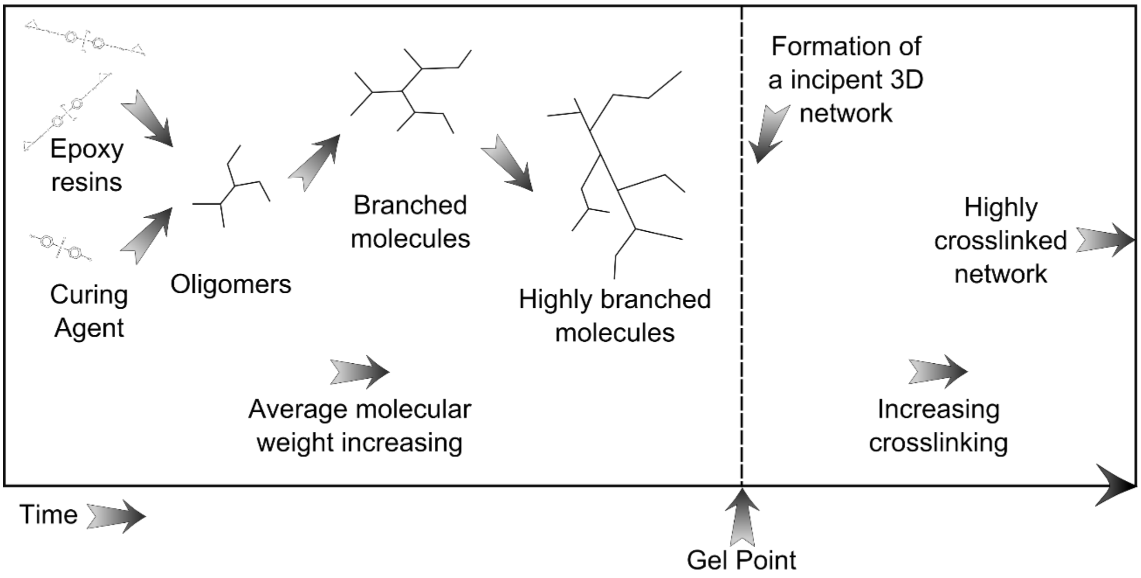

Figure 2 Progression of epoxy reaction

Post gel-point, the mobility of the reactants is inhibited due to an increase in viscosity preventing a high level of cure. To enable a high level of crosslinking and a resultant improvement in final properties, epoxy systems are post cured by heating the resin to a high enough temperature to enable maximum mobility of the un-reacted portions. Beyond this, in some systems the most favourable properties are achieved by producing non-stoichiometric epoxy to hardener ratios [7]. Usually an excess of epoxy is used, to produce a highly cross-linked system.

1.3.1.1 Amine cure

Amine cured resins make up the vast majority of epoxy curing agents [3]. Typically amine cures are a three part mechanism, as shown in Figure 3:

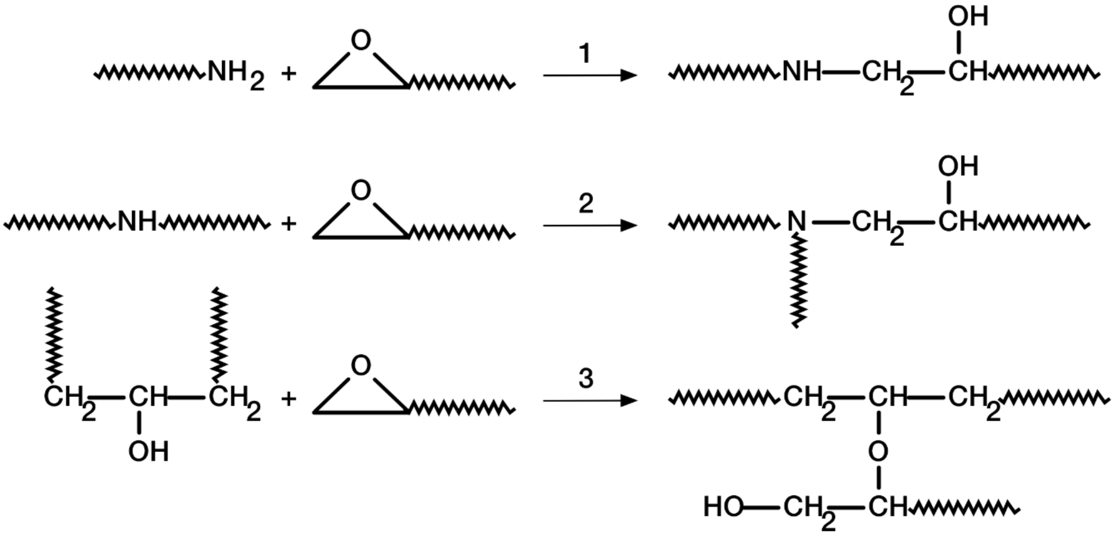

Figure 3 Reaction of amines with epoxy resins [3]

In the first step (1) the primary amine ring opens the epoxy group, bonding to the epoxy chain forming a hydroxyl group and producing a secondary amine. This secondary amine can then go on to ring open another epoxy group, forming another hydroxyl group and tertiary amine [3, 8]. To make the system into a full 3D cross-linked system, a di-amine and di-epoxide are used.

Post-initiation step, the reaction can be catalysed by a range of hydroxyl accelerators or hydrogen donors. As each epoxide reacts a hydroxyl group is formed, consequently the reaction is self-catalytic as shown in Figure 3 (3).

1.3.1.1.1 Amine blooming

Using low molecular weight amines is beneficial due to a tighter network formation, resulting in improved mechanical properties and chemical resistance [3]. However these low molecular weight amines can rise to the surface of the epoxy, producing an oily/whitened finish. This is caused by a mismatch of resin and hardener [3] and the resulting amine reacting with carbon dioxide in the atmosphere forming an ammonium carbonate [9]. This can be a real issue causing under curing due to a change in the stoichiometry, surface tackiness and the resulting surface is not ideal for painting [9]. This is normally minimised by increasing the molecular weight of the amine [3, 9].

1.3.1.2 Anhydride cure

Anhydride cured epoxies are less common than amine cures however, they boast good electrical insulating properties [8] and low shrinkage resulting in low residual stress [3]. There are a variety of anhydride curing techniques being either (a) uncatalysed or (b) catalysed as shown in Figure 4.

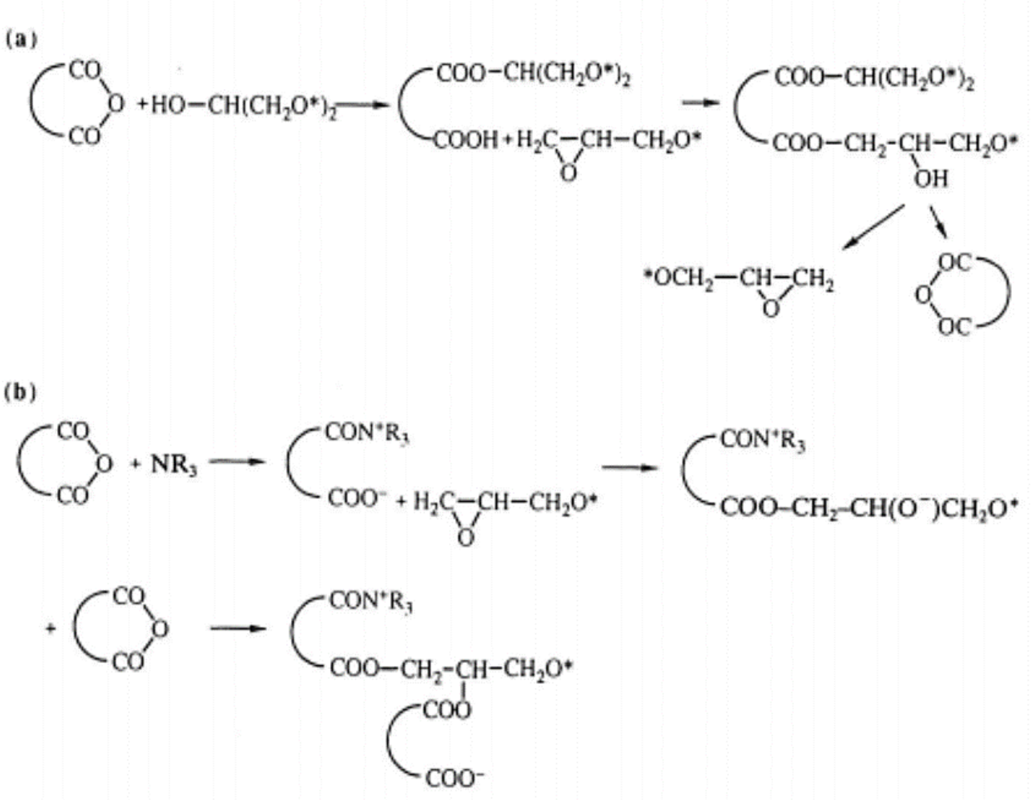

Figure 4 (a) Uncatalysed, (b) Catalysed anhydride epoxy reaction, R_3 denotes remaining side group of atoms [3]

In the uncatalysed version, a hydroxyl along the epoxy resin will react with the anhydride forming a half ester which results in a half ester carboxylic group. This can now react with the epoxy group resulting in a di-ester alcohol. The remaining hydroxyl group is now available to react with an epoxy or anhydride [3].

Catalysed versions can be used with tertiary amines, imidazoles or Lewis acids [3]. These ring open the anhydride, producing a carboxylate ion which react with epoxies. This forms an alkoxide esters which ring opens more anhydrides continuing the reaction with further epoxies [3].

1.4 Need for cure monitoring

The majority of PMC mechanical properties are dominated by fibre properties. Some of the properties such as interlaminar shear strength and unidirectional transverse strength are dominated by matrix properties which are affected by crosslink density [10, 11]. Many high performance epoxy systems require heat to initiate and sustain the reaction and post cure the resin, meaning that early removal of the system will prevent the resin from fully reacting producing sub optimal performance. Therefore, the certainty of cure is of the upmost importance for use in structural and safety critical applications. To add to the problem, many structural PMCs are produced in thick laminates leading to thermal gradients and non-uniform cures [12]. As a result the components may be subjected to conservative processing, involving longer cure dwells and higher than necessary temperatures leading to higher residual stresses [13], potential for exothermic reaction and a resulting economic disadvantage [14]. To negate the issues of cure, many methods have been investigated to add certainty of cure and the progression towards cure systems with feedback controls, giving economic advantages and certainty to the final components [15].

1.5 Project Aims

Part 1: The aim of the project is to produce a glass with the following criteria:

- Sufficiently high refractive index, enabling light guiding in all epoxy resins throughout the full curing process.
- Possess a transmission window to enable monitoring of curing peaks in epoxy resins.
- Non-toxic constituents, with minimal environmental impact.
- Must be able to for form continuous fibres using convention processing.
- Suitability for integration in PMC
    - Mechanical properties suitable for reinforcement.
    - Aim for a similar chemical durability to current E-glass fibres.

To achieve the goals set out above, the RI of a range of epoxy matrices will also be tested as a minimum glass RI.

Part 2: To practically demonstrate the novel FEWS sensors using a range of chemicals, epoxy resins and commercial pre-preg systems.

2 LITERATURE REVIEW

2.1 Cure monitoring techniques

Modern scientific laboratories have many powerful analysis techniques to assess cure of resins, such as [12]:

- Differential scanning calorimetry (DSC)
- Fourier transform infrared spectrometry (FTIR)
- Rheometry
- Dynamic mechanical thermal analysis (DMTA)

However, all of these techniques require expensive equipment, involving either destruction of the component or removal of resin from a curing system making them unsuitable for in situ cure monitoring [10]. Due to the heat generation during epoxy cure, examination of small quantities of resin do not reproduce the bulk curing thermal condition, producing inaccuracies in the cure state measurement. For real time processing the cure has to be monitored via a change which occurs during the cure of a resin including: density, resonant frequency, optical response - either spectrum or refractive index, induced strain, thermal response or viscosity. Current practical solutions to in-situ cure monitoring of PMCs include [12, 15]:

- Dielectric monitoring
- Acoustic emission
- Ultrasonic monitoring
- Thermal monitoring
- Fibre optic methods:
    - Intensity-based (self-sensing)
    - Fresnel reflector
    - Strain measurement
        - Interferometric sensors (Fabry-Pérot)
        - Fibre Bragg Grating (FBG)
    - Spectroscopic techniques
        - Extrinsic optical fibre spectrometers
        - Fibre evanescent wave spectroscopy

Each of the cure monitoring techniques have their own advantages and disadvantages. Dielectric cure monitoring can produce results on the state of cure, void content and flow front in resin transfer moulding (RTM) moulds [14]. Despite these promising results integrated sensors can only determine localised cure state and, due to permanent integration, they can act as a stress concentrator through life. The technique can also produce inaccurate results when using conductive fibres such as carbon fibres, or the addition of water as a by-product or moisture ingress [15]. They are limited by electromagnetic interference [12, 16]. Despite these limitations when integrated into reusable RTM moulds, dielectric cure monitoring is a convenient cure monitoring technique.

The response from acoustic emission varies with the stiffness of the panel and consequently as the panel cures it stiffens and information about the gel point and degree of cure can be determined. If the materials acoustic response is already known, then further information can be drawn on the PMCs densification and residual stress [15]. Acoustic methods are heavily limited by the requirements that the curing part requires free vibration of the specimen. Ultrasonic methods, in a similar manner, can determine the state of cure through mechanical properties. However, they are limited via the difficulty of coupling with the curing panel [15] the requirement of a database of correlated studies to infer the chemical state of the resin [17]. This combined with limited environmental ranges such as high temperatures [18] prevents the use of ultrasonic cure monitoring.

Thermal cure monitoring involves the use of thermocouples, infra-red thermometers and thermal imaging systems. By monitoring external baseline temperatures exotherms can accurately be determined providing a curing point [14]. This technique is simple to implement for point thermocouples however, this limits the technique to resin systems where no external heat is applied which would mask results by the oven/autoclaves controller maintaining a static temperature.

2.2 Optical fibre sensing

A multitude of optical fibre sensors (OFS) have been investigated for cure monitoring of PMCs. This is due to their simple integration into a PMC, immunity to electromagnetic interference [4, 11, 19] preventing expensive protection and use in harsh chemical environments [20]. Fibres inherently lend themselves to integration into PMC causing minimal impact on the final mechanical properties [4, 11]. The integration can also be tailored to certain sections with a wide sensing capacity and, when integrated with computer controlled systems, components can be mapped out using fibres giving expansive spatial data about the component.

Throughout the rest of this thesis only optical sensing techniques and the relevant theory will be discussed.

2.2.1 What is light?

Currently, light and all of its phenomena cannot be fully explained using a single unified theory however, the closest theory is quantum electro dynamics. It is known that light is a particle not a wave or ray however, using a variety of theories, a practical explanation of many of light's phenomena can be derived [21]. Geometrical optics are best suited for macroscopic cases [22], whereas electromagnetic wave theory explains colour and polarisation of mediums, and quantum mechanics explains the interaction of light with atoms [22-24]. Consequently the most relevant theory will be used for each phenomenon.

2.2.2 Reflection, refraction, total internal reflection and fibre optics

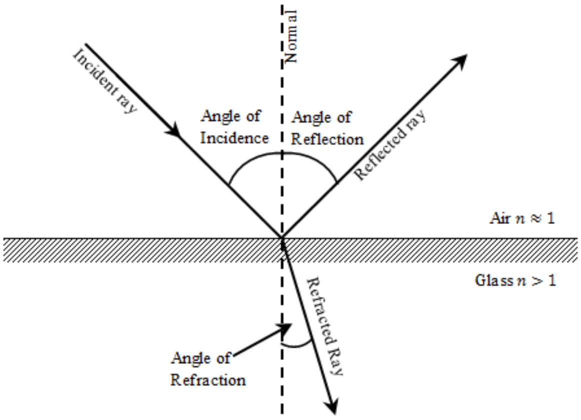

Figure 5 Ray diagram of an incident beam, reflecting and refracting on a glass sheet. Diagram redrawn and modified by author from reference [24]

When light falls upon a transparent material some of the light is reflected and some of it is refracted and transmitted as shown in Figure 5. From a quantum mechanical approach to reflection and refraction, it is still unknown why a photon refracts or reflects [21].

However, geometric optics can describe the phenomena. Reflectivity is given by [22, 24]:

$$R = \left(\frac{n_a - n_b}{n_a - n_b} \right)^2 \quad \textbf{(1)}$$

where n_a and n_b are the refractive index of the transmission medium and reflecting medium respectively [21,23]. As light propagates through a material it is absorbed or scattered and the waves velocity will be retarded [23]. This retardation is measured as a ratio of light traveling through a vacuum versus the light through a medium which results in a unitless value known as the refractive index (RI) [23, 24].Refraction is the bending of light which occurs when light propagates through a refractive index change. This is described using Snell's law [21,23]:

$$n_a \sin\theta_a = n_b \sin\theta_b \quad \textbf{(2)}$$

As light propagates through a high refractive index medium to a low refractive index medium it bends away from the normal. As this angle of interception increases it eventually reaches an angle called the critical angle where the transmitted light propagates along the interface. Beyond this critical angle the light is reflected back in to the high refractive index medium. This phenomenon is known as total internal reflection (TIR) and is demonstrated in Figure 6.

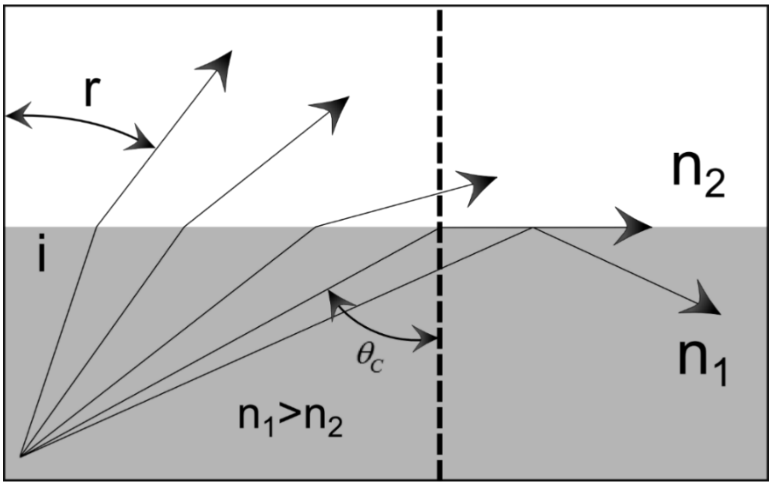

Figure 6 Diagram demonstrating the bending of light away from the normal, until the critical angle is attained causing total internal reflection. Diagram redrawn and modified by author from references [24, 25]

Fibre optics operate using the principal of TIR; where light enters a central high refractive index core and propagates via TIR from a low refractive index cladding.

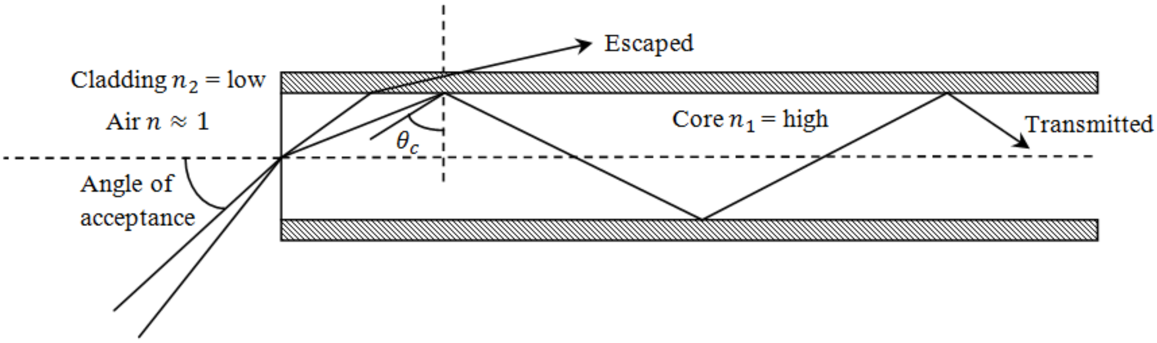

Figure 7 Diagram showing the operation of an optical fibre and its acceptance angle. Diagram redrawn and modified by author from references [12, 23-27]

As demonstrated in Figure 7, TIR only occurs beyond the critical angle; hence rays > θ_c are total reflected and bound whilst rays < θ_c are partially refracted and will attenuate along the fibre. This couples with the refraction of the incoming wave as it moves from air to the core and leaves us with an angle of acceptance. This angle of acceptance gives a cone of rays which will be transmitted. More commonly, the angle of acceptance is stated as the numerical aperture (NA) given by the following relation [24]:

$$NA = \sin(\text{Acceptance angle}) = \sqrt{(n_1^2 - n_2^2)} \qquad \textbf{(3)}$$

where n_1 and n_2 are the refractive index of the core and cladding respectively. Hence, to acquire the highest efficiency and luminous power the difference between n_1 and n_2 should be as large as possible.

The rays which enter the optical fibre at differing angles are described as modes and are split into three categories: guided, leaky, and radiation modes, where guided modes are the modes which are transmitted. The modes in a fibre can be described by a unit less quantity, the normalised frequency or V number [27].

$$V = \frac{2\pi a}{\lambda} NA \qquad \textbf{(4)}$$

Where a = fibre diameter. From the equation it is clear that the larger the NA and a and the smaller the wavelength, the larger the number of modes guided by the fibre. Modes are an important factor in high speed communications due to each mode having a different path length resulting in a pulsed light spread out [24, 27]. Optical communication fibres have controlled diameters producing a V number < 2.405 which allows only the single fundamental mode, this is known as a mono mode fibre [28].

If a fibre optic cable is bent the conditions for TIR change such that the critical angle becomes shallower around the bend and some of the propagating light no longer obeys the conditions for TIR. Hence such rays escape from the fibre. Bending losses can occur on both a macroscopic and microscopic scale [28].

Within multimode fibre optics bending losses cause some of the modes to escape. Consequently, when measuring light intensity in-situ it is possible to detect which fibres have undergone bending. Macroscopic bending losses are given by [28]:

$$BL \propto \exp\left(-\frac{R}{R_c}\right) \tag{5}$$

where BL= bending losses, $R =$ radius of curvature of the fibre and $R_c =$ critical radius given by [28]:

$$R_c = \frac{a}{\left(n_1^2 - n_2^2\right)} \tag{6}$$

2.2.3 Epoxy / glass fibre refractive index mismatch

Epoxy resins have a range of RI values from 1.55 [29] to 1.63 [30] depending on composition of the resin system. Calcium aluminosilicate glasses are commonly used for reinforcing fibres [31-35]. Reinforcing glasses have a high silica content and low levels of polarisable elements, consequently they have low refractive indices, such as commonly used boron free E-glass fibres (Advantex) at 1.561 [32, 33]. Other commonly used reinforcing fibres are shown in Table 1. When incorporating optical fibres into epoxy resins for sensing techniques, the fibre RI > epoxy RI to maintain TIR within the fibre. As a result when optical fibres are incorporated into PMC, specialist glasses, cladded glasses or modified resin systems are required if they are used as optical fibres.

Table 1 Optical and mechanical properties of regularly used reinforcing glass fibres [32, 33]

	Advantex	**AR-glass**	**C-glass**	**D-glass**	**E-glass**	**E-CR-glass**	**R-glass**	**S2-glass**
Density g/cm^3	2.62	2.70	2.52	2.11	2.55-2.62	2.68-2.72	2.54	2.48
RI n_D	1.561	1.562	1.533	1.465	1.558	1.574-1.576	1.546	1.521-1.525

2.2.4 Fibre diameter mismatch

Many traditional fibre optic systems work on a 125-230 µm diameter which when compared to composite reinforcing fibre diameters of 7-14 µm, produce a large fibre diameter mismatch when integrating standard optical fibres into PMCs [20, 36, 37]. This diameter mismatch acts as a stress concentration due to the OFS displacing the reinforcing fibres giving rise to resin-rich regions around the OFS [36, 37]. Within studies it has generally been found that tensile strength and stiffness have been equivalent to samples without OFS. However, the compressive strength and stiffness have been reduced due to the large diameter OFS [36, 37] and this needs to be considered when designing PMC with integrated OFS.

2.2.5 Strain inferred cure monitoring

Fibre Bragg gratings (FBG) and extrinsic Fabry-Perot interferometers have been a popular choice of OFS for PMCs. They have been demonstrated in a wide expanse of PMC sensing technologies including structural health monitoring, residual stress measurements and the cure monitoring can be in the form of temperature and processing pressures [15, 38, 39]. Unsurprisingly, aerospace and civil companies are currently incorporating FBG into their PMCs, despite their current geometry mismatch [22, 40]. However, this has led to the development of 40 µm diameter FBG [41].

Strain measurement devices are very beneficial providing data beyond the cure monitoring process however, FBG sensors are affected by both strain generation during cure and heating occurring which limits their applications. Beyond this they can only infer cure of PMC by strain generation. There are arguments for inference of cure for a well-known system being adequate however, for accurate data other optical techniques are more promising.

2.2.6 Intensity and self-sensing composites

Intensity-based systems rely upon a simple system of a large change in resin RI whilst it cures and gels [11, 16]. By utilising a fibre with a suitable RI i.e. high enough that the uncured resin will act as a cladding, light can be transmitted through the fibre. As the resin cures its RI increases causing a decrease in number of modes and the numerical aperture resulting in an overall intensity drop. Consequently the intensity drop can be related to the state of cure.

When reinforcing glasses are used with a suitable resin system the intrinsic optical properties of the glass fibre are utilised. This is known as self-sensing. Self-sensing in general uses the intrinsic material properties to sense phenomena and provide a functionality to the material at minimal extra cost, limited change to the original design inhibiting loss of mechanical properties, and providing a large sensing volume [42, 43]. Self-sensing has been performed using both glass and carbon fibre composites which have developed into large research topics [17, 25, 29, 42, 44-48].

In general, intensity based systems do not give absolute values for cure, and can be affected by strain and temperature. However, when absolute values are not required, intensity based systems offer financial advantages [36].

2.2.7 Fibre optic sensors designed for Infra-red spectroscopy

All of the previous optical techniques work via an inference of cure rather than direct analysis on a chemical level. There are two spectroscopic fibre optic techniques, extrinsic optical fibre spectroscopy and fibre evanescent wave spectroscopy which can chemically analyse cure. Spectroscopic techniques study the interaction of materials with radiated energy. Infra-red interacts with the natural vibrations and rotations of molecular bonds [49, 50], therefore, using infra-red spectroscopy on a curing epoxy system the ratio of remaining bonds within the sensing volume can be determined. This allows quantification of the level of cure over the sensing region at the molecular level.

The fundamental wavelengths given from epoxy and amine groups reside within the mid infra-red range 2500 nm-50000 nm however, these peaks are very intense, broad and overlapping, which can cause difficulty in interpretation. The harmonics of these fundamental peaks reside in the near IR (NIR) from approximately 780 nm-2500 nm and are narrower allowing for quantitative measurements [12]. These overtone absorptions relate to higher order quantum vibrational states which are more unlikely and consequently weaker however, this can be beneficial allowing for larger thicker samples to be used than that of mid infra-red (MIR) spectroscopy [6, 8, 51].

2.2.7.1 Single fibre transmission sensor

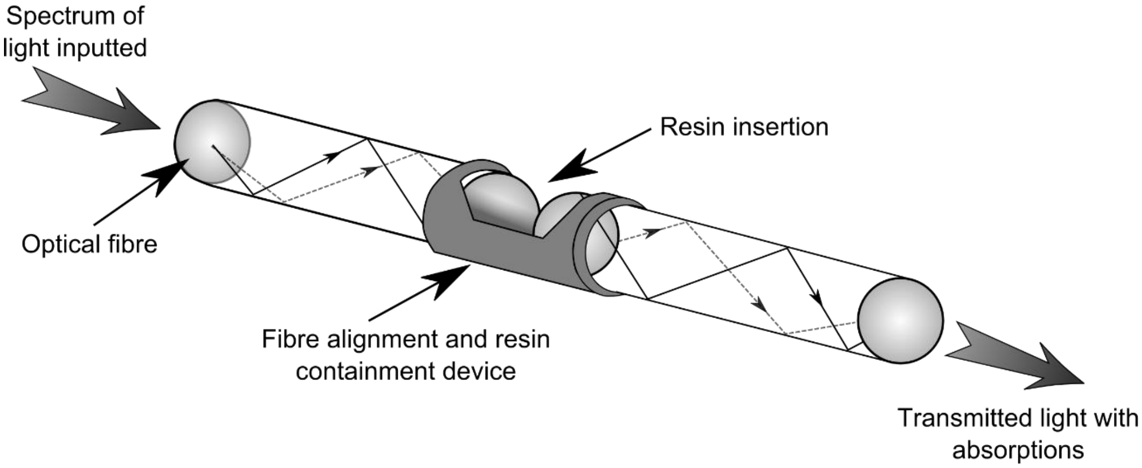

Figure 8 Single fibre transmission sensor. Diagram redrawn and modified by author from reference [12]

This technique involves two fibres with a gap placed between the fibre ends [12, 52]. The resin then enters the cavity between the fibre ends as shown in Figure 8. Using a spectrometer, a spectrum can be obtained through the fibre, then the resin and then through the second fibre to the detector. When using infra-red light, vibrational peaks within the resin can be detected and analysed through the cure process [53]. This technique also gives quantitative data however, the sensor relies on good fibre alignment and the protection of the sensor, using a capillary can act as a stress concentrator through the life of the PMC. To overcome these issues laser ablation has been used to create cavities in the fibres. This has enabled evanescent wave spectroscopy and Fabry-Perot interference fringes, adding further functionality to the sensor [12]. Although this technique produces excellent spectroscopic data, the fibres are inherently fragile and can only sense a small region of resin.

2.2.7.2 Fibre evanescent wave spectroscopy

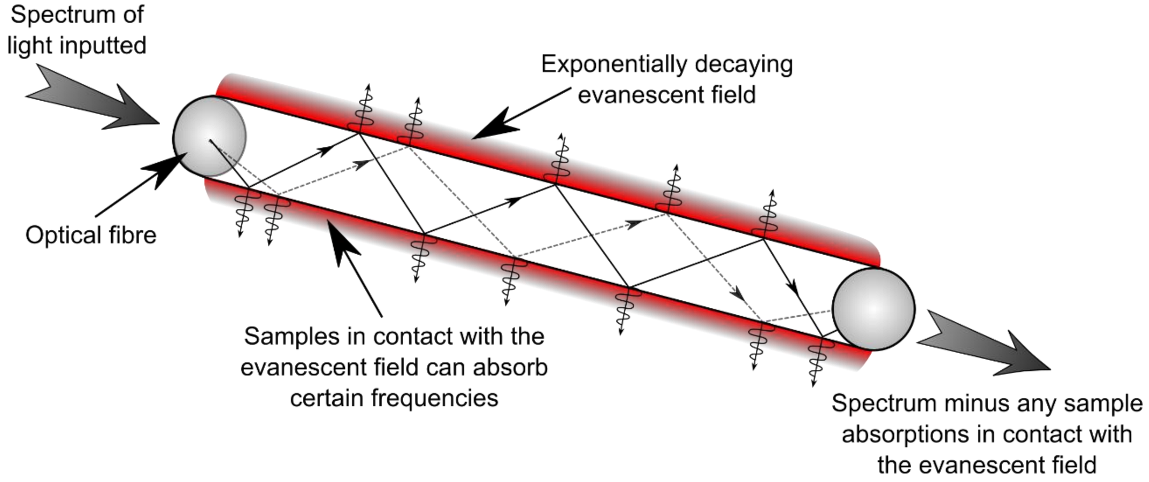

Figure 9 A partially unclad fibre optic cable demonstrating the evanescent wave forming at the surface. Diagram redrawn and modified by author from reference [12]

Fibre evanescent wave spectroscopy (FEWS) exploits the evanescent wave which forms at the surface of an optical fibre as long as the laws of total internal reflection are obeyed. The evanescent wave is an exponentially decaying standing wave which is formed at the interface between the fibres core and the lower refractive index medium as a function of distance from the core [10, 54] as shown in Figure 9. As a result to analyse the curing of an epoxy resin system a region with no cladding must be present [4]. Consequently, the refractive index of the fibres must be higher than the resin system being analysed to maintain the conditions for TIR and the formation of the evanescent field. However, if an unclad fibre is used the resulting evanescent wave flows over the entire length producing a large surface-to-volume sensing capacity [55].

If the evanescent wave penetrating the epoxy system matches the vibrational frequency of the molecule the light will be absorbed [56]. By scanning a spectrum of light through a suitable fibre embedded in a curing epoxy resin the functional groups will absorb at their specific frequency removing the energy from the total transmitted wave [57]. As a result as the curing reaction progresses and the reactants are used up and new functional groups are produced the total absorptions in the spectrum will change with respect to time. This will then give the state of cure beyond the boundary of the fibre [12, 54, 55].

2.2.8 Optical absorptions of glasses

To spectroscopically analyse a curing epoxy resin within a composite, the light will have to transmit through an optical medium. Consequently, the absorptions of this medium, which will be glass, are of the upmost importance providing a sensing window. Glasses with only small absorptions in the bulk produce a significant issue in optical fibres due to length of transmission.

Infra-red absorptions can arise for a variety of reasons as characterised by Shelby *et al*, [35] such as:

- Impurities
- Infra-red cut off (Multiphonon edge)

The impurities can be either gasses trapped/dissolved during manufacture or bound hydrogen isotopes. Diatomic gasses do not normally absorb in the IR, however, weak absorptions due to H_2 can be found in silicates around 2420 nm and a harmonic overtone at 1240 nm, varying a small amount with composition [35].

The multiphonon edge is an intense edge made up of overtones or fundamental absorptions which occur due to the vibrations between anions and cations. The frequency of their vibrational absorption is given by [35]:

$$\upsilon = \left(\frac{1}{2\pi}\right)\sqrt{\frac{F}{\mu}} \text{ where } \mu = \frac{m_1 m_2}{m_1 + m_2} \qquad \textbf{(7)}$$

υ = frequency of vibrational absorption, F= Force constant on the bond, μ= reduced mass of molecule where m_1 and m_2 are the masses of the two atoms. This demonstrates weak bonds with large atoms will have higher IR cut off points.

Chalcogenides are a family of non-oxide containing glasses i.e. S, Se and Te which, due to the replacement of oxygen with heavier elements, transmit significantly further into the infra-red spectrum than silicate glasses [35]. Conversely, in silicates the addition of transition metals and hydroxyl ions from either the batch or from moisture produce IR absorptions. However, it is difficult to predict the exact absorption spectrum without performing a scan of the glass [58].

The most common IR absorption in silicates is the Si-OH hydroxyl vibration. There is a lot of discussion in the literature with regards to the precise location of the hydroxyl vibration in silicates however, the general consensus is around 2722 nm (3673 cm^{-1}) to 2850 nm [35, 59-62].

Phase separations and flaws also give rise to absorptions leading to attenuation of the light. Density fluctuations, either micro or macroscopic, result in refractive index changes which leads to Rayleigh scattering attenuating the light [25].

To discuss this in greater detail the optical theory and processes surrounding the technology and other optical techniques used within the project will be considered.

2.2.8.1.1 Evanescent wave

The evanescent wave can be described using Maxwell's equations. When light is travelling in a high refractive index medium and it approaches the interface at the critical angle, as previously described in Section 2.2.2, it reflects. However, to satisfy the boundary conditions of Maxwell's equations the transmitted light cannot equal zero [22]. A range of experiments have been performed to demonstrate the existence of the evanescent wave and proofs are provided in reference [54].

This transmitted wave forms a non-propagating, exponentially decaying standing wave, perpendicular to the fibre with on average no energy transfer in the optically lower density medium; this is called the evanescent wave [12]. Frequently literature uses the term "on average no energy is transferred" which seems to suggest no energy transferred and hence no interactions can occur beyond the core of the optical fibre. However, extensive derivations show that energy is passed back and forth which results in a net zero transfer of energy [22]. The evanescent wave interacts with the reflected wave and as a result the reflected wave is determined by the interactions occurring beyond the fibre interface [57]. The penetration depth is given by [12, 54]:

$$d_p = \frac{\lambda}{\left[2\pi n_1 \left(\sin^2\theta - {}^{n_2}\!/\!_{n_1}{}^2\right)\right]^{1/2}} \qquad \textbf{(8)}$$

The equation demonstrates that as the fibre and claddings refractive index starts to match $n_2/n_1 = 1$, the penetration depth maximises. Furthermore, as the angle increases beyond θ_C, the field diminishes. Finally, as the wavelength increases, the penetration depth increases.

Area of interaction is determined by the number of reflections (N) [57].

$$N = \left(L/T\right)\cot\theta \tag{9}$$

Here, L=length, T=Thickness of waveguide and θ= angle of incidence. This corresponds to longer and thinner waveguides, having higher reflections and consequently greater evanescent wave interaction.

When referring to the optical fibre waveguide, this corresponds to the modes given by the V-number in section 2.2.2. Modes which travel far beyond the critical angle are tightly bound to the centre of the core and are known as high order modes; whilst modes approaching the critical angle, which travel slightly into the cladding, are known as low order modes. These mode types are also able to interact with each other, which in an absorbing cladding results in an energy loss [57].

The relation of power in the cladding of a fibre $P_{clad,}$ which is the evanescent field intensity, and the total power travelling is given by total power P_{total} [57]:

$$r = \frac{P_{Clad}}{P_{total}} = \frac{4}{3}\frac{\sqrt{2}}{V} \tag{10}$$

This indicates that as the V number increases the power in the cladding reduces. As stated in section 2.2.2, the V number depends on the radius of the fibre, the smaller the radius the smaller the V number. Consequently, the smaller the fibre diameter and the less modes can travel the greater the evanescent wave intensity [57].

2.2.8.1.2 Review of FEWS cure monitoring

Infra-red FEWS cure monitoring has been performed on epoxy systems using a wide array of glass fibres including: E-glass [63], chalcogenide [64, 65], borosilicate [16, 66], lead silicate [18], sapphire and zirconium fluoride glass [67] silver halide [68] flint-glass [69].

Chalcogenide glasses possess the ideal optical properties for FEWS of epoxy resins due to their larger more polar atoms, resulting in RI >2 [35] and a large IR transmission, as stated in section 2.2.8. Bailey demonstrated successful epoxy cure and moisture ingress monitoring however, due to the chalcogenide's low strength and chemical durability fibres were prone to fracture [55]. This was combated by using an organo-silane coupling agent which improved the matrix bond. Anne *et al* investigated a variety of chalcogenides with glass transitions >200 °C forming a central tapered fibre to promote the evanescent wave. These fibres produced successful cure monitoring throughout the mid infra-red [65]. Chalcogenide glasses offer the possibility of FEWS cure monitoring however, due to their inherent low glass transition <250 °C [65] and complex processing [55, 64, 65] these fibres are not currently commercially viable.

J.J. Kellar's group produced a range of papers utilising the evanescent wave sensors for investigation of interface chemistry between fibre and epoxy resin [69-72] and as a strain analysis technique using inherent density increases (RI increase) and fibre narrowing to resulting in a modal loss and intensity decrease in the NIR region [56]. These papers demonstrate excellent sensing capability producing an insight into interfacial chemistry however, they all varied from a realistic system either using specialist partially fluorinated resins with lower RI [70, 72, 73] or specialist flint-glass fibres [69, 72].

G. Fernando's group have publish a wide array of papers on FEWS cure monitoring of epoxy resins with correlation to other lab based cure monitoring techniques [10-12, 16, 17, 63, 74]. The paper from Wang *et al* was the first paper to the author's knowledge which utilised FEWS cure monitoring of epoxy resins with reinforcing E-glass fibres [63]. This also enabled damage sensing in the form of intensity based self-sensing beyond the FEWS cure monitoring. However, the RI mismatch between E-glass fibres and standard epoxy systems, as stated in section 2.2.3 prevents FEWS cure monitoring throughout the full cure. As a result a specialist low RI 1.52 epoxy resin EPO-TEK 310M is required. The use of such a resin significantly limits the range of applications for this system preventing analysis of the common epoxy systems.

All of the previously mentioned work has demonstrated successful FEWS cure monitoring of epoxies and given an insight into interphase chemistry. However, to achieve this either specialist fibres or resin systems were required. Specialist low refractive index resins are inconvenient due to great expense and limited use within structural applications. Many of the glass fibres are very inconvenient for real applications such as silver halide fibres which degrade in visible light with low thermal resistance [66]. Many of the other fibres are expensive such as sapphire fibres [66] or involve complex processing and lower mechanical and thermal properties than reinforcing fibres such as chalcogenide [64, 65]. Other fibres such as borosilicates and lead glasses are unsuitable for engineering applications due to low corrosion resistance [35] and optical fibre production routes which are inherently more expensive that reinforcing fibres.

2.3 Glass

A glass is a solid material which has no long range order. Theoretically any material can be placed in a glassy state by having a sufficiently rapid cooling rate preventing organisation of the atoms into an ordered crystalline structure. The cooling rate dependence gives rise to materials which readily form glasses and those which require external stimuli to prevent crystallisation. The most common glass formers are the inorganic glasses and for the rest of the thesis when discussing glasses, it will be referring to the inorganic glasses. Glasses are usually produced by mixing constituents together forming a glass batch. The constituents have varying roles within the glass formation and processing and can be broadly categorised as [35]:

- Glass former – Produces a network structure
- Flux - Usually alkali/alkali earths which break up the network (reducing the processing temperature)
- Property modifier - Modifies the glass structure to affect its properties
- Colorants - Usually 3D transition metals, affecting the final colour
- Fining agent – Removes bubbles from the melt

There are an infinite variety of glasses, to narrow the search down for a suitable glass composition for FEWS sensing the following topics will be covered:

- Glass fibre forming
- Refractive Index
- Chemical durability
- Mechanical properties

2.3.1 Glass fibre forming techniques

The processing of glass fibres is a highly developed field with a multitude of processing techniques such as [34]:

- Down drawing from melt
- Preform down drawing
- Up drawing

These processing techniques and varlets of them produce fibres for a variety of applications focusing on different properties.

For a glass melt to be fiberized it must be held at the fibre drawing viscosity without crystallising. The temperature which no crystals are formed in the melt for a set period of time (usually 24 hours) is known as the liquidus temperature [75]. The fibre drawing temperature typically lies between either viscosity of $\log(\eta/\text{Poise})=3$ or $\log(\eta/\text{Poise})=2.5$ [34, 76]. To reliably draw fibres the fibre forming point should be 50 °C higher than the liquidus [76].

2.3.1.1 Optical glass fibre production

Modern low-loss optical fibres are produced using chemical vapour deposition (CVD) due to the higher required purities [77]. Chemicals are purified before being deposited down a glass tube significantly reducing impurities [78]. A burner is then pasted down the tube solidifying the glass into a pure preform [35]. From here the preform can be drawn into fibres using a drop tower. This results in fibres with a significantly greater transmission lengths due to the removal of impurities [76].

2.3.1.2 Reinforcing glass fibre production

In comparison reinforcing fibres are commercially produced using a down-drawing technique, this can be done as a continuous process through a Pt alloy bushing from a melt or from a preform for smaller batches [31]. The down drawing technique is shown in Figure 10 where the batch composition is melted in a furnace, passed into a refiner and finally into the forehearth where the glass passes through a bushing and forms fibres. From here the fibres are usually cooled and coated with a sizing to protect the fibres minimising flaws. They are then wound onto a drum or chopped depending on the final application.

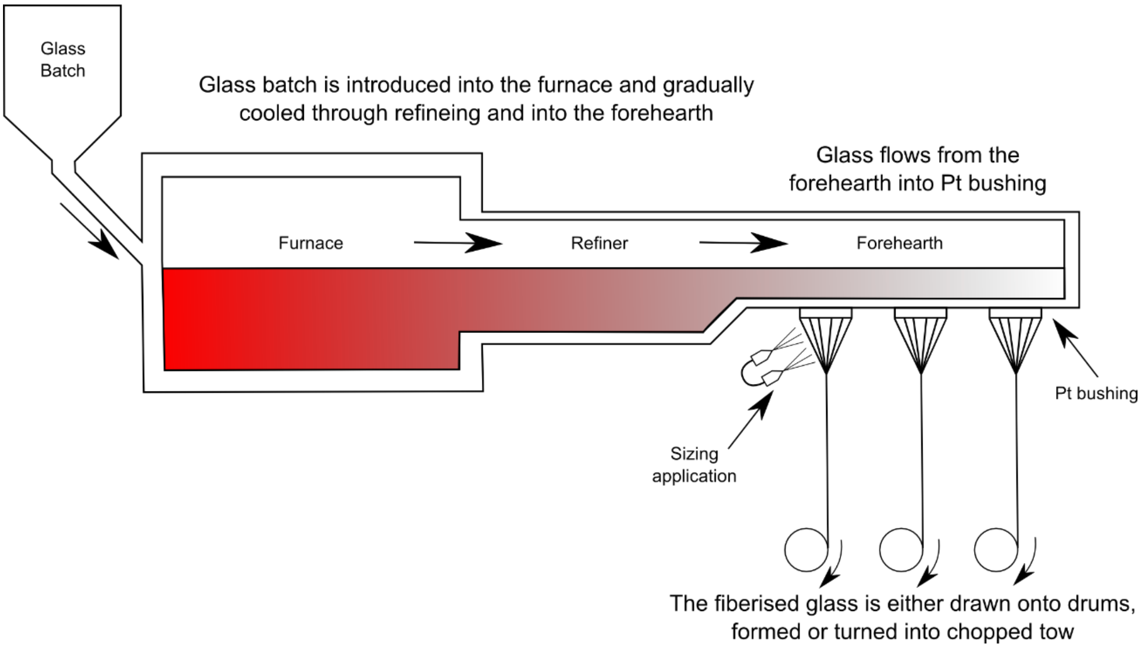

Figure 10 Diagram of a typical down drawing fibreisation furnace and haul off unit. Diagram redrawn and modified by author from reference [31]

Reinforcing fibres are produced on the large scale with little concern to the optical properties. As a result they are commonly optically limited by [25, 43]:

- Chemical impurities
- Density fluctuations
- Phase separations
- Presence of Flaws
- Imperfect cross sectional area

Consequently when reinforcing fibres are used for optical purposes they are inherently limited and it is impossible to acquire the same lengths of transmission as standard optical fibres [25, 43].

It was decided to focus on production techniques similar to standard reinforcing fibres. This was decided due to the cost of fibres and their eventual integration into PMC. One of the project aims is to produce a suitable glass for both optical properties and integration into PMC.

2.3.2 Light interaction with matter and the refractive index

RI is frequently stated as a real number however, it is actually a complex number given by [22, 24]:

$$\tilde{n} = n + ik \tag{11}$$

Where n is real part (absolute) RI, $\tilde{n}$ is the complex RI and k is the extinction/absorption coefficient [23, 24]. For transparent materials where absorption is negligible, the absolute index of refraction is given and the imaginary component is removed [22-24, 79]:

$$n = \frac{c}{v} \tag{12}$$

Where c = Speed of light in a vacuum and v = Velocity of light in the medium

Using the absolute refractive index we can derive Maxwell's relation [23]:

$$c = \frac{1}{\sqrt{\varepsilon_o \mu_o}} \tag{13}$$

$$v = \frac{1}{\sqrt{\varepsilon \mu}} \tag{14}$$

Where ε = absolute permittivity μ= absolute permeability. This gives [22-24]:

$$n = \frac{\sqrt{\varepsilon \mu}}{\sqrt{\varepsilon_o \mu_o}} = \sqrt{\varepsilon_r \mu_r} \tag{15}$$

Where ε_o= vacuum permittivity, μ_o = vacuum permeability, ε_r= dielectric constant (relative permittivity) and μ_r = relative magnetic permeability.

The magnetic components can be ignored for dielectrics due to electron magnetic moments not being able to move at the frequencies of light and most dielectrics are non-magnetic, hence relative magnetic permeability can be removed. This produces Maxwell's relation [22-24]:

$$n \approx \sqrt{\varepsilon_r} \tag{16}$$

This relation only holds true for the frequency range of visible light.

In order to relate the refractive index to the materials structure one must first relate the dielectric constant to the polarisability using the Clausius-Mossotti relation [79]:

$$\frac{\varepsilon_r - 1}{\varepsilon_r + 2} = \frac{N\alpha}{3\varepsilon_o} \qquad \textbf{(17)}$$

Where α = Polarisability of the material and $N =$ numbers of polarisable species per a unit volume of material. When applying the Clausius-Mossotti relation to a material with more than one type of polarisable species $N\alpha$ must be summed for such that:

$$N\alpha = N_1\alpha_1 + N_2\alpha_2 ...... + N_n\alpha_n \qquad \textbf{(18)}$$

The Clausius-Mossotti relation only holds true for isotropic (cubic) or amorphous materials with no permanent dipoles [24].

From a closer look at the origin of polarisability it is possible to see how RI is related to the Material's structure. The total/bulk polarisability of a material is made up of several contributions [24]:

- Electronic polarisability
- Ionic polarisability
- Orientation polarisability
- Space charge polarisability

When the electric field impinges on a material it induces dipoles. The dipole moment (p) is given by [24, 79]:

$$p = \alpha E_{loc} \qquad \textbf{(19)}$$

where E_{loc} is the local electric field given by [24, 79]:

$$E_{loc} = E_0 + E_1 + E_2 + ... + E_n \qquad \textbf{(20)}$$

The local electric field is comprised of the sum of the impinging wave (E_0) interacting with the induced waves in the surrounding material which are continuously interacting with other local waves ($E_1 + E_2 + E_n$) which are dependent on the dipoles (permanent or induced) and structural defects. Hence the magnitude of the dipoles in the material is dependent on their polarisability, their interaction with other surrounding dipoles, and the local electric field.

To acquire the net polarisation vector (P) all the dipoles moments must be summed [79]:

$$P = \sum_j N_j p_j = \sum_j N_j \alpha_j E_{loc} \quad \textbf{(21)}$$

where N_j species are summed with their α_j polarisabilities with an ever interacting E_{loc}.

In a static field all of the contributions of polarisation can contribute towards the polarisation. However, when a wave impinges on a material it forces the charged species to oscillate which generates a new electric field.

The original electric wave and the newly formed electric field within the material interact forming a total electric field [23]. As the frequency of the impinging wave increases, the inertia placed on the contributing factors increases until they are physically unable to keep up. This is due to their size and beyond a certain frequency they are no longer able to contribute towards polarisation. This is best demonstrated by Figure 11.

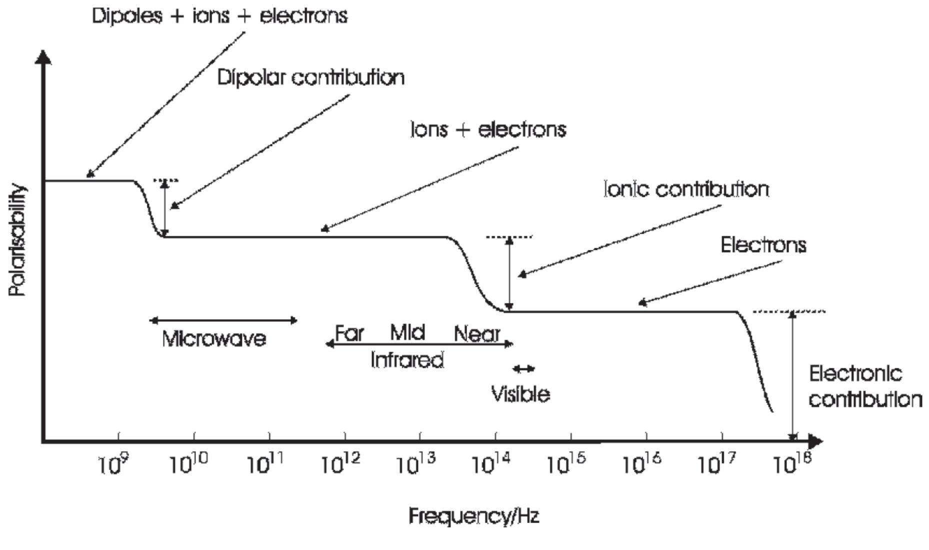

Figure 11 The frequency dependence on the types of polarisability reproduced from reference [24] with permission from John Wiley and Sons copyright@2004

Within the visible range light only interacts with the electrons in a material; knowing this and using Maxwell's relation we can alter the Clausius-Mossotti relation and we get the Lorentz-Lorenz relation [22, 24, 79]:

$$\frac{n^2 - 1}{n^2 + 2} = \frac{N\alpha_e}{3\varepsilon_o} \qquad \textbf{(22)}$$

where α_e = electron polarisability. Consequently, the electron mobility of a material is related to the refractive index such that high electron mobility will give a high refractive index and vice versa. The electron mobility of a material is related to the elements used within a material and their bonding.

The electron mobility per unit area is naturally related to the molecular spacing/molecular density. Seeing as the density of a material is related to the thermal expansion, a temperature must be stated along with the refractive index.

In a vacuum, light travels at a constant speed c and the frequency is inversely proportional to wavelength. When light enters a medium its phase speed decreases and seeing as a colour change is not observed then it is reasonable to presume that frequency is constant. Hence, when a wave travels through an optical dense material it will reduce its wavelength. This is why when different wavelengths are passed through an optically dense material they are refracted different amounts and are dispersed [22]. Consequently when refractive index is stated the wavelength used for the measurement must be stated too.

As previously stated in Section 2.2.3, there is a fibre epoxy RI mismatch for reinforcing fibres. This is due to the highly polarisable nature of benzene rings, ether links and the resulting hydroxyl groups contained in structural glycidyl epoxy resins. These are commonly cured with highly polarisable amines resulting in high RI values with respect to their densities. Due to the highly tailorable nature of epoxy resins, the resulting RI can be adjusted giving a wide array of RI. Consequently, to find a glass composition suitable of FEWS cure monitoring any resin system, a range of resin systems will have to be tested to find the upper limits of epoxy systems and provide a minimum RI for the candidate glass system.

2.3.3 Refractive Index measurement techniques

To achieve the project goals it was a fundamental necessity to measure the RI of a range of resins and glasses. There are a wide array of experimental methods available for RI determination. These include:

- Critical angle technique (Abbé) [80]
- Ellipsometry [80]
- Interferometry [80]
- Index matching methods [80]
- Brewster angle techniques [80]
- UV-Vis Spectrometer [55]

Most of these techniques usually rely on either Fresnel’s reflections from the angle of refraction or reflection against a sample, the Brewster angle of reflection, or the phase change in a polarised light ray interacting with a medium. All of these techniques rely on optically flat samples which involves polishing the surface. This can be problematic in polymers, although much simpler for glasses. The exception to this is index matching which requires particulate form sample suspended in a liquid however, the liquid should have no interaction with the particles. This limits index matching and prevents measurement of most polymers. Due to the limitations of equipment, only methods available at the University of Sheffield will be discussed.

2.3.3.1 Spectroscopic RI analysis

At the University of Sheffield, Bailey *et al* [55] used a FTIR spectrometer to measure the RI. This was done by measuring the percentage of optical transmission of a sample. The sample was incrementally ground and polished reducing the sample thickness and then measuring the percentage transmission. This was done until the sample could not be polished any further without fracturing. The transmissions and the consequential percentage reflection was extrapolated to a sample thickness of zero such that the following relation could be utilised to give the RI [55]:

$$R = 2.\left(\frac{n-1}{n+1}\right)^2 - \left(\frac{n-1}{n+1}\right)^4 \quad \textbf{(23)}$$

2.3.3.2 Critical angle technique (Abbé refractometer)

An Abbé refractometer measures the refractive index of a sample using the critical angle technique. This is performed by placing an optically flat sample onto a refracting prism using a contact solution to ensure optical continuity and preventing reflection losses between the interfaces [81, 82]. A monochromatic light is either refracted or reflected through the sample producing a light dark boundary, as shown in Figure 12. On the edge of the dark, light boundary is the critical angle of the sample for the wavelength of the monochromatic light being used. Using Snell's law, the RI of the refracting prism, measured angle of the light dark boundary the RI of the sample can be determined [82]. Reflectance mode gives a harder to interpret critical angle due to a bright to dim line rather than a bright to dark critical angle boundary of refraction.

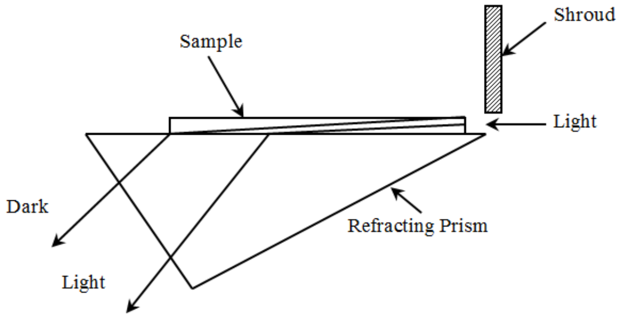

Figure 12 Cross section of the Abbe refractometer demonstrating the light propagation through a sample. Diagram drawn and modified by author from reference [82]

Chromatic light source cannot be used due to dispersion which would lead to a blurred boundary and hence a light source with known wavelengths must be used [81]. Another limitation is the contact solution has to have a higher RI than the sample and be non-absorbing in the region of interest this limits the range of contact liquids available.

2.3.3.3 Ellipsometry

Ellipsometry examines the polarisation state of light reflected from a material. The polarisation states are then converted into a refractive index. Polarisation will be discussed in the next section.

2.3.3.3.1 Polarisation

Natural light contains many electric field components of various orientations, perpendicular to the direction of travel, which is known as un-polarised light. Light can be characterised using two vectors, S (or Senkrecht) and P vectors, which are transverse and parallel electric waves to the ray of light respectively [22, 54, 83]. Knowing the magnitude and phase difference of these vectors gives one the polarisation sate of the light. This polarisation can be linear, circular or elliptically polarised [22, 54, 83, 84].

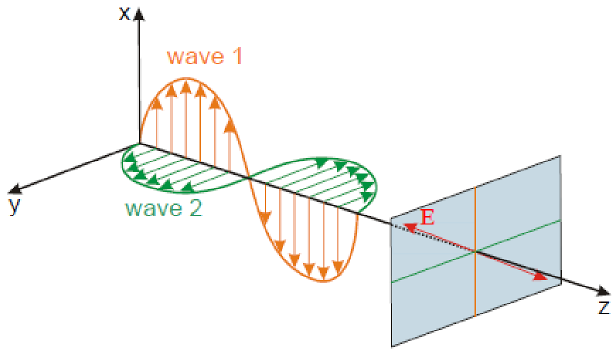

Figure 13 Diagrams showing both vectors are in phase then the resulting wave is linearly polarised[84]

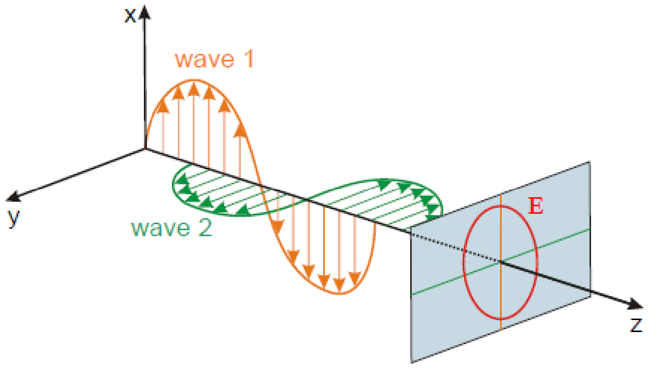

Figure 14 Diagram showing when the components are out of phase by 90° with each other and the same amplitude they will be circularly polarised [84]

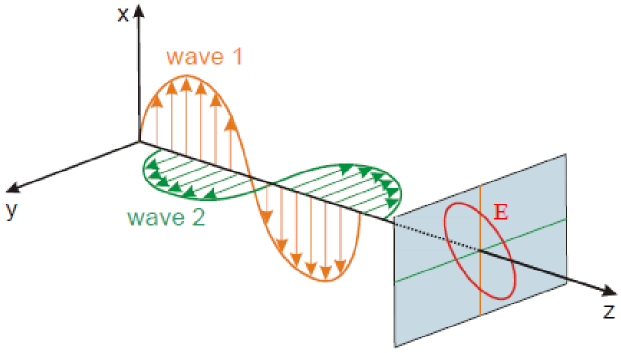

Figure 15 Diagram showing when the components are not in phase and have differing amplitudes then the resulting wave will be elliptically polarised. [84]

Figures 13-15 Reproduced with the permission of Horiba .Ltd

2.3.3.3.2 Ellipsometry theory

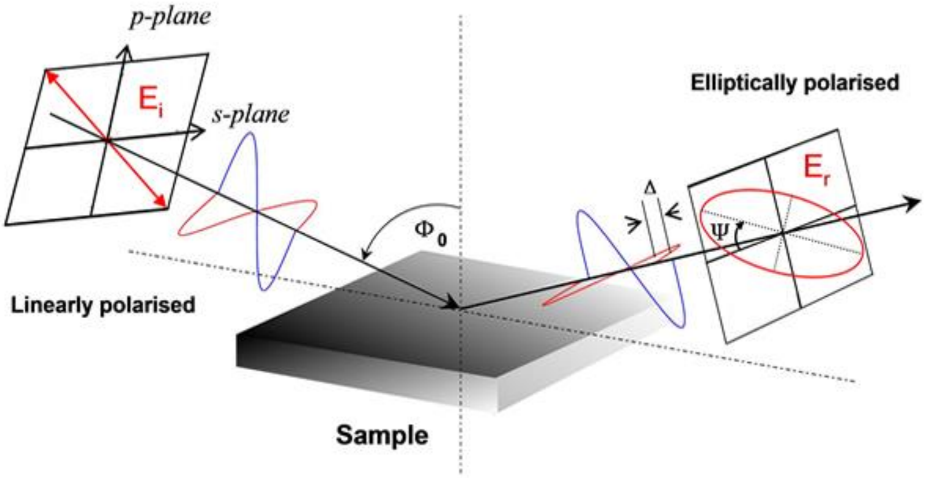

Figure 16 Principal of Ellipsometry - Change of polarisation state due to reflection from sample [85] reproduced with permission C. Smith, Trinity College Dublin

As linearly polarised light is reflected from a surface of a material, each of the components interacts differently and the resulting wave has a new polarisation, as shown in Figure 16. Ellipsometry measures the new amplitude and phase of the resulting reflected wave [80, 83, 84]. The raw data from an ellipsometer are given as Ψ = Relative amplitude change and Δ = Relative phase change between Fresnel reflections in the perpendicular “Senkrecht” r_s and parallel r_p to the plane of incidence by the following fundamental ellipsometry equation:

$$\rho = \frac{r^p}{r^s} = \tan\psi . e^{i\Delta} \tag{24}$$

where ρ is the complex ratio of the total reflection coefficients.

$$\psi = \frac{|r^p|}{|r^s|}\tan^{-1} \tag{25}$$

$$\Delta = \delta_p - \delta_s \tag{26}$$

For simple substrates Δ and Ψ can then be converted directly into optical properties using the following equations [83]:

$$n_3{}^2 - k_3{}^2 = n_1{}^2 \sin^2\theta \left[1 + \frac{\tan^2\theta(\cos^2 2\psi - \sin^2\Delta \sin^2 2\psi)}{(1+\sin 2\psi - \cos\Delta)^2}\right] \quad \textbf{(27)}$$

$$2n_3k_3 = \frac{n_1{}^2 \sin^2\theta \tan^2\theta \sin 4\psi \sin\Delta}{(1+\sin 2\psi - \cos\Delta)^2} \quad \textbf{(28)}$$

where θ is the angle of incidence for the experiment, n_3 and n_1 are the sample and atmosphere refractive indices respectively and k_3 is the extinction coefficient of the sample. From the two derived quantise $n_3{}^2 - k_3{}^2$ and $2n_3k_3$ the samples refractive index n_3 can be calculated using the following derivation [83]:

$$n_3 = \sqrt{\frac{(n_3{}^2 - k_3{}^2) + \sqrt{(n_3{}^2 - k_3{}^2)^2 + (2n_3k_3)^2}}{2}} \quad \textbf{(29)}$$

The most common use of ellipsometry is for measurement of film thicknesses. So as long as the measured films have known/calculated optical properties the thickness of the films can be calculated. Ellipsometry can be performed using a single wavelength or a range of wavelengths, known as spectroscopic ellipsometry.

2.3.3.3.3 Backside reflections

When examining transparent samples light can be reflected from the rear surface. If this back side reflection (BSR) interferes with the top face reflection they can interact resulting in inaccurate data [83, 84, 86]. To remove these back side reflections many methods have been used these include:

- Large sample thickness or wedging to spatially separate the BSR [84]
- Painting with absorbing medium
- Roughening
- Index matching [84, 86, 87]
    - Roughened clear adhesive tape [87]
    - Vaseline [87]
    - Toothpaste [87]
    - Blu-tack™ [86]

The benefit of index matching is the non-destructive nature which enables the sample to be used for other experiments reducing further sample preparation. Roughening is naturally a destructive technique but, is also highly effective. Roughening can cause issues with warping when dealing with softer polymeric materials. Painting is a highly effective technique however, it relies on there being no interaction with the substrate.

2.3.4 High refractive index glasses

As previously stated in Section 2.2.3 epoxy resins are stated as having an upper limit of 1.63 $n_{D.}$ There are a wide array of glass systems which possess a RI>1.63 n_D; however, many of these systems are unsuitable due to lack of fibre formability, toxicity, inherently poor chemical durability and mechanical properties. The following literature reviews high refractive index glass systems whilst narrowing down glasses which do not meet the projects criteria.

Using unconventional containerless processing of glasses, crystal nucleation can be suppressed leading to vitrification of uncommon glass formers such as $BaTi_2O_5$ [88] and $0.3La_2O_3$-$0.7Nb_2O_5$ [89] which lead to high RI values of 2.1 and 2.3 respectively. Glasses with high levels of heavy metal oxides making up the main glass former have been reported [90, 91] with some very high RI values and extended infra-red transmission bands due to the large atoms [89, 90]. However, for the purpose of the project containerless processing is unsuitable for fibre drawing, and chemical durability must be considered.

2.3.5 Chemical Durability

The chemical durability of glass fibres is of the upmost importance due to the large surface area of glass fibres [34]. Glass formers such as borate [91], germanate [90], gallate [91] and phosphate [92] oxide glasses form higher refractive index glasses as opposed to silicates with larger IR transmission windows. However, many non-silicate glasses are readily soluble in water and as a result they have limited applications [35]. Silicate glasses are more durable, however silica can be dissolved in solutions with pH >9 [93].

Fluxes are typically added to silicates in the form of alkali ions reducing processing temperatures however, this leads to the reduction in the chemical durability of the silicate [35]. The highly mobile alkali ions and alkali earth ions to a lesser extent diffuse into solution by ion exchange. The leached alkali ions cause an increase in the pH of the solution, which can further lead to the dissolution of the remaining network [35]. Therefore low alkali and alkaline earth silicate glasses tend to have better chemical durability [93]. The ability of the alkali ions to leach into solution is dependent on the mobility of the ion K > Na > Li [93].

2.3.6 Silicate glasses

In summary, non-silicate glasses possess inherently higher RI and IR cut off windows than their silicate counterparts due to the larger atom sizes and polarisations. On the other hand, silicates offer simple integration into PMC due to similar chemistry and higher chemical durability but, possess low RI values [91, 94]. However, the addition of large polarisable elements causes significant RI increases to silicates. The next section will focus on the modification of silicate glasses to increase the RI.

2.3.7 Mechanical properties of silicate glasses

The strength of glass is flaw dependent. The abrasion of glass against any harder material or itself, or chemical attack can induce flaws which lead to failure [34, 35]. When glass is formed into fibres the surface area is maximised to the volume of material, enabling a large quantity of flaws to develop resulting in fibre failure. To combat this issue sizes are placed on the fibres immediately after drawing which lubricate the fibres, prevents flaws and bind the fibres to the matrix polymer. This process results in a controlled flaw level which enables a discussion of the composition relating to the mechanical properties [34].

The Young’s modulus (*E*) is a bulk glass property dependent on the batch composition and resulting structure [35] elongation of the structure, density and thermal history [34]. To increase the *E* the amount of bridging oxygen must increase within the structure. As the amount of bridging oxygen increases the structure changes from a chain to layered to a 3D network [35]. Breaks in the structure, such as non-bridging oxygen (NBO), allow easier atom motion resulting in a reduction in *E*. Alkali and alkaline earth ions are used in glass melts as fluxing agents to reduce processing temperatures and melt viscosity however, they do this by reducing the concentration of NBO which as stated before adversely affects *E* [35]. Alumina is used within reinforcing fibres to increase the modulus and strength of silica by increasing the connectivity of the network increasing *E* [95]. Rare earth ions can be added to increase the strength and *E* by producing strong bonds and high density packing. Table 2 shows the mechanical properties of commonly used glass fibres.

Table 2 Tensile strength and Young's modulus of common glass fibres [31]

Fibre	**Tensile strength (MPa)**	**Young's Modulus (GPa)**
Boron containing E-glass	3100-3800	76-78
Boron free E-glass	3100-3800	80-81
ECR-glass	3100-3800	80-81
D-glass	2410	-
S-glass	4380-4590	80-81
Silica	3400	69

2.3.8 Modification of silicates glass for high RI

Heavy elements such as lead, thallium and bismuth, have been incorporated into silicate glasses producing high refractive indices however, they are toxic and possess absorption bands in the visible spectrum [89]. Lead silicates have been traditionally used, as ornate high RI glasses however, they have low chemical durability in acidic solutions and the lead volatilises during fiberisation, resulting in structural discontinuities leading to fibres fracturing during processing [96].

Niobium has been extensively used within the literature as an addition to silicates for non-linear optical glass with very high refractive indices [89, 94, 97-102]. It has also been stated that Nb_2O_5 replaces SiO_2 in the network [101] and forms NbO_6 octahedrals improving mechanical properties [94] and improving chemical durability [101, 103]. Consequently, Niobium silicates will be investigated.

It has been previously stated that alkali and alkali earth ions are used to reduce the processing temperature and melt viscosity however, these effects need to be balanced with the negatives of reduced chemical durability, Young's modulus and glass stability [35]. The following sections will cover alkali containing silicates and non-alkali containing silicates.

2.3.8.1 High refractive index alkali containing silicates

A survey of the literature gave a range of compositions which are of interest; these are given in Table 3. The addition of alkali ions effect on RI follows the trend of Na < Li < K < Rb < Cs which is unusual when viewed from the atomic size and resultant polarisability. The RI increase with Li is caused by a shrinkage of the network and resultant higher electron density [35, 104]. Consequently, even though Lithium silicates are not expected to possess high RI they will be investigated. Sigaev *et al* [100] produced a range of lithium niobium silicate glasses, the composition with the lowest glass transition (T_g) and presumed lowest fibre forming temperature is shown in Table 3.

Enomoto *et al* demonstrated a range of potassium niobium silicate and germinates with high refractive indices from 1.75 to 1.81 (at 632.8 nm) [94]. Despite the potassium niobium silicate producing the lowest RI, it also gave the largest glass transition and crystallisation separation of 91°C. The composition is given in Table 3.

Using Sciglass database a range of sodium titanium silicate glasses with high RI values were discovered [105]; these glasses were narrowed down discarding any compositions with a RI below 1.63 followed by a composition with the highest silica content and lowest liquidus was selected giving the Na:Ti:Si shown in Table 3.

Table 3 High refractive index alklai silicates

Composition	**K:Nb:Si [94]**	**Li:Nb:Si [100]**	**Na:Ti:Si [105]**
SiO_2	50	46.1	50
Li_2O	0	38.5	0
K_2O	25	0	0
Na_2O	0	0	25
TiO_2	0	0	25
Nb_2O_5	25	15.4	0
Refractive index	1.75 (at 632.8 nm)	-	1.678 (at 589 nm)

2.3.8.2 High refractive index non-alkali silicates

A range of high dielectric constant glass fibres have been developed [99] for gamma radiation absorption and concentration of electromagnetic energy. Maxwell's relation given in equation 16 demonstrates that the refractive index is related to the square of the dielectric constant. Consequently, the higher the dielectric constant the higher the refractive index within the visible light.

Reference [99] gave a range of liquidus and log(η/Poise)=2.5 fibre forming temperature for each of the compositions and is given in 8.1 Appendix A-1. The glass with the largest fibre formability, known as H-glass, is given in Table 4.

Table 4 The glass composition from reference [99]known as H-glass

Composition	**H-glass** [99]
SiO_2	50.00
Na_2O	0.00
K_2O	0.00
MgO	0.00
CaO	7.50
SrO	7.50
BaO	15.00
Al_2O_3	0.00
TiO_2	11.55
ZrO_2	2.45
$NbO_{2/5}$	6.00

Reference [99] led to a patent [96] producing a wide array of high dielectric constant glass compositions given in 8.2 Appendix A-1 with liquidus and log(η/Poise)=2.5 fibre forming temperature.

3 EXPERIMENTAL

3.1 Glass selection

Although exploring chemical durability is only a consideration of the current research, it would be preferential to have an alkali free glass. However, the furnace set out for fibre drawing is limited to 1200 °C. Consequently, two sets of silicates will be investigated; alkali containing and non-alkali containing silicates with the aim of achieving more chemically durable fibres whilst facilitating fibre drawing.

3.1.1 Alkali containing silicates

Alkali silicate compositions are given in Table. 5. The alkali containing glasses were examined in an attempt to produce high RI glasses which had lower melting points than their non-alkali counter parts. The composition 25 mol% K_2O, Nb_2O_5 and 50 mol% SiO_2 (Table 3) from Enomoto *et al* paper [94] was modified to 3K:3Nb:4Si in order to increase the alkali and niobium content reducing processing temperatures and increasing the RI. After 3K:3Nb:4Si crystallised, it was decided that adding more silica and reducing the alkali content would prevent crystallisation, consequently 2K:3Nb:5Si was melted. Li:Nb:Si from reference [100] was melted as given in Section 2.3.8.1, whilst Li:Ti:Nb:Si substituted 50% of the SiO_2 for TiO_2 with the aim to increase the refractive index. Na:Ti:Si was also taken from [105] as given in Section 2.3.8.1.

Table. 5. Compositions of alkali containing silicate glasses in mol%.

Composition	**3K:3Nb:4Si**	**2K:3Nb:5Si**	**Li:Nb:Si**	**Li:Ti:Nb:Si**	**Na:Ti:Si**
SiO_2	40	50	46.1	23.05	50
Li_2O	0	0	38.5	38.5	0
K_2O	30	20	0	0	0
Na_2O	0	0	0	0	25
TiO_2	0	0	0	23.05	25
Nb_2O_5	30	30	15.4	15.4	0

3.1.2 Non-alkali containing silicates

Alkali free glasses were investigated to produce glasses with suitable mechanical properties and chemical durability similar to current reinforcing fibres whilst possessing a high RI. Two varieties of non-alkali containing silicates were attempted: niobium modified reinforcing style compositions and high dielectric constant glasses.

3.1.2.1 Reinforcing style glasses

Two reinforcing style calcium alumina silicates compositions were selected from the literature and Al_2O_3 was substituted with Nb_2O_5 in each case; these compositions are given in Table 6. Boron-free E-glass was selected due to the common use in composites. In order to increase the RI 5 mol% Al_2O_3 was subtracted from the composition and 5 mol% Nb_2O_5 was added. A calcium aluminosilicate was chosen from reference [106] due to known stability of the composition. The Nb_2O_5 modified version had the Al_2O_3 mol% halved and Nb_2O_5 substituted as shown in Table 6.

Table 6 Alkali free silicate plus planned compositions

Composition	**Boron Free E-glass** [34]	**E-glass -5%Al + 5%Nb**	**Ca:Al:Si** [106]	**Ca:Al:Nb:Si**
SiO_2	56.43	56.43	41.43	41.43
Na_2O	0.61	0.61	0.00	0.00
K_2O	0.16	0.16	0.00	0.00
MgO	1.96	1.96	0.00	0.00
CaO	19.42	19.42	51.40	51.40
SrO	0.00	0.00	0.00	0.00
BaO	0.00	0.00	0.00	0.00
Al_2O_3	20.73	15.73	7.71	3.855
La_2O_3	0.00	0.00	0.00	0.00
TiO_2	0.70	0.70	0.00	0.00
ZrO_2	0.00	0.00	0.00	0.00
Nb_2O_5	0.00	5.00	0.00	3.855

3.1.2.2 High dielectric constant glasses

H1 composition in Table. 7 was modified from the composition from Naka’s paper [99] with the highest fibre formability and then the $NbO_{2/5}$ was set equal Nb_2O_5 in order to increase the RI.

The compositions from the high dielectric constant glasses from the patent [96] were plotted with the log(η/Poise)=2.5 fibre forming temperature – liquidus temperature on the x-axis against the liquidus point y-axis and dielectric constant at 1MHz as data labels and are shown in Figure 17. The liquidus point was selected as a parameter due to the max temperature of the fibre drawing furnace. The compositions in the bottom right hand corner have the lowest liquidus points and highest fibre formability. Two sets were chosen: H2 and H3 which were selected due to the lowest liquidus points and largest fibre formability whilst H4, H5 and H6 were selected due to the highest dielectric constants with a lower maximum liquidus temperature of 1075 °C and highest fibre formability window >75 °C.

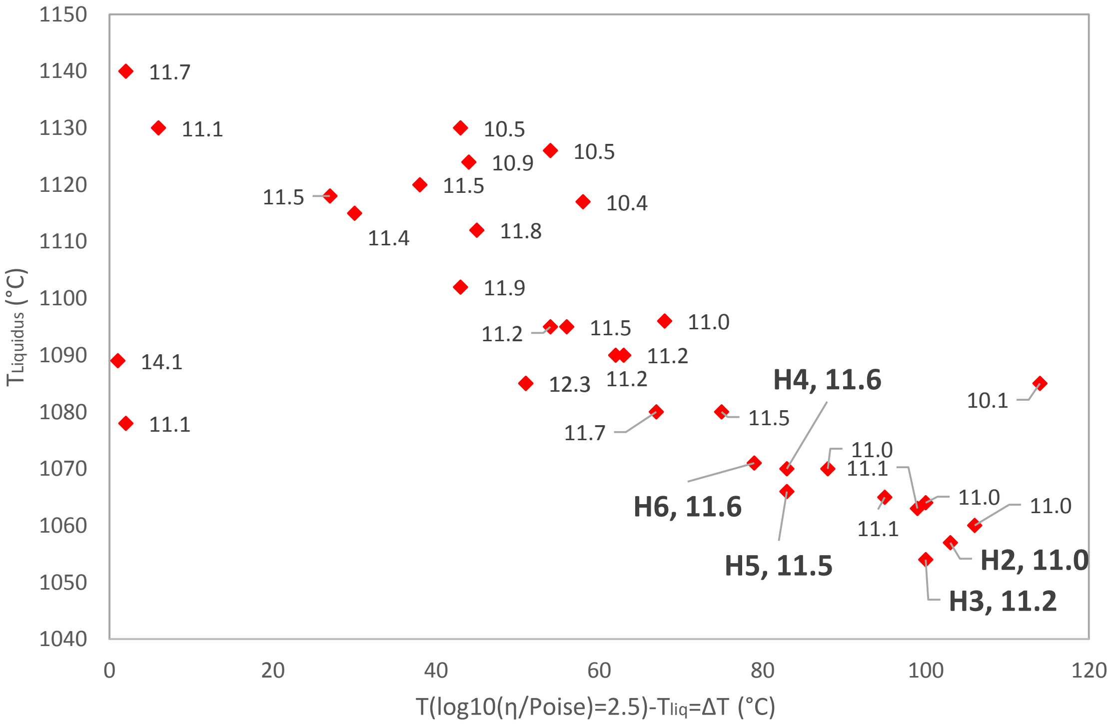

Figure 17 High dielectric constant glasses, ΔT versus $T_{liquidus}$ data labels equals dielectric constant at 1MHz [96]

Non-alkali containing silicate compositions are given in Table. 7.

Table. 7. Composition of non-alkali containing silicate glasses in mol%.

Composition	**Ca:Al:Nb:Si**	**E-glass -5%Al + 5%Nb**	**H1 Pt**	**H1 –Ti +La**	**H2 ME**	**H3 Pt**	**H4 ME**	**H5 ME**	**H6 ME**
SiO_2	41.43	56.43	50.00	50.00	50.79	52.08	51.56	51.55	51.83
Na_2O	0.00	0.61	0.00	0.00	0.00	0.00	0.00	0.00	0.00
K_2O	0.00	0.16	0.00	0.00	0.00	0.00	0.00	0.00	0.00
MgO	0.00	1.96	0.00	0.00	0.00	0.00	0.00	0.00	0.00
CaO	51.40	19.42	7.50	7.50	9.52	9.38	7.73	9.28	7.77
SrO	0.00	0.00	7.50	7.50	6.35	6.25	7.73	6.19	7.77
BaO	0.00	0.00	15.00	15.00	15.87	15.63	15.46	15.46	15.54
Al_2O_3	3.86	15.73	0.00	0.00	2.65	1.04	0.00	0.00	0.00
La_2O_3	0.00	0.00	0.00	11.55	0.00	0.00	0.00	0.00	0.00
TiO_2	0.00	0.70	11.55	0.00	9.63	10.31	11.91	11.91	11.11
ZrO_2	0.00	0.00	2.45	2.45	2.01	2.19	2.52	2.52	2.35
Nb_2O_5	3.86	5.00	6.00	6.00	3.18	3.13	3.09	3.09	3.63

3.2 Glass production

Glasses were batched using the constituents given in Table 8 to produce a 300 g glass melt. Each constituent was weighed out using scales to two decimal places. These were then mixed by hand using a spatula and any lumps were broken up to form a uniform powder.

Table 8 Raw constituents, supplier and purity for each oxide

Desired oxide	Constituent	Supplier	Purity (%)
SiO_2	SiO_2	Glassworks	99.5
Li_2O	Li_2CO_3	Alfa Aesar	99
Na_2O	Na_2CO_3	Glassworks	99.1 (min)
K_2O	K_2CO_3	Glassworks	99.5
MgO	$4MgCO_3.Mg(OH)_2.5H_2O$	Alfa Aesar	-
CaO	$CaCO_3$	Glassworks	99.3
SrO	$SrCO_3$	Sigma-Aldrich	>98
BaO	$BaCO_3$	Alfa Aesar	99
Al_2O_3	$Al(OH)_3$	Sigma-Aldrich	-
La_2O_3	La_2O_3	Sigma-Aldrich	99.9
TiO_2	TiO_2	Acros	99
ZrO_2	ZrO_2	Fisher Chemical	-
Nb_2O_5	Nb_2O_5	Alfa Aesar	99.9

Table 9. Processing conditions for glass compositions

Composition	**Temperature (°C)**	**Crucible**	**Furnace type**	**Stirring regime**	**Time (hours)**	**Annealing temperature (°C)**
3K:3Nb:5Si	1450	Pt	Electric	4hrs, Pt stirring paddle	5	Splat quenched
2K:3Nb:5Si	1450	Pt	Electric	4hrs, Pt stirring paddle	5	Splat quenched
Li:Nb:Si	1450	Pt	Electric	4hrs, Pt stirring paddle	5	650
Li:Ti:Nb:Si	1450	Pt	Electric	4hrs, Pt stirring paddle	5	Splat quenched
Na:Ti:Si	1450	Mullite	Electric	Manual Si rod stirring at 2hrs & 4hrs	5	550
Ca:Al:Nb:Si	1450	Pt	Electric	4hrs, Pt stirring paddle	5	780
E-glass -5%Al + 5%Nb	1450	Pt	Electric	4hrs, Pt stirring paddle	5	700
H1 Pt	1450	Pt	Electric	4hrs, Pt stirring paddle	5	750
H3 Pt	1450	Pt	Electric	4hrs, Pt stirring paddle	5	750
H3 GM	1450	Mullite	Gas	Manual Si rod stirring at 2hrs & 4hrs	5	750
H3 EM	1450	Mullite	Electric	4hrs, Mullite stirring paddle	5	750
H2 GM	1500	Mullite	Gas	Manual Si rod stirring at 2hrs & 4hrs	5	750
H4 GM	1500	Mullite	Gas	Manual Si rod stirring at 2hrs & 4hrs	5	750
H5 GM	1500	Mullite	Gas	Manual Si rod stirring at 2hrs & 4hrs	5	750
H6 GM	1500	Mullite	Gas	Manual Si rod stirring at 2hrs & 4hrs	5	750

Batches were melted according to Table 9. Glasses were processed using either a platinum crucible with an electric furnace or a mullite crucible in a gas furnace. In all cases an electric furnace with a Pt crucible was preferable due to the prevention of contaminating the glass from the dissolution of the mullite however, during the electric furnace downtime, a gas furnace with mullite crucible was the only option.

Melts performed in mullite crucibles were added in entirety to the crucible and heated at 3 °C/min until the desired temperature was reached, then processed according to Table 9. For melting in Pt, the batch was added to a cold crucible and placed in a top loaded furnace at the melt temperature of 1450 °C. Consequently batches were added up to 2 cm from the top of the crucible to prevent any of the batch being forced out due to gas evolution. The remaining batch was added bit-wise to the melt as it proceeded. The melt was then allowed to settle for 1 hour to thermally homogenise and allow the chemical reactions to occur. The melt was then stirred for 4 more hours using a Pt stirring paddle to fully homogenise the melt before casting.

Once the glasses were ready for pouring, the crucibles were removed and left until the melt viscosity was visually viscous enough to prevent the melt from folding back on itself. This was done to prevent the melt from folding upon itself and causing striations during casting, as shown in Figure 18. Blocks were then poured into heated steel moulds and left to cool until the block had sufficient integrity to not collapse under its own weight. Blocks were then placed in an annealing furnace for an hour at the annealing temperature stated in Table 9 and cooled at 1 °C/min to room temperature. This was done to remove any internal stresses.

Some melts instantly crystallised upon pouring and in attempt to see if a glass could be formed they were splat quenched between two 5 mm thick, steel plates. This was done to increase the cooling rate; samples which were splat quenched were not annealed.

Figure 18 Casting of glass into a steel mould

3.2.1 Fibre drawing by hand

After blocks had been poured, the remaining melt was heated for 10-15 minutes to allow the melt to return to the processing temperature enabling fibres to be drawn. Once the crucible had returned to melt temperature it was removed and placed on a furnace brick allowing it to cool until a "skin" was formed on the top of the melt. Once the skin had formed a silica glass rod was placed into the melt and up drawn by hand to demonstrate proof of concept, as shown in Figure 19. All samples produced in Pt were tested for hand fibre drawing however, those produced in mullite were not tested for fibre drawing due to the health and safety factors in which the mullite could thermally shock spilling the glass melt.

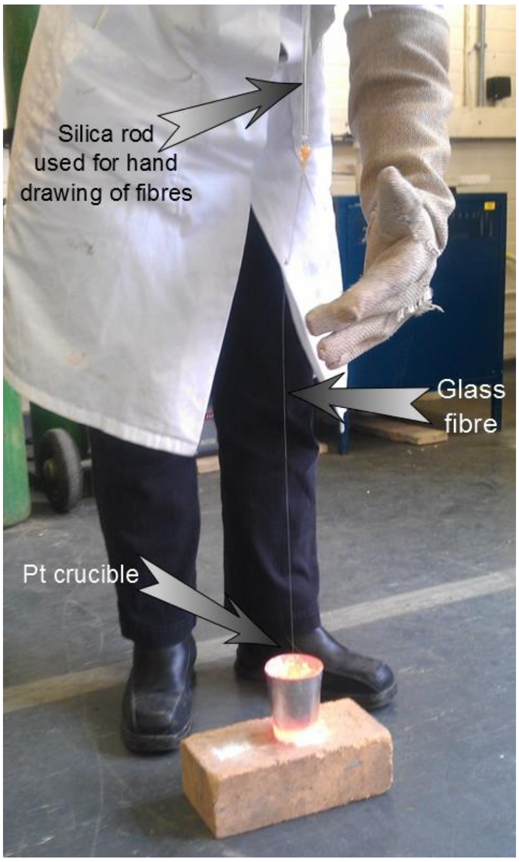

Figure 19 Demonstration of fibre up drawing by hand. Pt crucible was placed on a furnace brick. Upmost care was taken using, safety shoes, a lab coat and kevlar gloves

3.3 Glass sample preparation

Glass blocks were sectioned using an Isomet slow cutting saw with a diamond blade. IsoCut™ Fluid cutting solution from Buehler Ltd was used to lubricate and cool the blade. Sections were taken from the most optically clear section of each sample with minimal striation. The sections were then mounted on to 31.75 mm diameter by 15 mm thick stainless steel cylinders using 509 Crystalbond™ adhesive. The cylindrical blocks were heated on a hot stage to 150-200 °C and the sectioned glasses were pre-heated in an oven to 50 °C. Once the 509 Crystalbond™ had melted the glass samples were removed from the oven and applied to cylinders and pressed down until all the bubbles were removed from under the glass. Pre-heating of the sectioned glass was used to prevent any chance of thermal shock when applying the glass to the heated cylinders. Similarly samples were left on the hot plate to slowly cool, again minimising any chance of thermal shock.

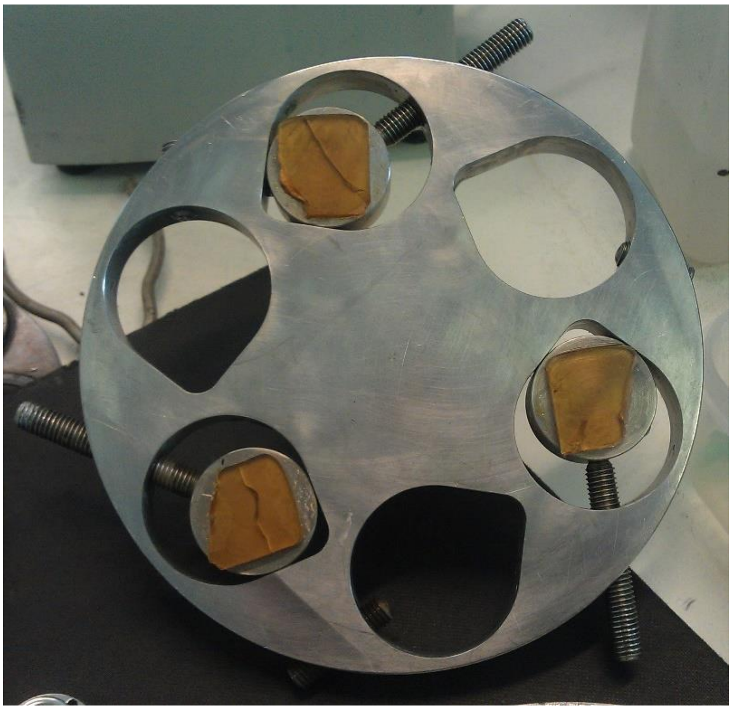

Figure 20 Samples held on stainless steel cylinders and positioned in single point grinding jig.

Once the samples were cooled and firmly bonded to the cylinders they were placed in a single point grinding head for automatic polishing as shown in Figure 20. Samples were loaded into the head using a bulls-eye sprit level to ensure they were all parallel with the head of the grinder. Samples were then ground using an 8" diameter 15 µm diamond grinding plate from Beuhler Ltd at 61 rpm plate speed and a head speed of 60 rpm with a force of 20 N over the entire head. 61 and 60 rpm were chosen for the head and plate speed to optimise use of the whole disk, similar speeds were chosen to optimise the surface flatness by matching the centrifugal forces of the head and plate. 20 N was used to minimise the loading onto the sample and prevent cracking. Samples were then ground for 1-2 minutes and realigned in the jig; this was repeated until a clear level uniform surface was produced. After this they were further polished automatically using the same procedure through 6 µm, 3 µm and 1 µm diamond pastes on cashmere cloths for 5 minutes per grade. Samples were polished only to 1 µm to remove specular reflections as no further improvement was found upon using ¼ µm polishing. After polishing, the samples and cylinders were reheated on the hot plate to remove the polished sections from the cylinders. Once the adhesive had warmed enough to free the sample they were gently removed and washed in acetone dissolving any remaining adhesive. Samples were then stored in lint-free cloths to protect them.

All of the non-crystalline melts were processed in this way to prepare them for optical analysis, in order to determine their refractive index and transmission characteristics. Additionally, E-glass and Advantex glass were prepared to act as a comparator between current commercial glass fibres and the putative glasses examined in this study.

3.3.1 Glass preparation for ellipsometry

After the sample was prepared using the method given in Section 3.3 and had been checked for uniformity, the roughened backside of the sample was sprayed with matt black paint. Samples were checked for any scratches on the surface using an optical microscope. Scratches were particularly important for ellipsometry due to the resulting specular reflections causing a depolarisation of the reflected beam resulting in unreliable data [84].

3.3.2 Glass preparation for UV Vis/FTIR spectroscopy

Samples for UV Vis and FTIR spectroscopy were prepared using the technique given in Section 3.3 but, stopping at 3 µm polishing. The sample was then heated, removed and acetone washed wiping it down with a lint-free cloth. The sample was then bonded with polished side down using 509 Crystalbond™ onto the grinding cylinder to enable grinding of both sides. The grinding and polishing stages were repeated until a parallel sample was produced. The sample was finally removed from the block, acetone washed and checked for uniformity. The sample was then repolished by hand using 6 µm, 3 µm and 1 µm diamond paste on both sides. The samples were finally washed in isopropyl alcohol (IPA) and stored in lint-free cloths before use.

3.3.3 Powder sample preparation

Many samples were required in powder format for the following experiments:

- X-ray diffraction (XRD)
- Differential thermal analysis (DTA)
- Liquidus
- Viscometer
- X-ray fluorescence

For XRD, DTA, liquidus measurement and viscometry, powders were crushed from annealed blocks of glass using a percussion mortar. Samples were then passed through a 200 µm sieve to separate the fine powder. A magnet was placed over the powder in order to remove any iron contamination from the initial crushing stage.

For X-ray fluorescence, samples were broken from cast blocks of glass by wrapping the glass in PTFE fabric and breaking it with a hammer, this was done to prevent additions from the percussion mortar or any hammer face. Samples were sent as small sections of 5-10 g and were further processed into a powder by AMG superalloys .Ltd.

3.4 Epoxy production

To find the upper limits of RI values of epoxies a range of resins and hardeners were tested. Three resins were selected for investigation, Epikote 828 supplied by Delta Resins Ltd, Huntsman’s MY0510 and Huntsman’s MY721 which are primarily diglycidyl ether of bisphenol A (DGEBA), triglycidyl p-amino phenol (TGAP) and tetraglycidylether of 4,4′ diaminodiphenyl methane (TGDDM) respectively, the chemical formulas of which are shown in Figure 21. These resins were selected due to their widespread use as aerospace grade resins.

The curing agents used were 4,4'-diaminodiphenyl sulfone (DDS), 4,4'diamine-diphenylmetane (DDM), triethylenetetramine (TETA) and norbornene maleic anhydride (NMA) with a benzyl dimethylamine (BDMA) accelerator, all of which were supplied by Sigma Aldrich Ltd and are shown in Figure 22.

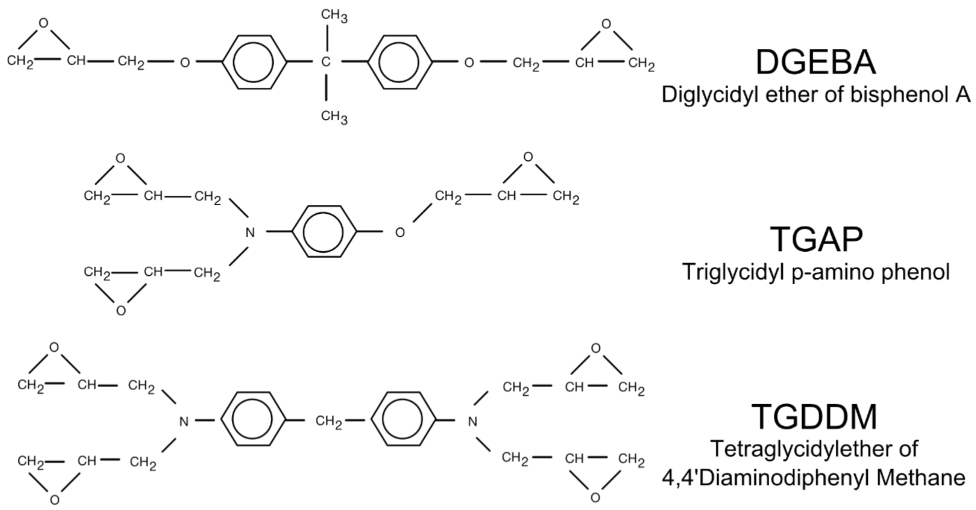

Figure 21 Chemical structures of di, tri and tetra functional epoxy resins [7]

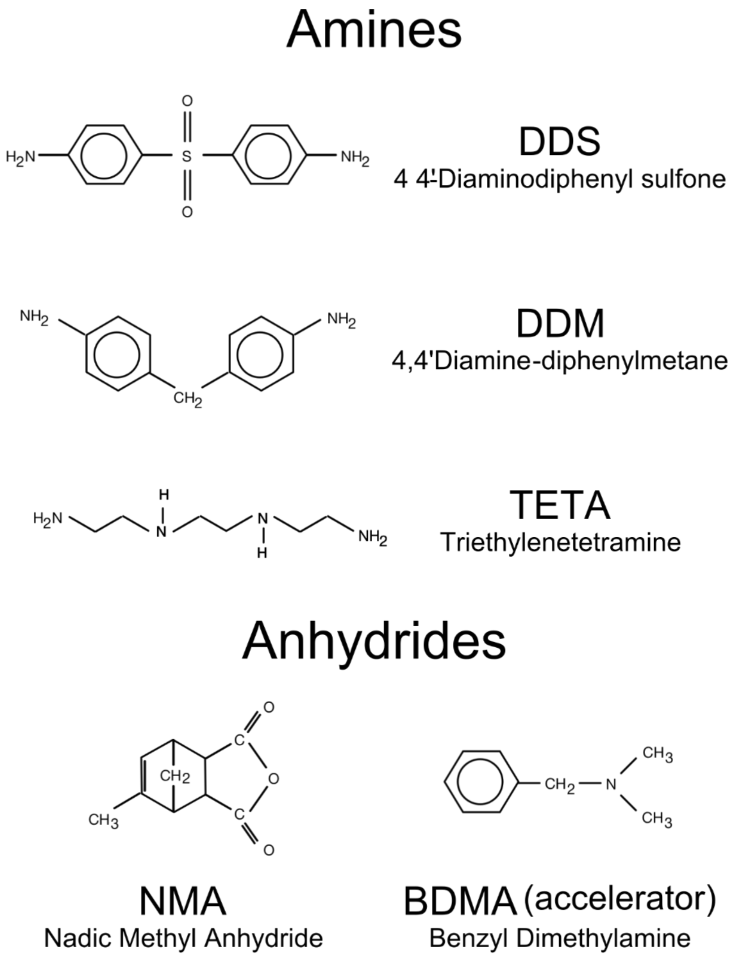

Figure 22 Chemical structures of amine and anhydride curing agents [8]

The epoxy, amine hydrogen and anhydride equivalent weights are given in Table 10, Table 11 and Table 12 respectively.

Table 10 The epoxy equivalent weights is given by the median molecular weight divided by the number of epoxy groups for each resin type

Epoxy	Epoxy theoretical maximum functionality	Manufacturers epoxy equivalent weight
828	2	187 (184-190)
MY0510	3	100 (95-106)
MY721	4	114 (109-117)

Table 11 Amine Equivalent weight is given by the median molecular weight divided by the amine theoretical max functionality (number of hydrogens attached to the nitrogen)

Amine	Amine theoretical maximum functionality	Amine molecular weight	Amine hydrogen equivalent weight
DDS	4	248	62.0
DDM	4	198	49.5
TETA	6	146	24.3

Table 12 Anhydride + Accelerator[107]

Anhydride	Anhydride theoretical maximum functionality	Anhydride molecular weight	Anhydride hydrogen equivalent weight
NMA	1	178.2	178.2

As stated in Section 1.3.1 an epoxy excess is used for the desired properties. These excess factors have been previously optimised in ref [7] apart from DDM, for which the excess factor for DDS samples was used, with the exception of 828:DDM which was initially trialled using the same mix ratio by weight as DDS. The mix ratios are shown in Table 13:

Table 13 Resin mix ratios and epoxy excess factors taken from ref [7]

Resin	Stoichiometric ratio based on theoretical functionalities	Epoxy excess correction factor	Corrected ratio for actual cure
828/DDS	187:62 = 100:33.2	1.11	100:30
828/DDM	187:49.5 = 100:26.5	1.13	100:30
828/TETA	187:24.3 = 100:13	1.00	100:13
MY0510/DDS	100:62 = 100:62	1.72	100:36
MY0510/DDM	100:49.5 = 100:49.5	1.72	100:28.8
MY721/DDS	114:62 = 100:54.4	2.09	100:26
MY721/DDM	114:49.5 = 100:43.4	2.09	100:20.8

Resins and curing agents were weighed out to 2 decimal places and mixed using the ratios in Table 13.

Resin systems including DDS or DDM were prepared by weighing out the resin into a glass beaker separately from the curing agent. The resin was then heated in a paraffin oil bath whilst stirring using an overhead stirrer. Once the resin reached 100 °C the curing agent was added and heated to 140 °C, or until the curing agent had fully dissolved in the resin in the case of that occurring earlier. The hardener was added at high temperatures to minimise the time in which the epoxy could gel whilst processing.

For samples cured using NMA/BDMA and TETA the hardeners were added and stirred at room temperature using a wooden tongue depressor, by hand, until a visually uniform mixture was produced. After the curing agent was added, mixtures were degassed in a vacuum oven for 10 minutes, and samples using DDS and DDM were degassed at 100°C, while the other samples were degassed at room temperature.

Samples were produced as “splats” on float glass coated with mould released. Henkel Frekote® 770-NC mould release was applied using a cotton cloth; once the solvents had flashed off a separate cotton cloth was used to polish the Frekote until a very smooth surface was obtained, in which the cotton cloth would glide over the glass surface with minimal resistance. This process was repeated 6 times on the first run and twice or more for each successive run on the same piece of glass until the minimal resistance was observed. This was done to ensure a reliable mould release was obtained. Samples were cast onto the glass in small pools (splats) to prevent any additional cutting of the samples, as shown in Figure *23*.

Figure 23 Examples of cured pools of resin before grinding.

After casting the resin samples were then cured in a programmable oven using the schedules shown in Table 14. The curing schedules for DDS cured resins were taken from reference [7] with the MY721 and MY0510 sample being cured at 200 °C to ensure samples showed no residual cure as shown in Behzadi dynamic mechanical thermal analysis (DMTA) traces. The DDM cured samples were cured using the respective epoxy resin with DDS curing schedule due to the similarities between the two curing agents and an investigation being beyond the scope of this work. The cure schedule of NMA and BDMA cured samples was taken from Grainger thesis [108]. TETA curing schedule was given in reference [109].

Once the samples had fully cured they were removed from the glass sheet and stored in press sealed bags in a desiccator over phosphorous pentoxide obtained from Sigma Aldrich Ltd.

Table 14 Cure schedules for resin systems

Procedure	828 : DDS/DDM	MY0510 : DDS/DDM	MY721 : DDS/DDM	828 : NMA, BDMA	828 : TETA
Ramp	120 °C at 2 °C/min	130 °C at 2 °C/min	130 °C at 2 °C/min	80 °C at 2 °C/min	20 °C
Dwell	120 °C for 2 hours	130 °C for 1 hour	130 °C for 1 hour	80 °C for 2 hours	20 °C > 12 hours
Ramp	185 °C at 2 °C/min	200 °C at 2 °C/min	200 °C at 2 °C/min	120 °C at 2 °C/min	50 °C at 2 °C/min
Dwell	185 °C for 6 hours	200 °C for 2 hours	200 °C for 2 hours	120 °C for 3 hours	50 °C for 1.5 hours
Ramp	20 °C at 2 °C/min	20 °C at 2 °C/min	20 °C at 2 °C/min	150 °C at 2 °C/min	150 °C at 2 °C/min
Dwell	-	-	-	150 °C for 4 hours	150 °C for 0.5 hours
Ramp	-	-	-	20 °C at 2 °C/min	20 °C at 2 °C/min

3.4.1 Epoxy sample preparation

Epoxy samples were ground parallel and flat using a custom build grinding jig. A cross section of the jigs set up is shown in Figure 24. The jig comprised of a cylinder with a hole in the centre for another cylinder to fit into. The central cylinder could be locked into place using a set of grub screws. This allowed a small section to be ground off the sample each time, while ensuring that the front and back faces remained parallel. This method produced samples, which after painting the roughened back surface, were ideal for ellipsometry measurements.

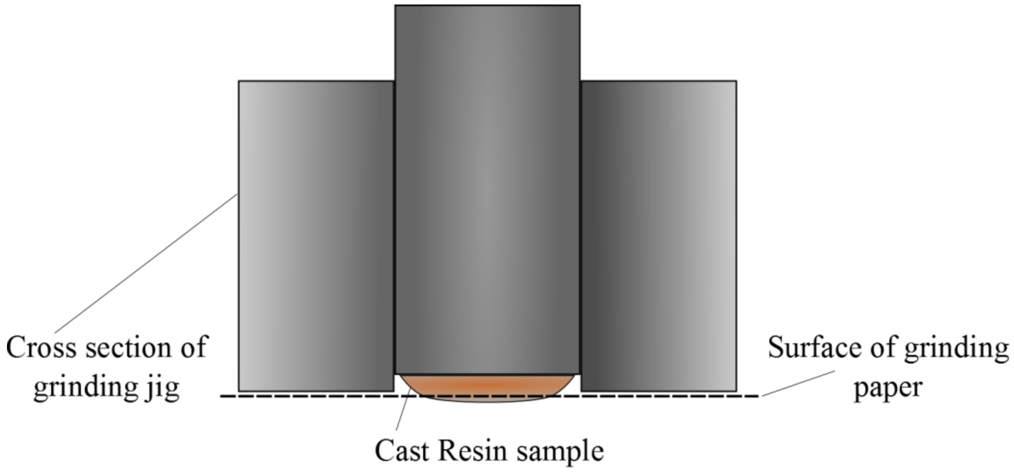

Figure 24 *Cross-section of the grinding jig for epoxy resin samples*

3.5 Optical Analysis

3.5.1 Refractive index measurements – Ellipsometry

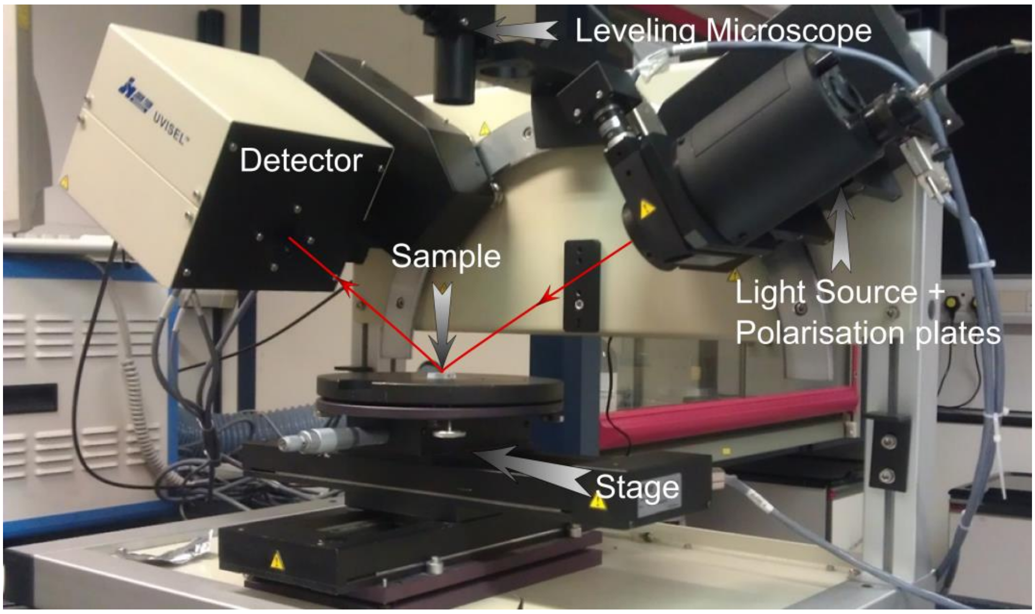

Figure 25 Horiba-Yvon UVISEL spectroscopic ellipsometer

Initially samples were tested using an Abbé refractometer as demonstrated in Section 2.3.3.2. However, results were problematic and consequently ellipsometry was chosen. Ellipsometry was performed on a Horiba-Yvon UVISEL spectroscopic ellipsometer with a 75W Xe lamp, as shown in Figure 25. The system was controlled using a computer running the DeltaPsi2 software supplied by Horiba. Samples were prepared in a manner that was dependent on the material type, as described in Sections 3.3.1 and 3.4.1 for glasses and epoxies respectively.

To produce the highest sensitivity it is best to work close to the Brewster angle for the sample [84]. For the range of refractive indices under investigation, n = 1.4 to 2, an average of 60° was calculated and was used for all the experiments.

Before each sample was run, a signal optimisation procedure was performed. The beam was set to 2.75 eV to enable a strong signal in the visible range for manual adjustment. The now visible beam could be placed onto a suitable region. This involved finding a region with minimal striation and no rough edges on the glass left over from the grinding procedure. After this, the stage was levelled using a microscope with cross-hairs for alignment situated above the sample. The now levelled samples were optimised for height by adjusting the stage until a maximum in signal was found. The maximum signal gain was optimised using a signal optimisation within the DeltaPsi software, producing a signal between 60-80 mV.

Once the sample signal had been optimised, scans were run from 350-850 nm using 3 measurements of 1000 ms per 10 nm step in wavelength this was done to maximise the signal to noise ratio. This whole procedure was performed 3 times per sample. For each sample set, 3 samples were run to ensure a good average was acquired. The spectral range was selected, due to machine limitations, into the NIR. The raw data from the ellipsometer converted into a refractive index directly using a substrate analysis against wavelength as given in Section 2.3.3.3.2 using equations (27-29). The data were converted directly using the DeltaPsi2 software. Converted RI values for each of the three scans were extracted from each of the three raw data sets, producing 9 scans per sample set. These 9 data sets were averaged per sample.

3.5.2 Absorption measurements UV-Vis and FTIR

UV-Vis and FTIR spectroscopy were performed using a Perkin Elmer Lambda 900 UV-Vis-NIR spectrometer and a Perkin Elmer Frontier FT-NIR/MIR spectrometer respectively. Both machines were turned on and left to stabilise for 1 hour before use, allowing the lamps to warm up.

Glass absorptions were measured using sample preparation given in Section 3.3.2. Three samples were used for each scan to check for any anomalies and the same samples were used for each machine. A background from an empty sample holder was also taken such that any influence of the lamp, detectors or atmosphere could be removed. Samples were then placed into flat sample holders and secured using Blu-tack™ to hold the sample flat and parallel to the beam. FTIR scans were run at a 4 cm^{-1} resolution 5 times before averaging. UV-Vis was scanned from 3300 nm to 180 nm. FTIR was scanned from 1000 nm to 25000 nm. The raw background subtracted data were exported from both machines and overlaid.

3.6 Physical Analysis

3.6.1 Density

Glass samples were measured using a Mettler Toledo density measuring kit employing Archimedes' principal. Three samples from each glass were measured and averaged; sections of Advantex E-glass and R-glass were also measured for comparison.

Resin densities were measured using an AccuPyc II 1340 Pycnometer and a 1.2789 cm^3 cell with 25 purges of He gas.

3.6.2 X-ray diffraction (XRD)

Powder XRD was performed on samples to check for any crystallinity using the procedure described in Section 3.3.3. Samples of the powder were then poured into a sample holder and levelled using a glass slide to produce a relatively smooth uniform surface before loading into the machine.

A Siemens D5000 XRD with $CuK\alpha_{(1+2)}$ radiation was scanned at 0.4º 2θ/minute over 15-60º 2θ. The resulting traces either exhibited a single broad peak typical of amorphous materials, or contained sharp peaks from crystalline material.

Material from phase separated H3 samples were scanned on a Bruker D2 machine. Phase separated samples were scanned as a solid and powder.

3.6.3 X-ray florescence (XRF)

XRF was performed at AMG superalloys .Ltd to investigate the differences in final composition of H3 glass produced in a mullite or Pt crucible. Samples were prepared as stated in Section 3.3.3.

3.6.4 Ultrasonic modulus measurements

Glass modulus measurements were performed on flat parallel samples by measuring the time of return signal in the longitudinal and shear orientations. Measurements were taken with an Olympus EPOCH 600 ultrasonic flaw detector. A 20MHz Olympus M208-RM longitudinal transducer and a 5MHz Olympus

V157-RM shear transducer were used for the longitudinal and shear reflection time measurements respectively. A contact solution of glycerine was used for longitudinal measurements whilst an Olympus shear wave couplant was used for shear measurements. The initial reflection peak was too strong and thus the second and third peaks were used for measurement.

$$Velocity = \frac{Thickness}{Round\ transit\ time/2} \qquad \textbf{(30)}$$

Velocity in either the longitudinal V_L or transverse V_T (shear), Poisson's ratio ν, Young's modulus (E) and shear modulus (G) are given by:

$$\nu = \frac{1-2\left({V_T}/{V_L}\right)^2}{2-2\left({V_T}/{V_L}\right)^2} \qquad \textbf{(31)}$$

$$E = \frac{V_L^2\rho(1+\nu)(1-2\nu)}{1-\nu} \qquad \textbf{(32)}$$

$$G = V_T^2\rho \qquad \textbf{(33)}$$

3.7 Thermal Analysis

3.7.1 Differential thermal analysis (DTA)

DTA was performed on a Perkin Elmer DTA STA 8000 machine. DTA operates by maintaining a constant heat flow and measuring the temperature difference between the sample and a reference.

Glass samples were prepared using the procedure given in Section 3.3.3. Approximately 50 mg of glass was added to a Pt pan, next to another Pt pan containing Al_2O_3. Al_2O_3 was used as a baseline materials to act as medium for heat transfer similar to the glass. The thermal stability of Al_2O_3 over the temperature range of interest provided an ideal baseline for the test. Samples were heated in an atmosphere of air from room temperature to 1200 °C at 10 °C/min. As the pans were heated the differences were measured and a graph of ΔH vs temperature was plotted. As the sample passes through a glass transition (T_g) point an endothermic dip occurs over the glass transition range and crystallisation appears shown as an exothermic peak. The glass transition and crystallisation temperatures were determined using Perkin Elmer’s Pyris software. T_g was calculated by taking the onset of the endothermic dip and any peak crystallisation temperatures were obtained using Pyris’s maximum point function.

3.7.2 Differential scanning calorimetry (DSC)

DSC was performed using a Perkin Elmer DSC 8500. Isothermal DSC involves the heating of two pans; one containing a sample and the other empty. The DSC measures the energy required to maintain a constant temperature, so any reactions causing endothermic or exothermic peaks affect the energy input into the DSC heating. The resulting traces give the heat flux versus the time. When examining an epoxy system isothermally, the exotherm of reaction is monitored with respect to time. Using the following equation the extent of conversion (α) is given by [3, 110]:

$$\alpha = 1 - \frac{\Delta H_t}{\Delta H_T} \qquad \textbf{(34)}$$

where ΔH_t is the cumulative enthalpy of the reaction at time t, ΔH_T is the total enthalpy of the reaction.

Uncured resins, samples were mixed using the procedures stated in Section 3.4. A small drop of resin between 5-10 mg was added to the DSC aluminium pan and weighed. A lid was added to the pan and pressed shut sealing the sample within. Samples were loaded using a vacuum system into the DSC cell and each time the pan was checked for any leakages that may have occurred. Samples were ran in a nitrogen atmosphere. 828 with TETA was left for 12 hours at 20°C whilst MY721 with DDS was left at 200°C. Raw data was extracted and processed using the integration function in Origin 8.1.

3.8 Fibre formability

Glass fibre forming requires a window known as ΔT, which is the difference between the suitable fibre drawing melt viscosity and the liquidus point. The liquidus point is the temperature at which for a given time scale, no crystals form in the melt in an equilibrium state [34]. To determine these values the $\log(\eta/\text{Poise})=3$ fibre forming point was taken from a viscosity trace and liquidus was determined using the following procedures:

3.8.1 Viscometry

Viscometry was measured using a Brookfield DV-III Ultra Rheometer shown schematically in Figure 26. The crushed sample was placed into an alumina crucible and heated using the regime in Table 15. Once the glass was up to temperature an alumina spindle was lowered into the melt and the torque was measured. From this the Rheoloader software supplied by Brookfield logged the torque and resulting viscosity against the temperature. After this scan, the crucible was heated back up to 1450°C to enable removal of the spindle. From this the melt was allowed to cool slowly to room temperature to prevent fracture of the crucible.

Table 15 Procedure for measurement of glasses viscosity using Brookfield DV-III Ultra Rheometer

Procedure		
Dwell	Hold at 15 °C for 90 min	Start furnace initialise program
Ramp	15 °C to 750 °C at 5 °C/min	Quick ramp to temperature - No spindle
Ramp	750 °C to 1450 °C at 1 °C/min	Slow ramp to temperature - No spindle
Dwell	Hold at 1450 °C for 15 min	Lower spindle into melt
Ramp	1450 °C to 1000 °C at 2 °C/min	Measure spindle torque
Ramp	1000 °C to 1450 °C at 5 °C/min	Remove spindle
Ramp	1450 °C to 20 °C at 3 °C/min	Cool to room temperature

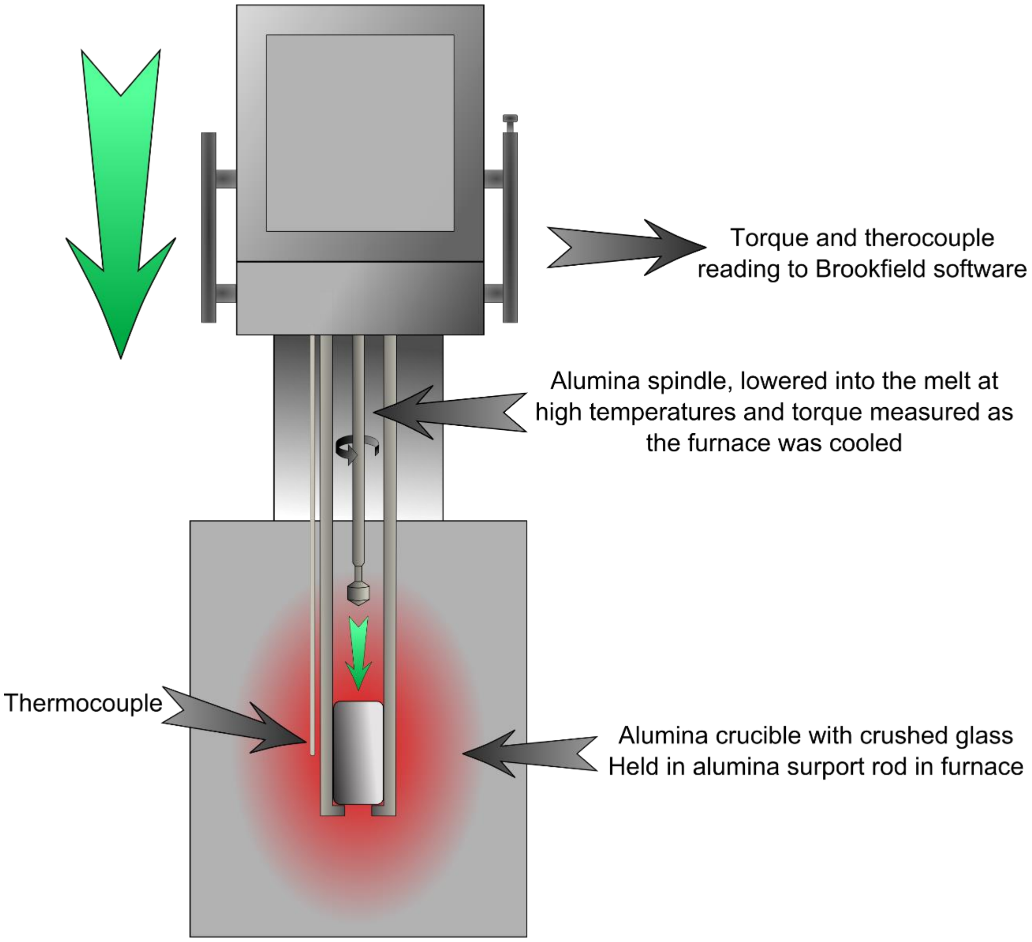

Figure 26 Diagram of Brookfield DV-III Ultra Rheometer

3.8.2 Liquidus measurements

The liquidus point was measured using a thermal gradient liquidus furnace with a 17 cm mullite “boat” crucible as shown schematically in Figure 27. The liquidus furnace is a narrow wound tube furnace such that a large temperature gradient extends from the centre of the furnace. Samples of crushed glass were placed along the entire length of the crucible and ramped at 3 °C/min to the desired set point and left to dwell for 24 hours. During the 24 hour dwell time, temperatures were measured along the length of the crucible at 1 cm intervals. Readings were taken at a minimum of 10 minute intervals to enable the thermocouple to equilibrate. After a 24 hour dwell the crucible was removed from the furnace using tongs, and air quenched.

After the sample had cooled to room temperature the crucible was measured from the end (where the initial thermocouple reading was taken) to the first point of crystal growth along the crucible. This was performed three times to an accuracy of ±0.1 mm to ensure consistency. The measured values of distance from the end of the crucible versus the temperature were plotted in Microsoft Excel and a line of best fit obtained. The equation of the line of best fit of the furnace temperature profile was then calculated using the value obtained from the sample, the resulting value was taken as the liquidus temperature.

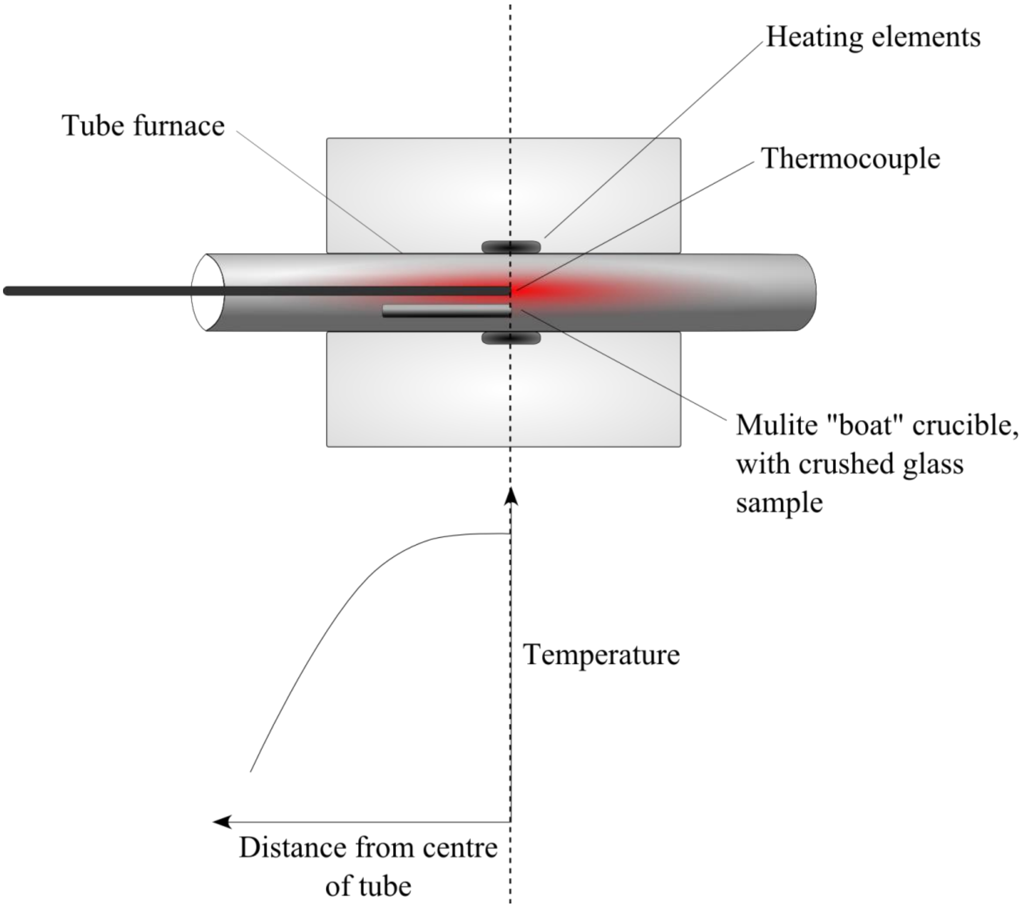

Figure 27 Schematic of the liquidus furnace

3.9 Fibre Production

3.9.1 Up-drawing fibre glass jig production

Reinforcing fibres are commercially produced using a down-drawing technique through a Pt bushing as discussed in Section 2.3.2. This gives many advantages such as continuous stable production and the ability to apply a sizing. However, due to the lack of availability of a down drawing facility and their batch size requirements, a glass fibre up-drawing jig was produced. The fibre drawing jig encompassed a vertical tube furnace with cut furnace bricks added down the tube, this was done to provide a bed for the crucible in the centre of the hot zone. An adjustable guide wheel was placed above the melt to run the fibre towards the fibre winder drum. A fibre winder and controller were taken from a decommissioned optical fibre drawing tower. The winder consisted of several detachable 1 m diameter polystyrene drums for multiple runs, fibre storage and a controller which could control the drum speed and move the drum side to side to enable winding onto the entire length of the drum. Due to issues of an extended hot zone, a closed loop water-cooling system was constructed using a submerged pump in a large water bath. The pump was connected to a set of reducing diameter copper pipes to an 8 mm diameter, 1 mm wall thickness copper pipe which was shaped into a coil. This was held above the melt using a lab stand so that it resided just above the hottest part of the furnace. The outlet from the coil was returned to the water bath which was cooled using a water cooler. The setup is schematically shown in Figure 28.

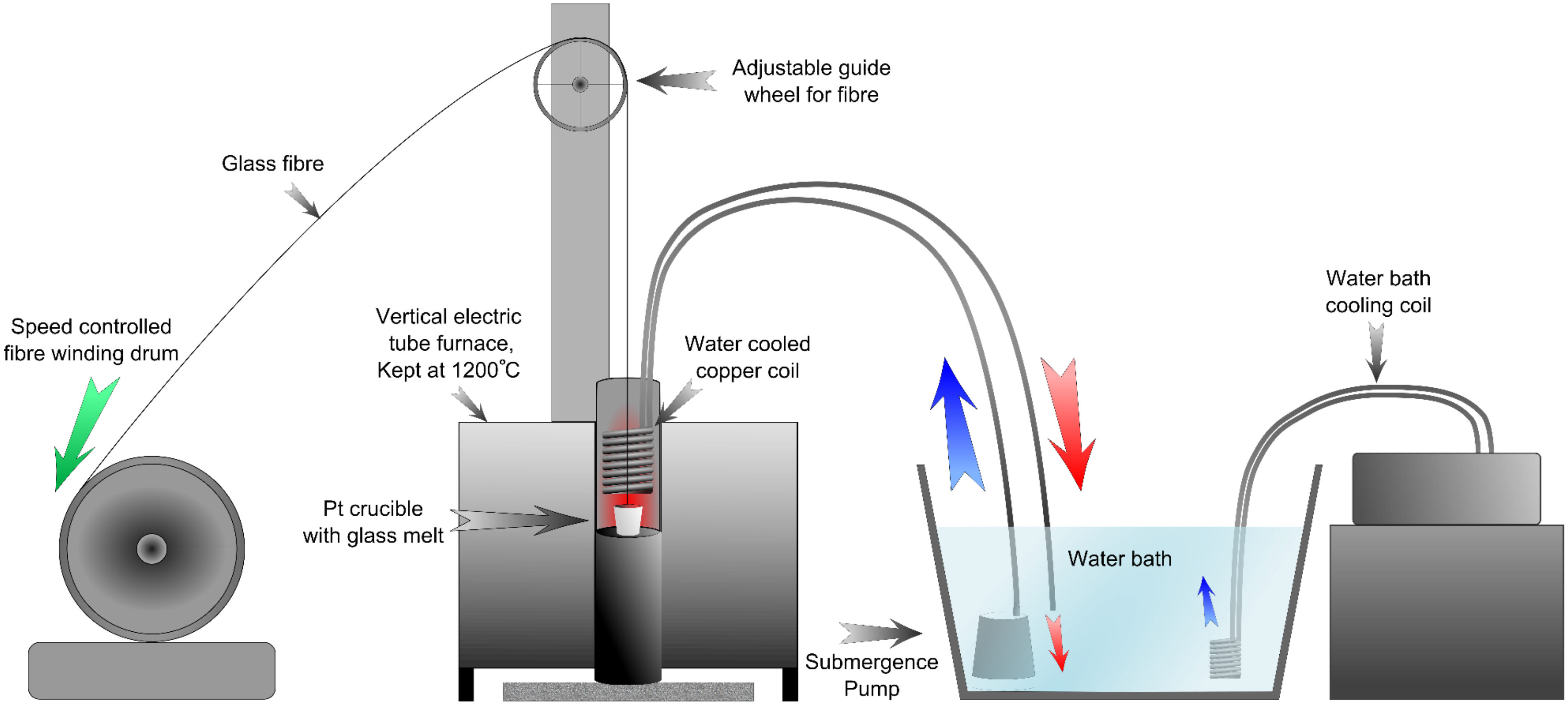

Figure 28 Layout of glass fibre up-drawing system.

3.9.2 Up-drawing jig operation

Glass cullet was added to a 110 mm by 50 mm diameter Pt crucible and ramped up at 2 °C/min to 1200 °C the night prior to fibre drawing. The cooling coil was placed above the melt and the height was adjusted to ensure that a stable fibre could be drawn out of the furnace. Two persons were required to operate the jig. One person would draw an initial fibre using a 10 mm diameter silica rod, which was dipped into the glass melt and drawn out by hand through the cooling coil. Once a stable fibre was drawn it was passed over the guide wheel and the second person would snap the fibre at the thin point beyond the silica rod. The fibre was then taped to a spinning drum, which continued to draw the fibre from the melt. The drum speed could then be increased, producing the highest output and finest fibre without causing fibre failure.

3.9.3 Drum speed

The polystyrene drums used for fibre winding were 1 meter in circumference. The drum speed was adjusted using a multi-turn potentiometer with an arbitrary scale. To calibrate the drum speed, speed measurements were taken at 25 potentiometer values from 50 to 500 as indicated by the potentiometer dial, actual speed was taken using a non-contact tachometer. The rpm was converted to drum speed, plotted and a trend line fitted to give the speed of the drum at any potentiometer value (Figure 30). At lower potentiometer values the dip in the data most likely occurred from the inaccuracy of the tachometer at low rpm values.

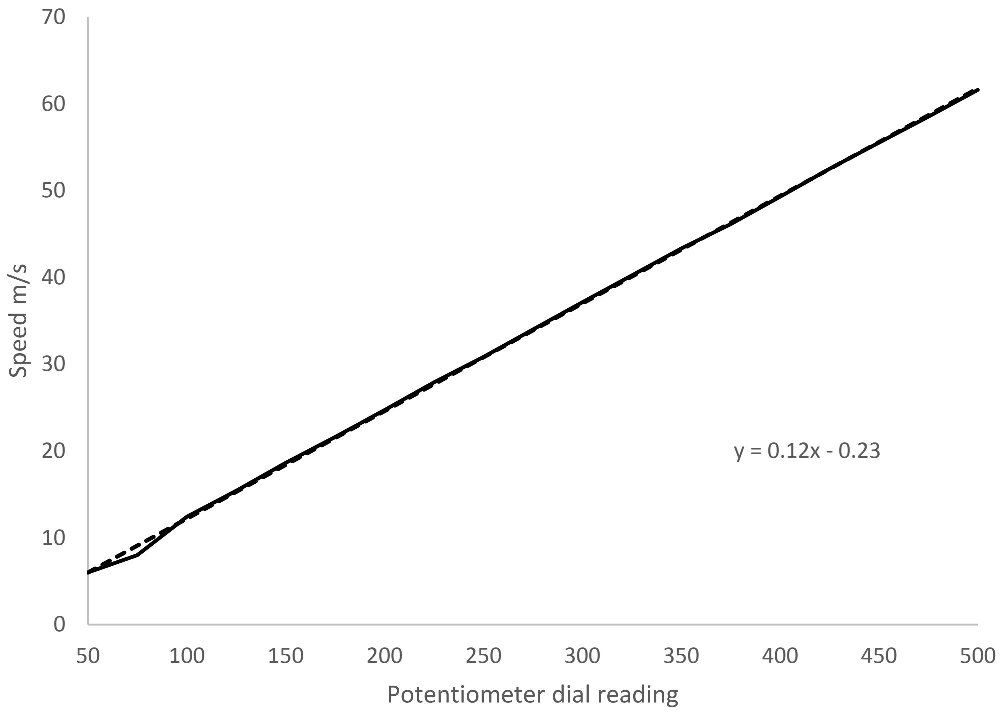

Figure 29 Graph of potentiometer value versus drum speed

3.9.4 Furnace temperature measurements

To give an accurate temperature profile for the furnace during fibre drawing, 5 N-type thermocouples were placed 30 mm away from each other down the centre of the cooling coil starting from approximately the top of the melt, as is shown in Figure 30.

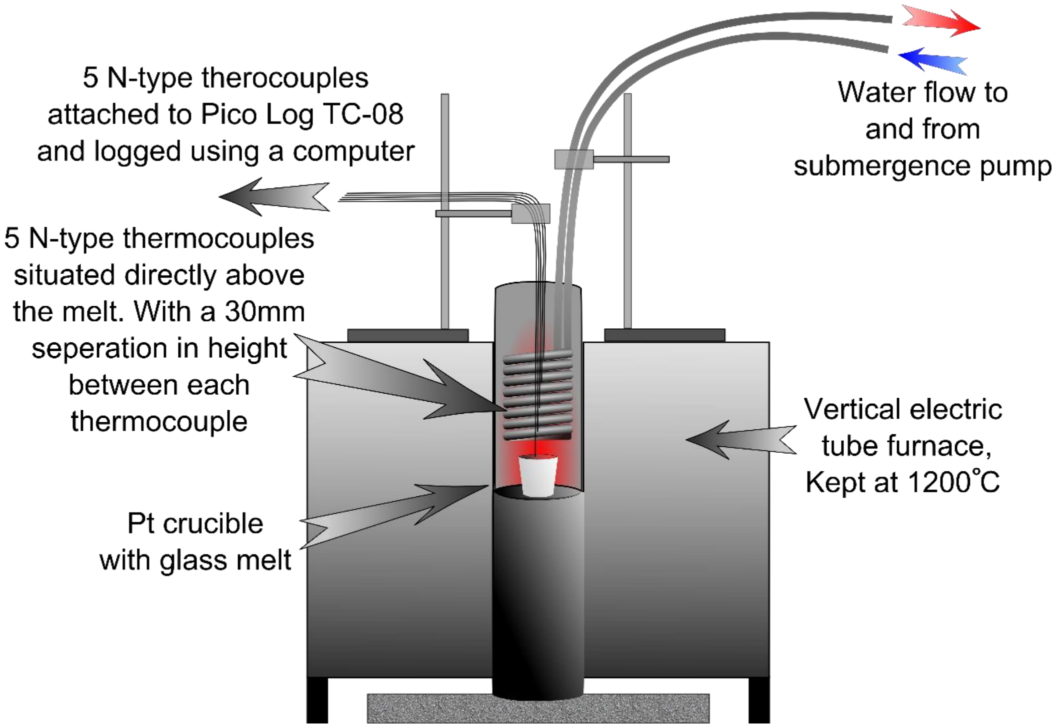

Figure 30 Diagram showing how furnace temperature profiles were taken.

During the fibre drawing process it was impossible to place the thermocouples down the furnace, due to the potential for disrupting the fibre drawing process. As a result, after the fibres were drawn, the furnace was given time to reheat up to 1200 °C without the cooling coil. The cooling coil was then reinserted at its previous position, which had been maintained using the lab stand, and the thermocouples were placed inside the cooling coil approximately where the glass level had previously been. From here the 5 thermocouples were logged using a Pico Technologies TC08 set to sample once every second using the PicoLog software.

3.9.5 Fibre drawing tests

Samples were trialled using two techniques:

- Placing a cooling coil at a set height and leaving it for 45 minutes causing the furnace to drop to a static homogenous temperature.
- Place the coil close to the melt providing a sharp temperature drop and fibre drawing before the melt thermally homogenised.

Two glasses were selected for fibre drawing due to availability.

- Na:Ti:Si
- H3 Pt

3.9.6 Fibre diameter measurements - Optical Microscopy

Fibre diameters were measured using a Nikon Eclipse LV150 optical microscope. Samples were prepared by cutting segments off the roll about a meter away from each other to better average the fibre diameter over the length of the drawn fibre. 7 samples were then taped to a glass slide to ensure the fibres lay flat. A 10x or 5x zoom was used to measure a larger proportion of the fibre. Images of each fibre were captured and 3 fibre diameter measurements were taken using the Buehler Omnimet 9.5 software. From these datum, average diameters and standard deviations were calculated.

3.10 Near infra-red spectroscopy experiments

The aim of these experiments was to demonstrate H3 fibres were capable of cure monitoring by fibre evanescent wave spectroscopy (FEWS). FEWS was performed by passing a NIR spectrum through a bundle of fibres covered in a curing resin and analysing the resulting absorption spectrum. A Bentham spectrometer was setup in a variety of techniques enabling investigation of fibre absorptions performing fibre loss spectrums. Baseline scans of samples were taken through custom-made cuvettes. FEWS liquid samples were then performed on each end of the epoxy RI index spectrum and finally FEWS cure monitoring of a thermoplastic toughened carbon pre-preg was performed. The following experimental details will explain each setup listed below:

- Fibre loss spectrums
- Baseline resin scans
- Liquid epoxy resin cure monitoring by FEWS
- Electrically cured PMC with FEWS cure monitoring

The justification of baseline resin scans is to check for the ideal peaks for cure monitoring. For all of the experiments stated above a baseline scan was required such that any glass absorption could be removed revealing the evanescent wave spectrum. For all of the experiments an initial averaged spectrum of the cuvette or H3 fibre bundles was taken prior to the experiment.

3.10.1 NIR Optical setup

Fibre spectroscopy was performed on a Bentham optics M300 monochromator with a 600 grooves/mm G306R1u25 diffraction grating. A Hamamatsu P9217-03 PbS detector was produced and linked to the relevant Bentham amplifiers. The setup was controlled through the Bentham Optics BenWin+ software. The setup is schematically shown in Figure 31:

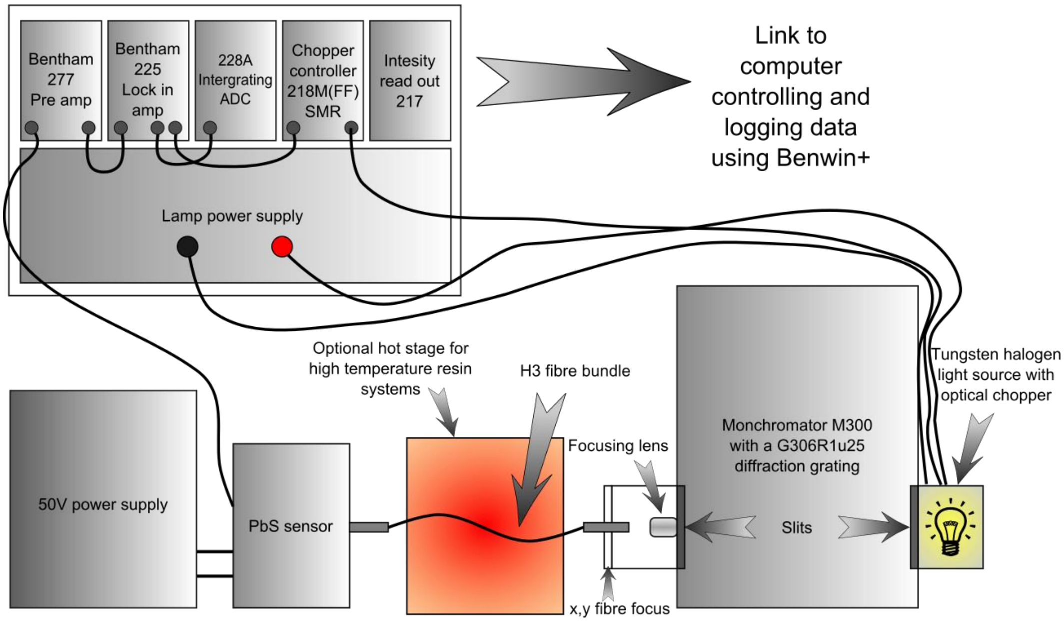

Figure 31 Bentham fibre spectrometer set up.

Before any scans were made, the lamp was given a minimum of 5 minutes to warm up. The bandwidth of the light was adjusted for each experimental setup optimising the signal level whilst maintaining the smallest possible bandwidth. This was adjusted using the slits either side of the M300 as shown in Figure 31. The bandwidth for each experiment is stated with corresponding experimental procedure.

3.10.2 Data Acquisition

Scans were run with 5 samples being taken per reading at 0.5 sec per reading with 10 nm scan steps from 1000-2500 nm. Scans were run a minimum of 2 times to rule out any anomalies, enabling averaging. Following setup and acquisition of the background scan, the samples were then scanned hourly using BenWin+ software's schedule mode enabling periodic scanning, before being exported into Microsoft Excel for analysis.

3.10.3 Signal optimisation

Before each experiment an optimisation procedure was run using the signal setup within Benwin+. The signal setup was set to wavelength "0 nm" to produce the entire spectrum from the light source. The 277 pre amp and 225 lock in amplifier were set to manual and the 277 unit was set to a gain range such that a reading could be seen on the 217 unit. This was followed by some rough sensor alignment to facilitate focusing of the launch optics. The focusing lens was adjusted to maximise the signal level. The next procedure was to adjust the X, Y stage at the fibre launch lens to again maximise the signal. Following this the lock-in amplifier was set to the 90° phase quadrant and was adjusted using the phase offset control to a zero value. This produced a maximum in the 180° phase, and the resulting phase offset value was inputted into the Benwin+ software for the rest of the experiment. This procedure is demonstrated in Figure 32.

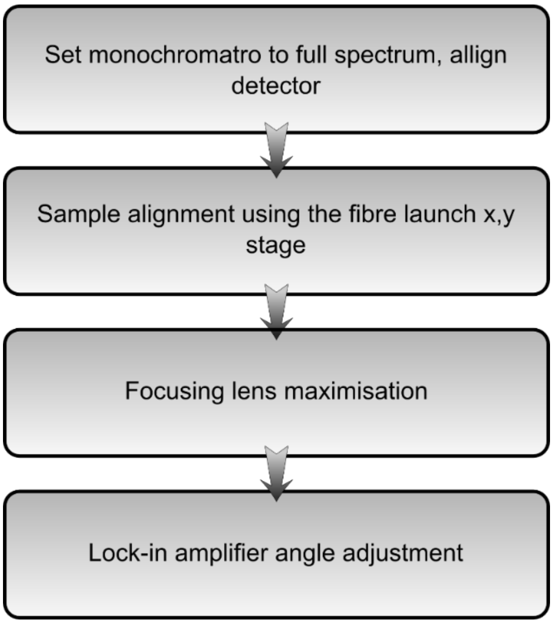

Figure 32 Bentham signal optimisation procedure.

3.10.4 Fibre loss spectra

Fibre loss spectra were gathered using a range of samples shown in Table 16. Samples were loaded into the Bentham launch optics using a variety of brass collars. Upon the initial scan the fibres were tensioned around a roller and cropped using a fresh scalpel. In the case of embedded fibres one end was cropped using a diamond saw and then ground and polished using a 1200 grit SiC paper and 6, 3 and 1 µm diamond polishing paste.

Table 16 H3 fibre samples for fibre loss spectrums

Setup	**Initial fibre length (mm)**	**Cropped fibre length (mm)**
Single H3 fibre	200	-
H3 Fibre bundle (20 fibres)	170	130
H3 fibre bundle (20 fibres) in 828 TETA	133	107

Four scans were taken of each sample length and averaged. The averaged scans were converted into loss spectra using the Beer-Lambert equation [111] and plotted against wavelength:

$$A = \left(\frac{10}{L}\right) - 10\log_{10}\left(\frac{Initial}{Cropped}\right)(dB) \qquad \textbf{(35)}$$

where L is the difference in length between initial and cropped per unit length.

3.10.5 Baseline/Comparative FEWS data

To enable accurate comparison of FEWS scans to a baseline samples were prepared into custom-built cuvettes show in Figure 33. Standard disposable cuvettes of polystyrene produced peaks in the NIR region and all available silicate cuvettes were very expensive and thus unsuitable for curing resin within them, making them effectively single-use. Custom-built cuvettes were produced by sectioning glass microscope slides using a diamond saw. These sections were then bonded at right angles using Araldite slow cure epoxy adhesive. They were held in place at right angles during curing by machined aluminium blocks covered in polytetrafluoroethylene (PTFE) coated glass fabric. Upon curing sections they were bonded to each other and post cured for 24 hours at 50°C. Prior to the addition of any resins they were tested for leaks using IPA.

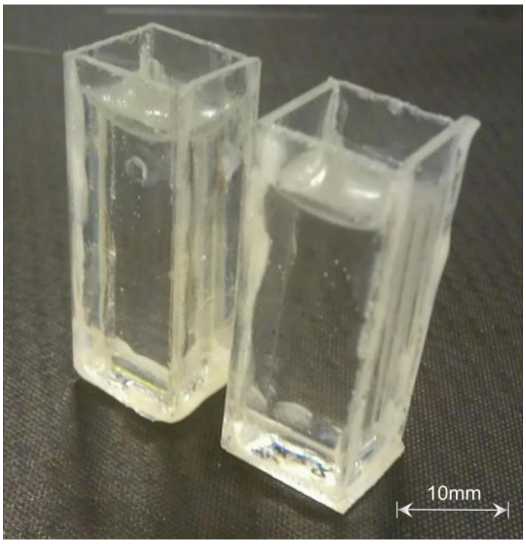

Figure 33 Cuvettes produced from glass slides and held together using Araldite two part epoxy adhesive.

For FEWS cure monitoring of electrically cured pre-preg experiments, a scan of NIR peaks of the raw resin was required for comparison. Acquiring the raw resin was not possible, so the resin was stripped from the pre-preg by solvent extraction using di-chloromethane (DCM) from Sigma Aldrich Ltd. A 4 x 5 cm^2 sample of MTC801 pre-preg from SHD composites was cut and added to 100 ml of DCM. The sample was left for 24 hours to extract the resin. After 24 hours the carbon fibre was removed and the remaining solvent resin mix was left in a fume hood for a week to allow most of the DCM to evaporate. Samples of MTC801 were cured at 120 °C for 3 hours with 2 °C/min ramps.

In a similar manner to FEWS experiments the cuvettes were scanned for baseline subtraction prior to sample addition. Samples of 828/TETA and MY721/DDS were cured according to the cure schedule given in Table 14.

Table 17 List of cuvette baseline experiments for comparison with evanescent wave spectroscopy experiments

Experiment	**Bandwidth (nm)**	**Temperature (°C)**
PEG 300	2	-
SFO	2	-
828/TETA	2	See Table 14
MY721/DDS	2	See Table 14
MTC801	2	120 °C for 3 hours with 2 °C/min ramp

3.10.6 Liquid epoxy resin FEWS

Liquid resin FEWS samples were produced by threading bundles of H3 fibres through 1 mm internal diameter PTFE tubing. After the bundles had been produced they were washed using acetone and IPA to remove any debris from the fibre. The fibre was then placed in a vacuum oven at 80 °C, under vacuum, for one hour and used immediately following this. Each piece of tubing was wrapped in two layers of heat shrink tubing to hold it in place in the fibre holder on the detector and fibre launch optics.

Liquid resins were prepared according to instructions given in Section 3.4. After signal optimisation of the fibres a baseline scan was taken of the H3 fibres. This baseline scan of the fibres was then used as the subtraction for the rest of the cure removing any artefacts from the glasses absorption. The prepared resin was then poured over the bare central section of the fibres. Any bubbles resting on the fibres surface were removed using a scalpel blade producing FEWS liquid samples shown in Figure 34.

Figure 34 Liquid resin FEWS sample

All samples were held in place using a PTFE coated Al plate on top of a lab stand; whilst MY721 samples were cured on a PTFE hot plate. A variety of samples were tested over and the experimental parameters are given in Table 18.

Table 18 List of FEWS experiments and the parameters used.

Experiment	Fibre length (mm)	Embedded length (mm)	No. Fibres	Average fibre diameter (µm)	STDev fibre diameter	Bandwidth (nm)	Temperature (°C)
PEG300	320	140	4	261.0	14.8	10	-
Sun flower oil	260	140	6	123.7	46.2	10	-
MY721 DDS	350	135	~20	87.0	20.1	10	200
828 TETA 1	200	65	4	299.0	15.8	10	-
828 TETA 2	270	70	4	214.0	63.0	10	-
828 TETA 3	300	125	6	120.5	11.0	10	-
828 TETA 4	290	130	18	55.8	15.1	10	-
828 TETA 5	300	135	24	54.8	18.4	10	-
828 TETA 6	350	125	24	97.1	22.2	10	150

3.10.7 Electrically cured PMC with FEWS cure monitoring

For cure monitoring of electrically cured panels MTC801 pre-preg supplied by SHD composites .Ltd was used. MTC801 was used due to a low resin viscosity and being a thermoplastic toughened system it was considered to be of interest to investigate what role the thermoplastic plays on FEWS. 4 plies of MTC801 were sectioned into 100 mm^2 pieces and laminated to give a [0,90]s structure with the H3 fibres bundle being placed in the centre of the laminate. 4 copper electrical contacts of 100 mm by 30 mm were cut and soldered between 2 contacts. These contacts were wrapped around the end of the panel with a 10 mm contact area over the strip.

The H3 fibre bundles were placed in the centre of the ply stack with a 10 mm overhang of PTFE tubing. This was also sectioned 5 mm up the tube to allow the tube to collapse. This was done to protect the fibre and upon resin flow to seal the tube fully, minimising leakage in the vacuum bag.

The 4 ply carbon composite with H3 fibres running through the centre was laminated onto a PTFE coated aluminium plate. This was followed by a layer of release film, thermocouples for control and breather fabric. This was all sealed inside of a vacuum bag using high temperature tacky tape as shown schematically in Figure 35.

Diagram of cure monitoring of electrically cured pannels

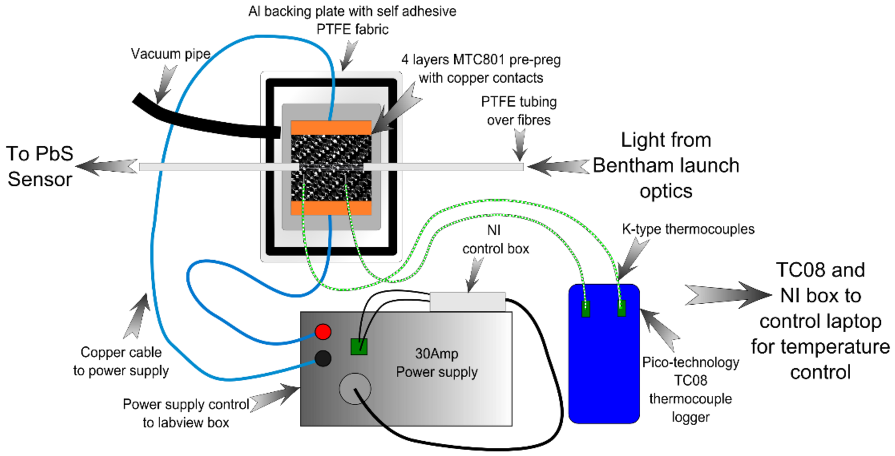

Side on view of bag

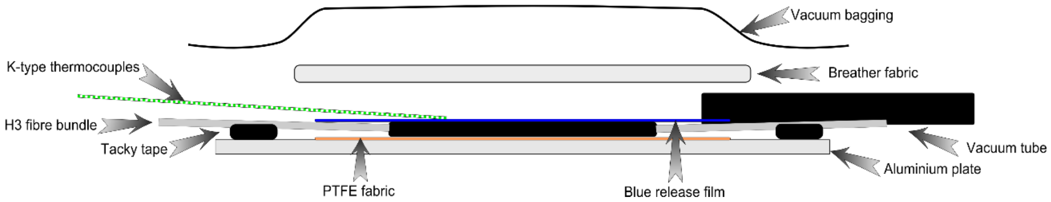

Figure 35 Schematic illustration of electrically cured FEWS cure monitoring panel

As Figure 35 shows the contacts were then wired to the 30 Amp power supply. This, in-turn, was controlled by a National Instruments USB6008 controller and a Pico-Technology TC-08 thermocouple logger. Both of these were plugged into a computer running a custom-built Labview program designed to control the electrical cure process. The program was set to cure for 3 hours at 120 °C with 10 °C/min ramps for heating and cooling of the part. The program set point and actual average attained thermocouple is shown in Figure 36.

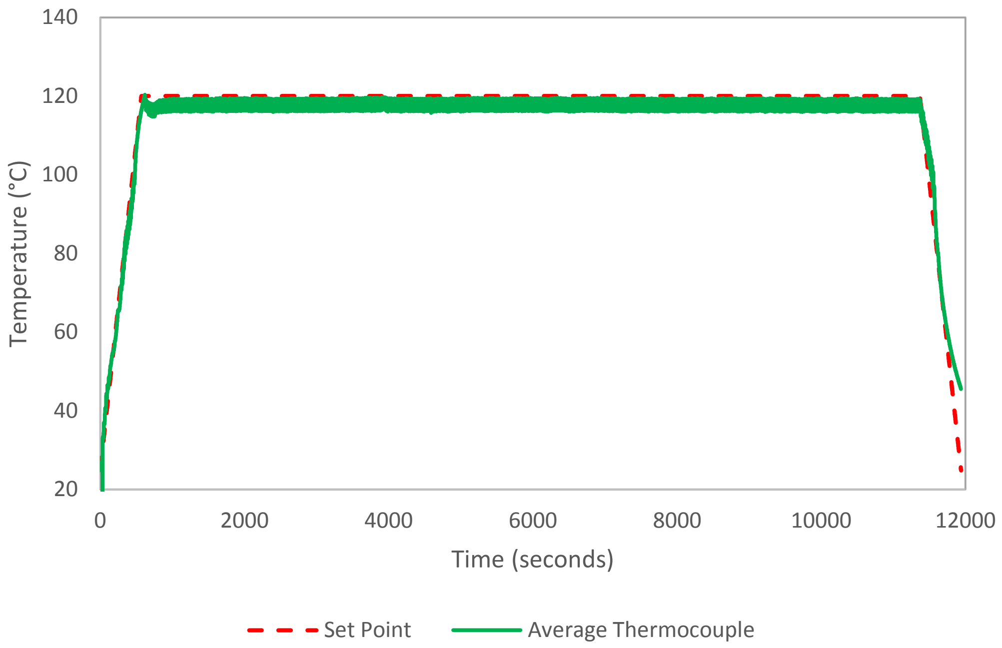

Figure 36 Cure schedule for electrical cure of MTC801 carbon pre-preg

A ramp rate of 10 °C/min is normally too high for epoxy resins, causing exothermic reactions; however, in the case of electrically cured parts every fibre acts as a resistive heater causing uniform though thickness heating. This prevents "hot spots" occurring and consequently even using these high ramp rates exothermic reactions have been found to have minimum influence [112]. The electrically cured FEWS cure monitoring experiment parameters are detailed in Table 19.

Table 19 List of electrically cured H3 FEWS experiments and the parameters used.

Experiment	**Fibre length (mm)**	**Embedded length (mm)**	**No. Fibres**	**Average fibre diameter (µm)**	**STDev fibre diameter**	**Bandwidth (nm)**	**Temperature (°C)**
MTC801	320	80	22	84.2	24.0	10	*Figure 36*
MTC801	300	80	26	87.8	24.0	10	*Figure 36*

3.10.8 Analysis of results

In order to analyse the FEWS data, it was necessary to process the data to remove the background features and reveal the peaks caused by absorption of the evanescent field.

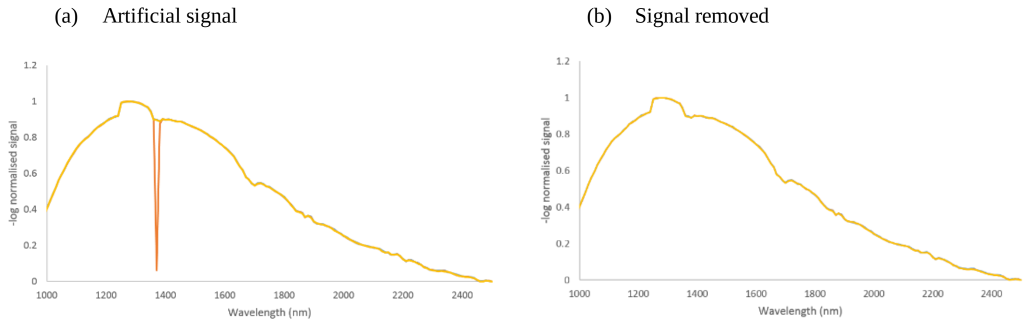
(a) Artificial signal

(b) Signal removed

Figure 37 Removal of artificial signal (a) before and (b) after overload removal.

The data from each set of scans would be examined for any artefacts/digital overloading. The PbS sensor worked on an inverse response which was compensated for by Bentham software. However, when the sensor was overloaded a signal of <0.001 nA was left in the data consequently, and all values less than <0.001 nA were discarded from the data as shown in Figure 37. The data were then normalised using feature scaling to the light intensity at 1670 nm to remove intensity variation due to fibre misalignment and resin RI increases during cure.

$$X' = \frac{X - X_{Min}}{X_{1670nm} - X_{Min}} \tag{36}$$

where X' is the normalised value, X is the original value, X_{Min} is the minimum value X_{1670nm} is the value at 1670 nm. The normalisation was performed at 1670 nm, as this encompasses the C-H aromatic vibration which will remain constant throughout cure [6, 12, 113, 114]. The scans were then averaged for each set. The final spectra were attained using Beer-Lambert law:

$$A = -10\log_{10}\left(\frac{I}{I_0}\right)(dB) \tag{37}$$

where I is the normalised and averaged spectrum per interval of time and I_o is the initial baseline spectrum of the optics, detector and glass absorptions to be removed leaving the absorption spectrum. The Beer-Lambert equation operates by sending the non-absorbing parts of the spectrum to zero, leaving only the absorption peaks. The processing is summarised in Figure 38.

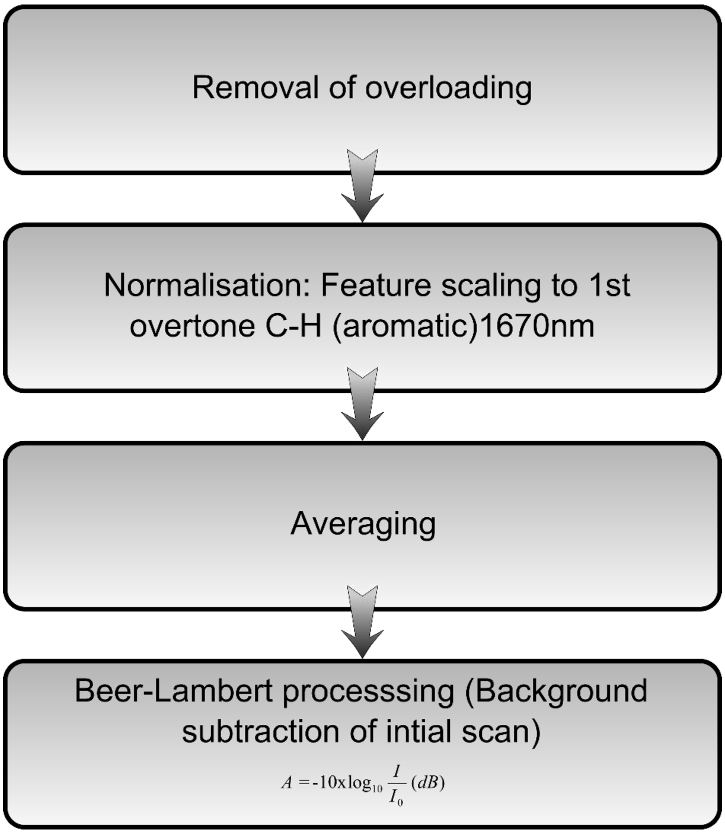

Figure 38 Processing of scans attained from the Bentham cure monitoring experiments to produce absorption spectrums

4 RESULTS AND DISCUSSION

4.1 Glass melts

Glass compositions were batched in accordance to Table. 5 and Table. 7 and melted using the procedures given in Table 9. Initially glasses were all poured straight from the furnace at 1450 °C; however, this produced striation of the block, caused by the cooling glass folding back on itself. In many of the H-glass family of glasses this was very apparent, which suggests local compositional variation within the melt.

The apparent visual appearance of the cast glass melts and hand fibre drawing tests are given in Table 20. All of the transparent sample glasses were scanned using powder XRD, whilst crystallised samples were not studied any further. XRD scans of the transparent glasses from Table 20 are shown in Figure 39, which gives the intensity versus the 2θ angle from 15 to 60°. All of the glasses showed a wide amorphous hump and a small peak at 27.4 2Θ degrees. This is presumed to correspond to the (0 1 1) quartz (SiO_2) peak [115]; however, there are not enough peaks for phase identification. The presence of this peak demonstrates a level of instability within these glass systems however, within the resolution of the experiment, they are all effectively X-ray amorphous.

The first section of Table 20 shows the alkali containing glasses. Both of the potassium niobium silicate (K:Nb:Si) glasses crystallised upon pouring blocks, however, samples were successfully splat quenched between two steel plates producing an x-ray amorphous sample. However, due to the instability of these samples, fibre drawing was not possible and they were consequently not investigated any further. The next attempted melt was a lithium niobium silicate (Li:Nb:Si) which was successfully cast, however hand drawn fibres were unsuccessful, containing “bobbly” crystallised sections which is expected in lithium silicates due to Li high mobility which limits the stability [116].

In order to impart a higher refractive index to the Li:Nb:Si system TiO_2 was added, but this resulted in instant crystallisation even via splat quenching. This result is not unsurprising considering Li’s high mobility and desire to crystallise [116]. The sodium titanium silicate (Na:Ti:Si) melt in mullite produced a dark amber x-ray amorphous sample however, no fibre drawing could be attempted due to use of a mullite crucible.

The alkali-free glasses, in general produced transparent material. Ca:Al:Nb:Si produced a clear block which was x-ray amorphous when casting. However, once the crucible had returned to processing temperatures and cooled to a suitable viscosity for fibre forming, the melt started to crystallise and only small sections of fibres, with crystallised regions, were formed, thereby demonstrating instability in the glass system. E-glass -5%Al + 5%Nb, H1 and H3 glasses formed transparent blocks and fibres were successfully hand drawn. It was decided to try and increase the refractive index by adding lanthanum oxide into H1, however the melt instantly crystallised upon pouring. After this, glass melts H2-H6 were all successfully poured producing x-ray amorphous samples. H3 melted in Pt, also produced successful fibres.

*Table 20. Visual appearance of melts and fibre draw.**

Composition	Appearance	Fibre drawing test results
3K:3Nb:5Si	C	Crystallised
2K:3Nb:5Si	C	Crystallised
Li:Nb:Si	T	Unsuccessful
Li:Ti:Nb:Si	C	Crystallised
Na:Ti:Si	T	N/A (Mullite)
Ca:Al:Nb:Si	T	Unsuccessful
E-glass -5%Al + 5%Nb	T	Successful
H1 Pt	T	Successful
H1 –Ti +La	C	Crystallised
H2 GM	T	N/A (Mullite)
H3 Pt	T	Successful
H3 GM	T	N/A (Mullite)
H3 EM	T	N/A (Mullite)
H4 GM	T	N/A (Mullite)
H5 GM	T	N/A (Mullite)
H6 GM	T	N/A (Mullite)

*****C = Crystalline T = Transparent Fibre drawing from mullite crucibles were not possible due to thermal shock and are labelled accordingly.

4.1.1 X-ray diffraction (XRD)

Figure 39 shows XRD scans of the transparent glasses with the intensity versus the 2θ angle from 15 to 60°.

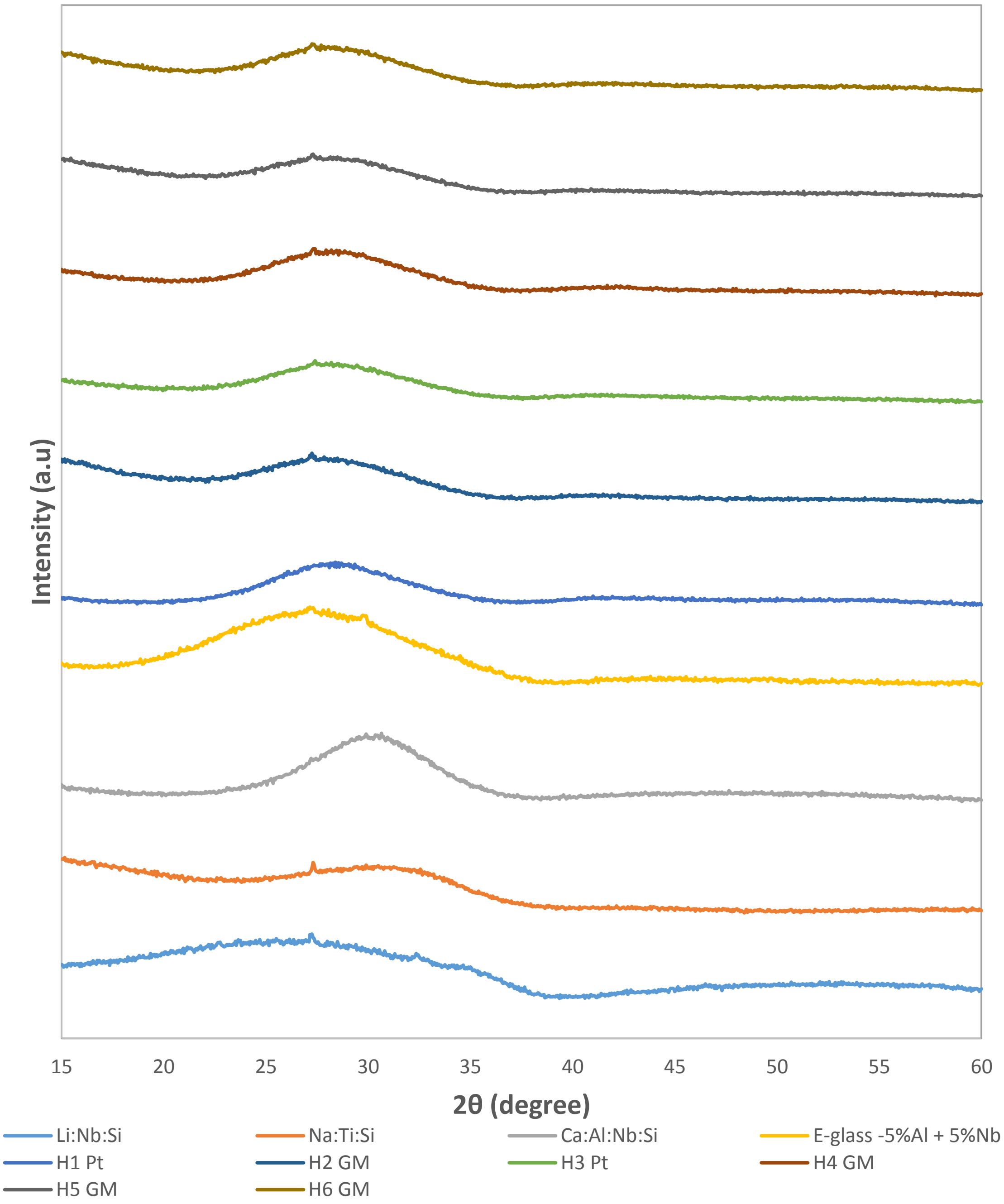

Figure 39 XRD plots of all transparent glasses

4.1.2 X-ray fluorescence (XRF)

For all of the alkali free glasses, when the batch was added to the crucible, parts of the batch would remain un-dissolved and stuck to sides of the crucible as demonstrated in Figure 40.

Figure 40 Undissolved batch left up the side of the crucible

The undissolved batch may have affected the final composition of the glass; however, even when a Pt paddle was used to knock off the remaining batch the undissolved batch remained firmly bonded to the side of the crucible. To minimise the issue, a maximum batch size of 300 g of glass was produced during each run.

Samples from the H-glass family were melted in both mullite and Pt. Samples melted in mullite produced a dark amber glass. To investigate the causes, elemental analysis was performed on H3 samples melted in either mullite or Pt using XRF.

Table 21 XRF compositional results in mol% for H3 melted in Pt and mullite with results normalised to expected H3 composition

Oxides	**H3**	**H3 Pt**	**H3 Pt ratioed to SiO_2, Fe_2O_3 and HfO_2**	**H3 ME**	**H3 ME ratioed to Al_2O_3, SiO_2, Fe_2O_3 and HfO_2**
Al_2O_3	1.04	0.97	0.99	3.67	3.77
SiO_2	52.08	54.07	55.18	54.66	56.15
CaO	9.38	9.11	9.29	8.36	8.59
TiO_2	10.31	9.60	9.80	8.98	9.23
Fe_2O_3	0.00	0.03	0.03	0.07	0.08
BaO	15.63	14.96	15.27	13.82	14.19
ZrO_2	2.19	2.10	2.14	1.93	1.99
SrO	6.25	6.09	6.22	5.64	5.79
HfO_2	0.00	0.02	0.02	0.02	0.02
Nb_2O_5	3.13	3.04	3.10	2.83	2.90

H3 Pt and H3 MG possess the same composition; however, the resulting mullite melted glass produced a dark amber glass.

The XRF of H3 Pt compositions demonstrate a 3.8 mol% increase in levels of SiO_2 and impurities of HfO_2 and Fe_2O_3. The impurities of HfO_2 and Fe_2O_3 can be explained due to HfO_2 impurities in Nb_2O_5 and ZrO_2 and additions of Fe_2O_3 from the constituent sand SiO_2. An increase in SiO_2 could be explained due to the constituent being a particle, rather than a fine powder, resulting in less of the constituent sticking to the weighing pan during batching in comparison with the finer powders of the other constituents. When normalised to these impurities, it is clear that the composition is close to the desired composition.

The XRF of H3 melted in mullite demonstrates a considerable increase of 253.6 mol% in Al_2O_3 and 175.7 mol% of Fe_2O_3 when compared to the expected impurities when melting in Pt. This is expected due to use of Al_2O_3 and Fe_2O_3 in the production of mullite. This demonstrates that the glass has attacked the mullite, resulting in a significant compositional change. When the resulting melts were normalised to the impurities, as shown in Table 21, a similar composition to the desired composition is produced within the error of the technique.

4.2 Refractive index measurements

4.2.1 RI measurement technique selection process

Initially RI measurements on epoxy resins were performed on a Bellingham and Stanley 60ED Abbè refractometer. Samples of cast epoxy on laser acetate sheets were placed on the refractometer with a contact solution of monobromonaphthalene. The contact solution produced two issues; the epoxy absorbed it warping the samples making the spectral lines hard to visualise, and due to the addition of monobromonaphthalene into the resin structure, the resins RI was artificially increased. This combined with the measurement limits of monobromonaphthalene at n_D = 1.65, which was on the upper end of the epoxy resins, the high variability in the measurement and human error interpreting the light dark boundary, all contributed to inaccurate unrepeatable results. Consequently, ellipsometry was examined as a measurement technique.

4.2.2 Ellipsometry

4.2.2.1 Data analysis

As stated in Section 2.3.3.3, ellipsometry can be used to measure the refractive index of a material by determining the final polarisation state of a reflected polarised light. In the case of a single layer system, the data can simply be converted into direct values using the method shown in Section 3.5.1. It is normally suggested in user guides/manuals [83-85] that all data should be modelled, accounting for issues such as back side reflections and surface roughness. However, in this study, the backside reflections were manually removed via roughening and painting the reverse side of the sample. The addition of surface roughness to the model was an attempt to correct for the absorption. However, all of the samples measured contained a varying level of amber colouration which, when using many of the models, conflicted and thus produced RI matches with a low goodness of fit. The use of modelled data with weak absorptions were tested, but in all cases modelling only ever produced a smoothing effect to the refractive index whilst trying to account for absorptions. Consequently, it was decided that as modelling only provided an artificial smoothing to the required RI measurement, a direct conversion was the most representative of the actual sample RI, as suggested by reference [83].

4.2.2.2 Calibration and sample optimisation

Initial ellipsometry results showed a considerable RI offset for samples of Advantex and fused silica from the literature [31]. Samples covering a range of RI values were purchased to see how uniform the offset was, with data for the refractive index being quoted at distinct spectral lines. To relate this data to ellipsometry at 10nm intervals, a line of best fit using a polynomial line of order 6 in Microsoft Excel was used to plot a line through the existing RI data. The equation of this line was used to plot wavelength values every 10nm. Due to the inability of polynomials to extrapolate data accurately, data was only plotted within the measured data range.

Table 22 Calibration glasses used for ellipsometry measurements.

Calibration Glass	**RI n_D (589.3nm)**
Fused Silica (FS)	1.45838 [61, 117]
N-BK7	1.51673 [118]
N-SK10	1.6227 [119]
N-SF10	1.72803 [120]
N-SF6	1.80491 [121]

The samples were then measured according to sample measurement and averaging technique given in Section 3.5.1. The final value was subtracted from the reference value giving an off-set value Δn.

The averaged offset for all of the references samples showed an offset of 0.096 on the refractive index over the entire range. This was corrected after an angle calibration had been performed by Horiba, accounting for this offset. After angle adjustment, samples were reanalysed to give the error plots shown in Figure 41, which were produced by measuring the RI for each reference sample 3 times in three positions on the sample. The data was then averaged and subtracted from the reference data for each glass over the 400 to 800nm range giving the difference in RI Δn versus wavelength. This demonstrated an error of RI of ±0.015 over the 400-800nm range with the exception of SF6 which starts off within the range and increases up to an offset of 0.02 in the low wavelength region.

To investigate if the ellipsometer tolerances were of a standard level, samples of FS, N-BK7, and N-SF6 were all sent to Horiba (manufacturer of the ellipsometer used in this work) to test for accuracy using two different ellipsometers (Horiba 1 and Horiba 2). Data was scanned once using three accumulations per sample for Horiba 1 samples, whilst Horiba 2 samples were scanned once with one accumulation. The Δ and Ψ values for Horiba 2 samples were not directly converted and were consequently calculated in Microsoft Excel. Error bars are shown for each scan, apart from those obtained from Horiba 2 where only one scan was taken. Results of the reference values minus the ellipsometry values for samples FS, N-BK7, and N-SF6 are shown in Figure 42, Figure 43, and Figure 44 respectively.

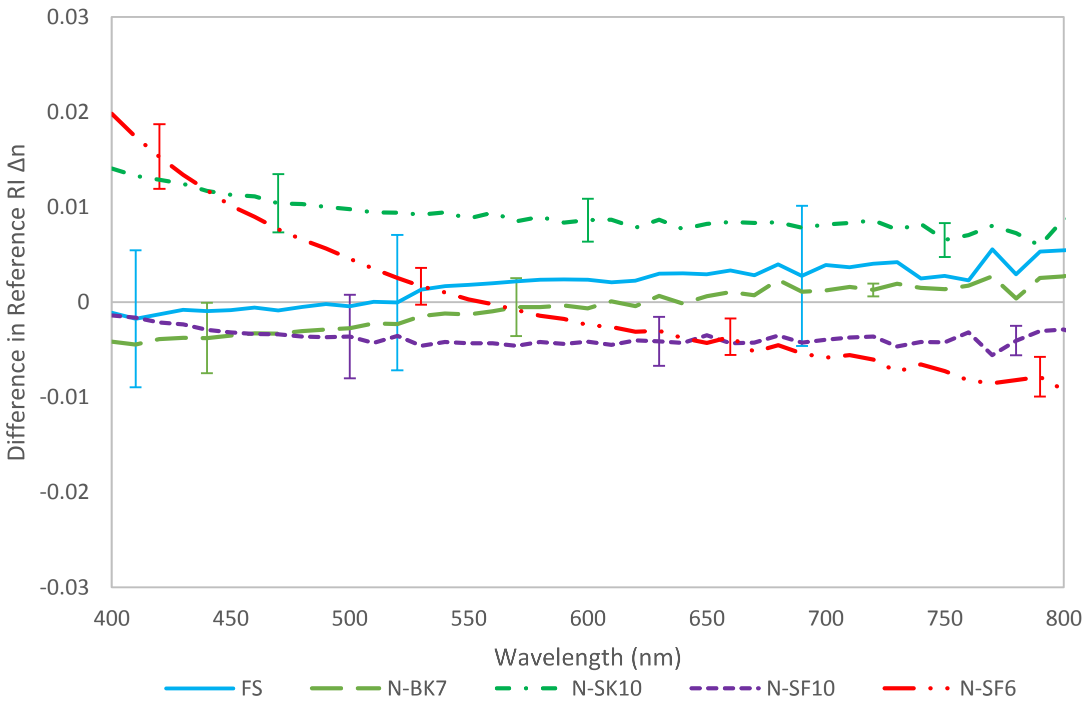

Figure 41 The RI reference of a sample minus the actual measured RI using the Sheffield ellipsometer for FS, BK7, SK10, SF10 and SF6 as a function of wavelength 400-800nm. Error bars show 1 standard deviation.

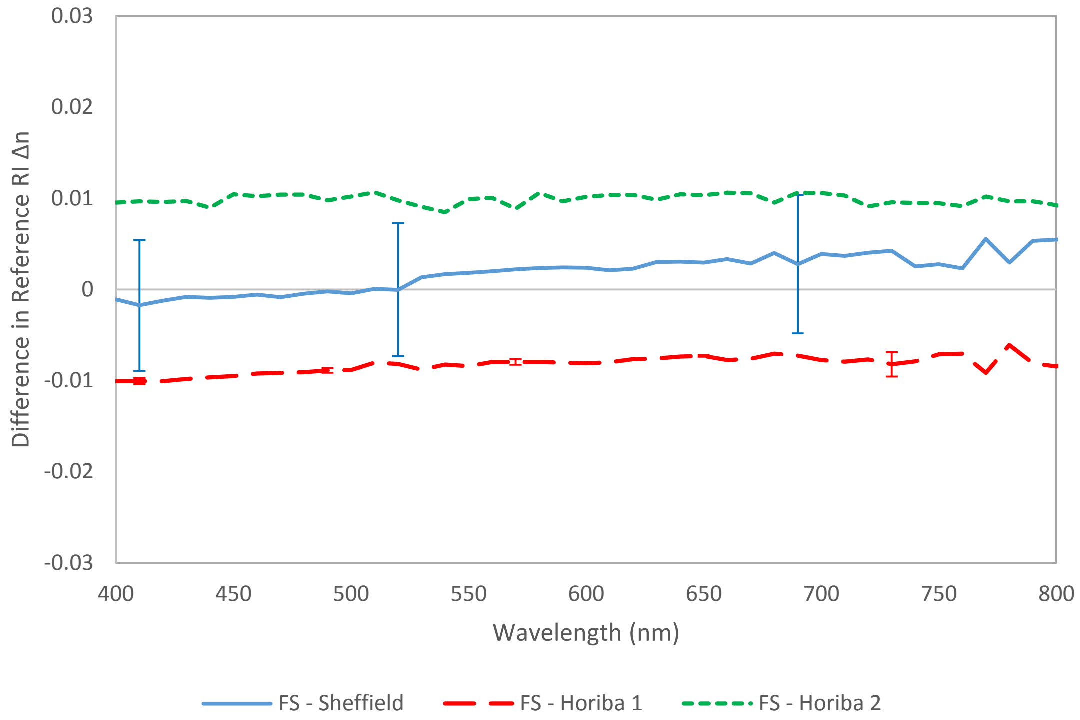

Figure 42 Error in measured RI as a function of wavelength for FS using Sheffield, Horiba 1 and 2 ellipsometers

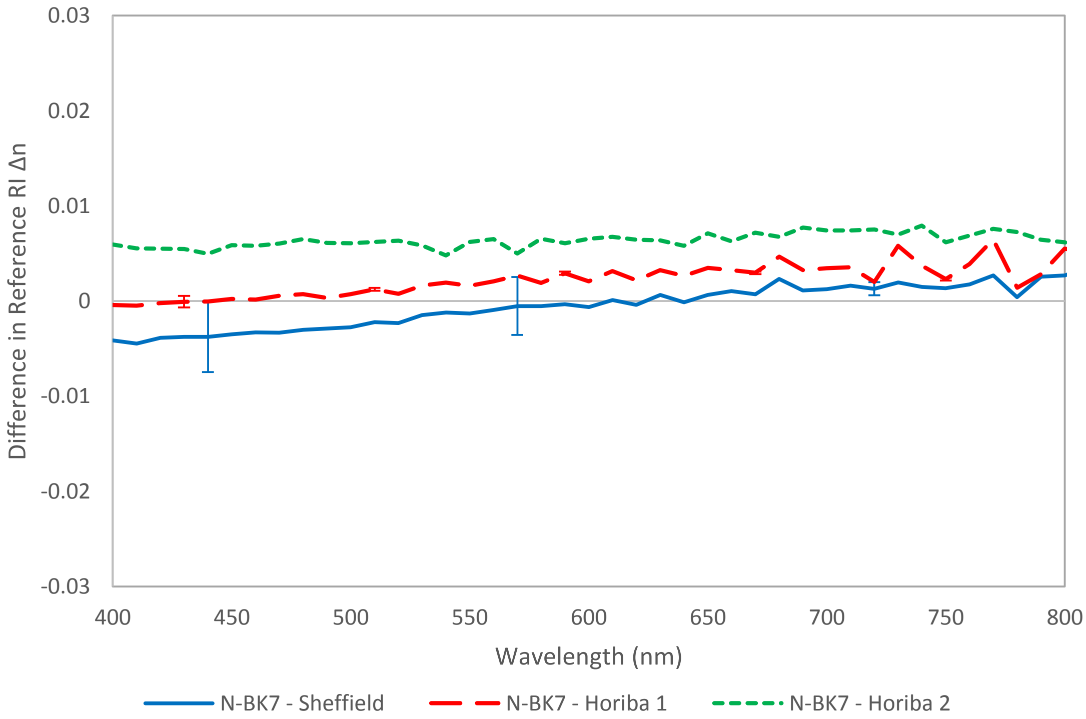

Figure 43 Error in measured RI as a function of wavelength for N-BK7 using Sheffield, Horiba 1 and 2 ellipsometers

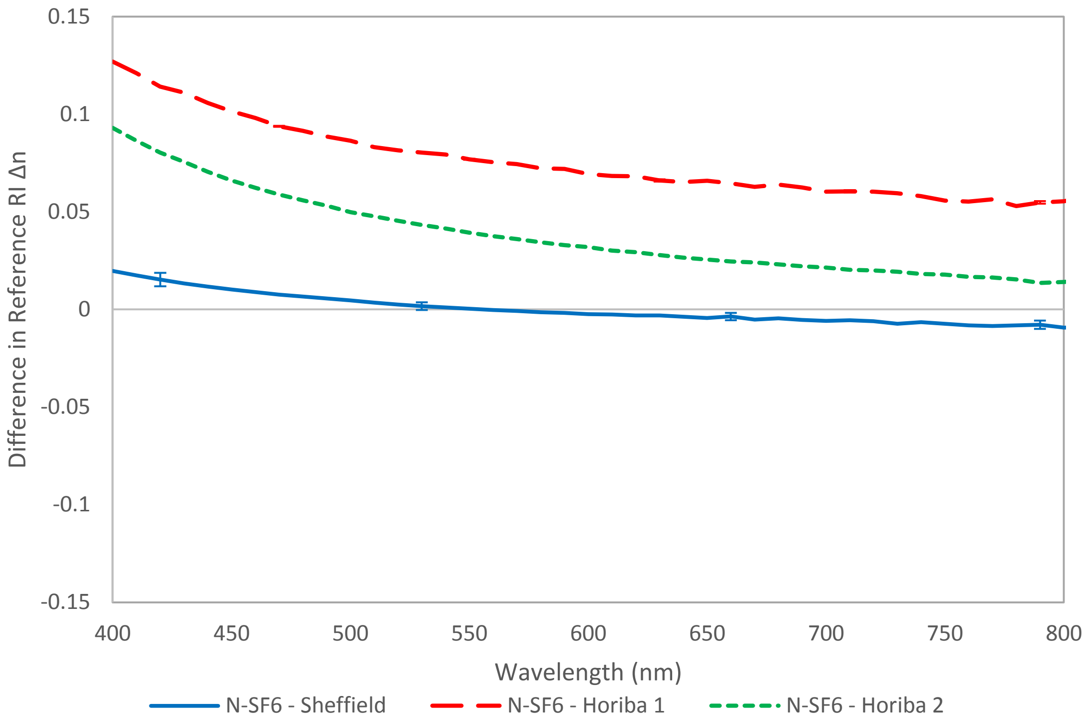

Figure 44 Error in measured RI as a function of wavelength using N-SF6 using Sheffield, Horiba 1 and 2 ellipsometers

Horiba 1 and Horiba 2 in Figure 42, Figure 43, and Figure 44 show a continuous offset for all of the samples. This demonstrates that a higher accuracy cannot be obtained using the recalibrated Sheffield ellipsometer. SF6 scans for all samples demonstrate an identical RI offset from the reference data for the 400 to 550nm range. This suggests that the SF6 samples most likely vary from the reference data in the range of 550 to 400nm. Considering the data from sample SF6 and the lack of rise in accuracy with other ellipsometers, the ellipsometer used for all RI measurements is considered to be accurate with an error of RI of ±0.015 over the 400-800nm range.

Another point to be considered is the common use of silicon wafers with varied oxide layer thickness for modelling of the data for calibration of ellipsometers. This technique can easily result in human errors rather than direct measurement techniques. In conclusion ellipsometers should be calibrated using single layer substrates with direct index conversion. If this had been performed on the ellipsometer the error of the equipment would be smaller.

4.2.2.3 Resin Ellipsometry

Figure 45, Figure 46 and Figure 47 show the average measured RI of resin samples produced by ellipsometry over the wavelengths 400-800 nm. Figure 45 shows 828 cured with a range of hardeners whilst Figure 46 and Figure 47 show the RI of DDS and DDM with a range of resins.

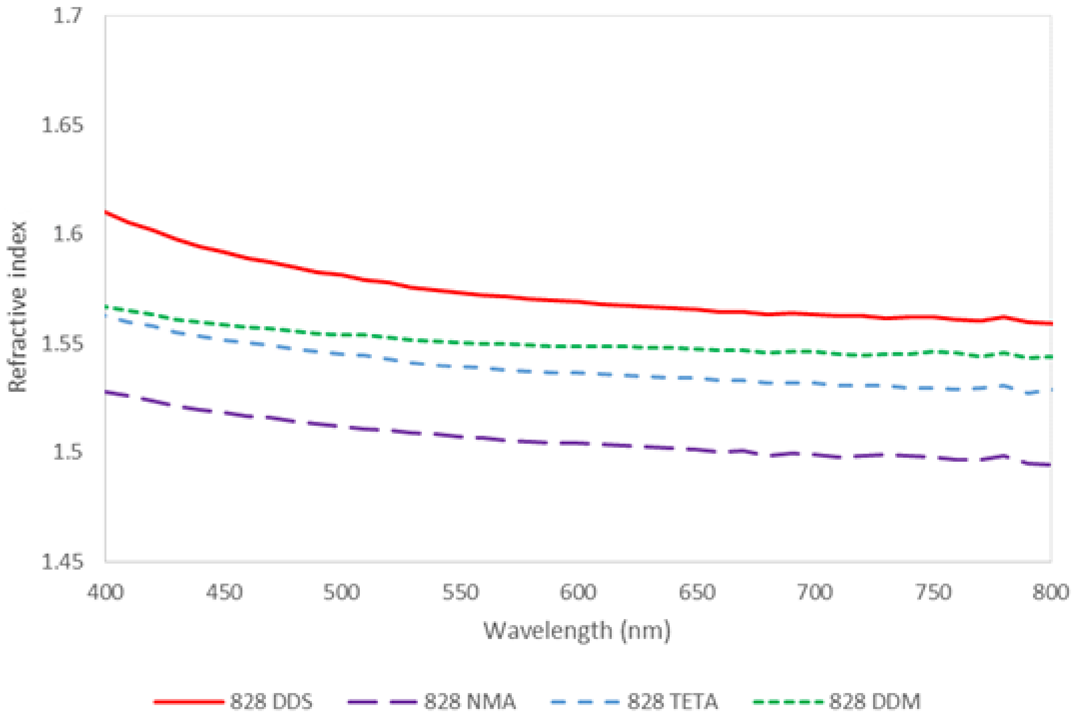

Figure 45 Refractive index of 828 cured with DDS, DDM, NMA and TETA (n is not a unit, so I would suggest you remove it from the Y-axis title of this figure and the following figures)

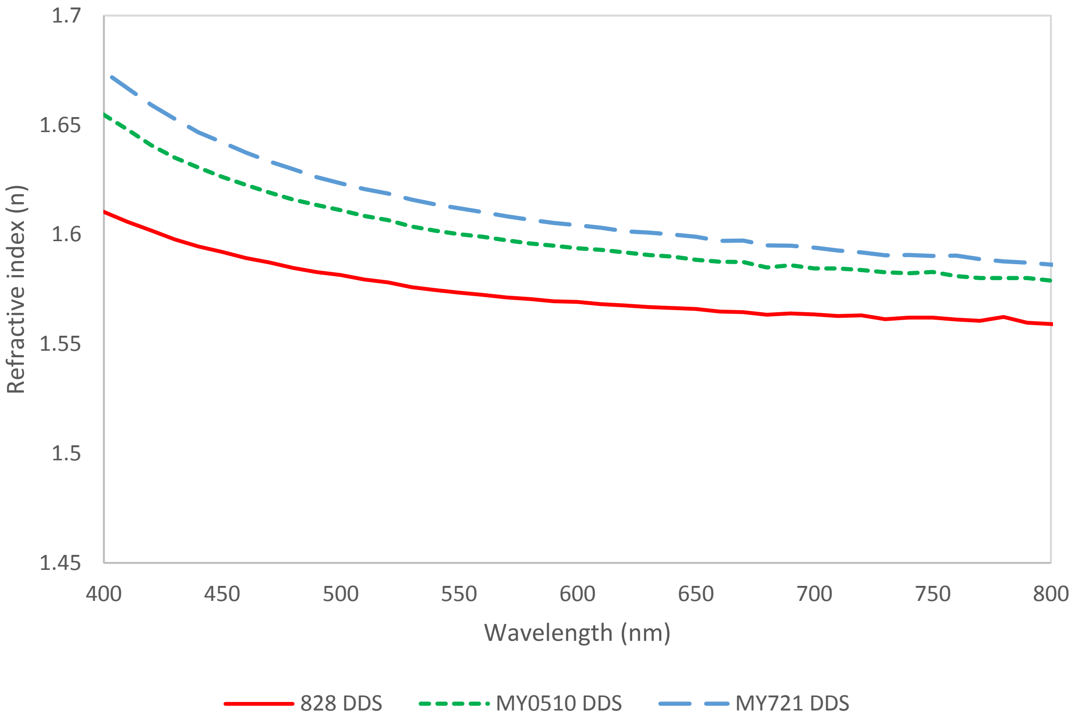

Figure 46 Refractive index of DDS curing agent with 828, MY0510 and MY721

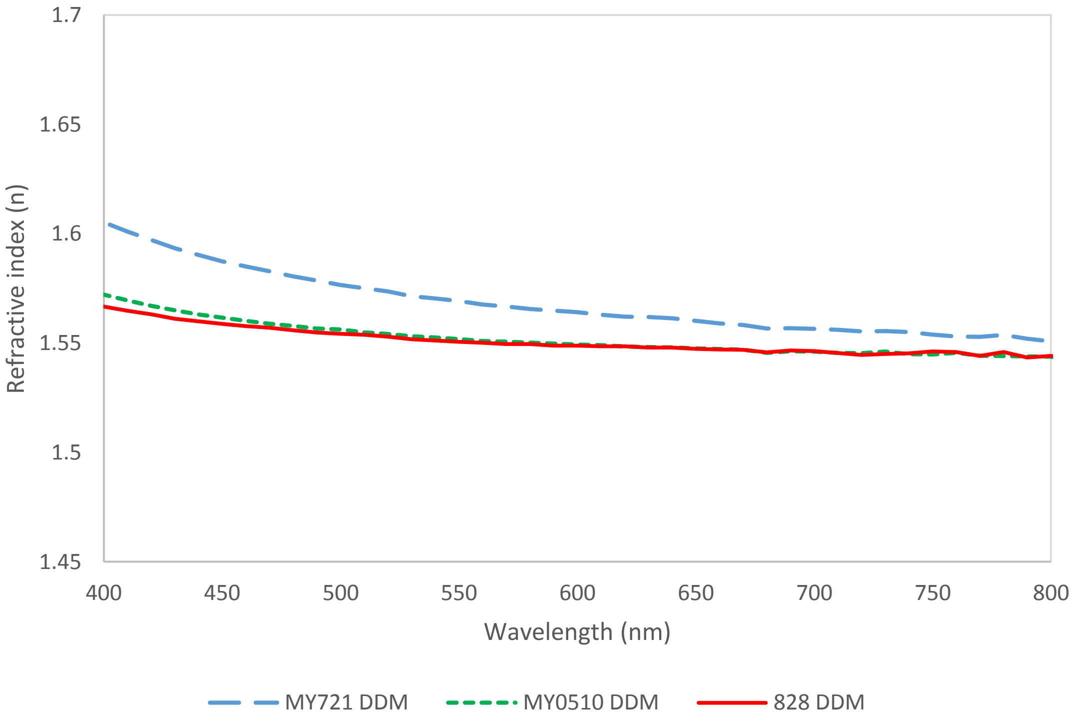

Figure 47 Refractive index of DDM curing agent with 828, MY0510 and MY721

4.2.2.4 Resin density

Resin densities were measured using a pycnometer; results are shown in Table 23

Table 23 Resin densities (g/cm^3)

Resin / Hardener	828	MY0510	MY721
DDS	1.2412	1.3264	1.2737
DDM	1.1993	1.2695	1.2366
TETA	1.1999	-	-
NMA, BDMA	1.2412	-	-

4.2.2.5 Epoxy production for RI measurements

Producing the ideal epoxy sample for RI measurements required a few techniques to be trialled. Initially samples were cast onto PFTE fabric coated plates, however the surface finish was unsatisfactory for optical analysis and multiple grinding and polishing steps led to no success. Therefore, samples were then cast between two mould-released polished steel plates which also produced poor results. Samples were subsequently cast between two glass sheets using a silicone inner mould which, due to stickiness between the mould and glass, would not release. The same technique was then modified adding a layer of cellulose acetate sheet in-between the mould and glass panes. This produced samples which could be de-moulded with clear surfaces ideal for optical analysis, however, due to the low temperature stability of laser acetate this technique could not be used for all of the resin systems. Finally successful samples were cured on glass panes treated using Henkel Frekote® 770-NC semi-permanent mould release as stated in Section 3.4.1 .

However, the use of a release agent which is on the scanned side for optical measurements may lead the addition of the release agent into the resin resulting in inaccuracies in the measurement. This being said, no other methods are available to the author’s knowledge which would produce >1 mm samples of epoxy with an optically flat surface.

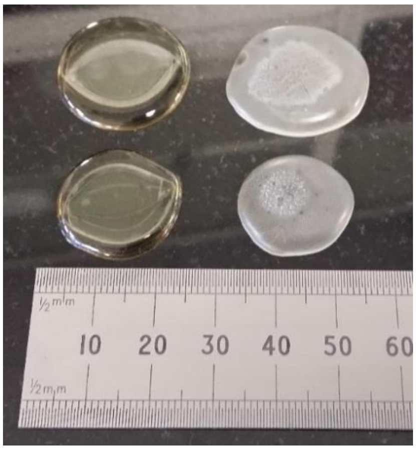

Figure 48 828 cured with DDS (left) and TETA (right), demonstrating amine blushing

All the samples produced were a range of transparent amber colours apart from 828 cured with TETA which had an oily/whitened finish as shown in Figure 48. This is not too surprising, because as stated in Section 1.3.1.1.1 low molecular weight amines like TETA can blush. Samples of 828 with TETA were left in a lab to cure with a high air turn over, preventing any additions of CO_2 and moisture. However, the blooming only occurred on the top surface of the "splat". As the measurement was taken from the bottom surface, it is assumed that no additions of high ammonium carbonate would have contributed to the RI measurement.

4.2.2.6 Discussion

Figure 45 shows the refractive indices of 828 cured with DDS, DDM, TETA and NMA. The systems give an increasing refractive index of DDS>DDM>TETA>NMA. This is expected due to the hardeners respective structures shown in Figure 22; when these are related to the Lorentz-Lorenz given in equation (22) the increase in polarisability and molecular density will produce a higher RI. DDS and DDM have very similar structures only differing by the presence of an SO_2 and CH_3 respectively between the aromatic rings as shown in Figure 22. This would presume that DDS's SO_2 should have a higher polarisability due to lone pair electrons on the oxygens and consequently would have a higher RI than DDM's CH_3. The mix ratio of DDM to DDS in 828 blends will have more DDM on a molecular level per epoxy; this difference is due to DDM having a smaller molecular weight and identical mix ratio by weight. However, between the two structures the substitution of SO_2 in DDS for CH_3 in DDM will produce a higher RI due to the higher polarisability of SO_2 due to larger atoms and consequential free electrons. As expected

828 cured with TETA has a lower level of polarisable ions and consequently lower RI than DDS and DDM. However TETA, possessing larger nitrogen content than NMA with BDMA, has a higher RI.

DDS cured resins (Figure 46), and to some degree DDM cured resins (Figure 47), show an increase in RI with epoxy functionality i.e. MY721>MY0510>828. Some of this is expected as the reaction of each epoxy ring results in a hydroxyl group, which is polar. Another factor that would explain the trend is the epoxy excess factors shown in Table 13 of 1.13, 1.72 and 2.09 for 828, MY0510 and MY721 with DDS respectively. This greater epoxy excess leads to a higher level of epoxy groups remaining within the structure, which in the case of MY721 enables higher RI. It is also apparent from MY721 structure that it would possess the highest RI value due to it having two extra nitrogen atoms and benzene rings, both polarisable species, than MY0510 and 828. The structure of MY0510 would suggest a lower refractive index than the other two systems due to a single benzene ring, however, this single ring reduces the steric hindrance producing a higher molecular density and actual density as shown in Table 23 enabling the system to fit between MY721 and 828 when cured with DDS. However, even with density trend of MY0510>MY721>828 for both DDS and DDM the higher density of MY0510 and higher epoxy excess than that of 828, it is seen that the RI values of 828 and MY0510 are similar. This shows that the DDM is playing a stronger role in these systems, balancing out the small size of the MY0510 molecule and higher epoxy excess factor.

Results were as expected with higher quantities of polarisable groups and higher densities producing high RI values. Curing agents follow the RI increase trend of DDS>DDM>TETA>NMA in 828 resin systems. The maximum RI was MY721/DDS which has a RI of 1.61 at 590 nm. This will act as a baseline which glasses must exceed in order to be considered suitable for FEWS cure monitoring.

4.2.2.7 Glass Ellipsometry

Figure 49 shows the combined plot of glasses and a shaded area that encompasses the range of refractive indices for the epoxy resins, taken as the highest measured epoxy RI, MY721 cured with DDS as shown in Figure 46. This gives a baseline for minimum RI of the sensing glass fibre. Samples of reinforcing glasses: Advantex and R-glass were also measured as a comparison with the glasses produced.

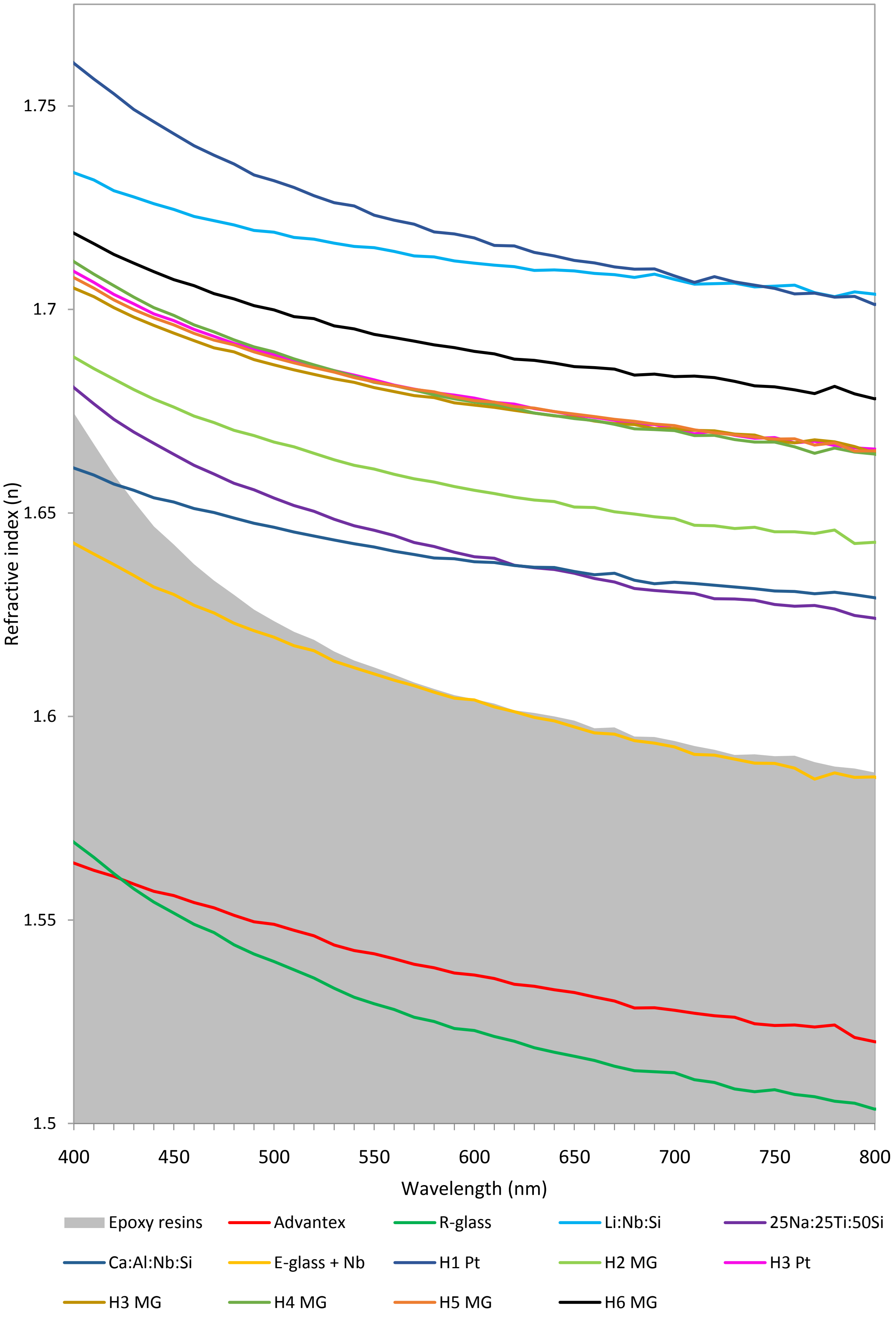

Figure 49 Ellipsometry RI values of glasses with the epoxy resin upper limit.

4.2.2.8 Glass densities and RI

Glass densities were measured using Archimedes' water submergence principal. The density results and RI values are tabulated in Table. 24.

Table. 24. Measured densities and RI at 590 nm of the glasses

Composition	**Density (g/cm^3)**	**RI (590 nm) (±0.015)**
Advantex (E-glass)	2.661	1.52
R-glass	2.554	1.54
Li:Nb:Si	3.217	1.64
Na:Ti:Si	2.792	1.69
Ca:Al:Nb:Si	3.112	1.64
E-glass -5%Al + 5%Nb	2.858	1.60
H1 Pt	3.779	1.72
H2 MG	3.535	1.66
H3 Pt	3.700	1.68
H3 ME	3.596	1.68
H4 MG	3.604	1.68
H5 MG	3.576	1.68
H6 MG	3.642	1.69

4.2.2.9 Glass RI Discussion

There is an argument that the refractive index measured for these glasses in the bulk is not representative of the final drawn fibre. The higher cooling rates for fibres produce compressive forces on the surface which consequently increase the density, resulting in an increase in the final RI values. However, inducing the same cooling rates on the glass samples would be impractical and the relatively unstressed bulk samples give a conservative value when compared to the fiberized glass.

Advantex and R-glass have RI values which correlate with [32, 33], which correlate to their low densities, high silica content and lack of heavy transition metals. This prevents these compositions from FEWS cure monitoring of high performance epoxy resin through the entire cure. The addition of 5%mol Nb_2O_5 and subtraction of 5% mol Al_2O_3 in E-glass gave a significant RI and density increase when compared to Advantex. Other calcium aluminosilicates (Ca:Al:Nb:Si) produced a higher RI than that of the niobium modified E-glass at 1.64. This is to be expected due to Ca:Al:Nb:Si possessing a very high level of calcium (>50% mol) and lower silica driving up the RI.

The Na:Ti:Si produced a RI of 1.64 which is lower than the reported value of 1.678 [105]; the reference RI was produced in Pt crucible consequently giving a lower value due to additions of Al_2O_3 and SiO_2 compared to glass produced in a mullite crucible. Li:Nb:Si produced a high RI, as expected due to lithium producing the highest contribution to RI of the alkali ions (as stated in section 2.3.8.1), acting in combination with a high niobium content.

Samples of H1 Pt have the highest RI of all the H-glass family. H1 Pt has a roughly similar composition to H4 and H6 but, lower silica and almost double the Nb_2O_5 level. This corresponds to a higher level of polarisable atoms and resulting high RI. H3 Pt and H3 MG have similar RI's with a slight reduction when melted in mullite. As previously stated in Section 4.1.2, XRF of H3 compositions demonstrate a rise in levels of SiO_2, Al_2O_3 and Fe_2O_3 when melted in mullite. The increases in these elements, and resulting percentage decrease in remaining batch, reduces the overall levels of highly polarisable elements and consequently produces a lower RI and lower density. However, this trend is within the error of ±0.015 and consequently cannot be confirmed.

H2 MG produced the lowest RI of 1.66 as expected due to the lowest permittivity of all of the H glasses as given in [96] and also being melted in mullite where the SiO_2 and Al_2O_3 additions will have further decrease the expected value. Purely looking at H2 MG with lower silica and higher alkali earth ions compared to H3 to H6 it would be expected that a higher RI would be attained however, the lower density would explain a lower RI.

The value of H6 MG was expected to be in line with H4 and H5, with the larger density being expected to correspond to the higher RI. However, this increase cannot be fully confirmed due to the trend being within the region of error ±0.015.

In conclusion, reinforcing glasses are unsuitable for FEWS monitoring throughout the entire cure of aerospace grade epoxy resins. The addition of 5%mol Nb_2O_5 and subtraction of 5%mol Al_2O_3 from boron free E-glass produced a glass on the border line of RI, rendering it unsuitable for FEWS cure monitoring of epoxy resins. All of the other glasses studied show the potential for FEWS monitoring of aerospace grade epoxy resins as shown in Figure 49.

4.3 Thermal Analysis of glasses

To investigate the possibility of producing fibres from the glass compositions and to determine the glass stability, fibre drawing and liquidus temperatures; DTA, viscosity and liquidus measurements were performed respectively. Figure 50 and Figure 51 show DTA traces for non-H glass and H-glass compositions respectively. The plots show the initial endothermic dip, which was used for T_g measurements. The following exothermic peak demonstrates crystallisation of the glasses. Any further endothermic troughs show melting of the glass.

Ideally glass samples should be cycled twice within the DTA to remove the thermal history and produce consistent thermal history for all samples, giving more comparable data. However, due to the samples tendency to crystallise during the initial heating cycle the crystallised samples during the second cycle prevents acquisition of accurate T_g values. Consequently, samples were heated in an atmosphere of air from room temperature to 1200 °C at 10 °C/min, in a single run, accepting that this is not optimum.

4.3.1 Differential Thermal Analysis (DTA)

DTA scans of the transparent glasses are shown in Figure 50 and Figure 51. DTA graphs show a glass transition T_g which were determined using the onset into the endothermic glass transition dip. This is then followed by a crystallisation peak T_x calculated as the maximum point of the exothermic peak. Perkin and Elmer Pyris software was used for the T_g and T_x locations and are labelled in Figure 50 and Figure 51.

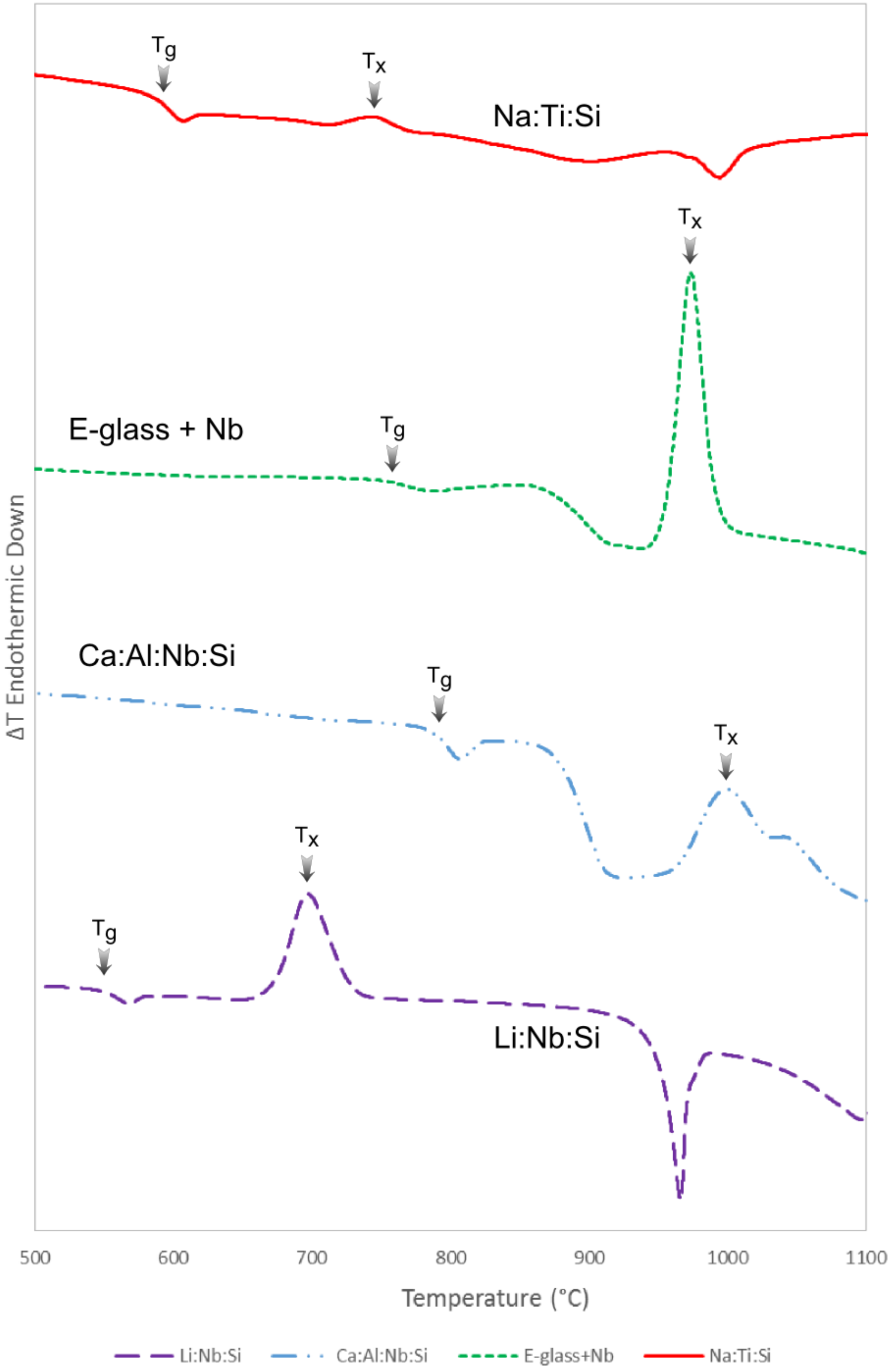

Figure 50 DTA results for Non-H-glass glasses

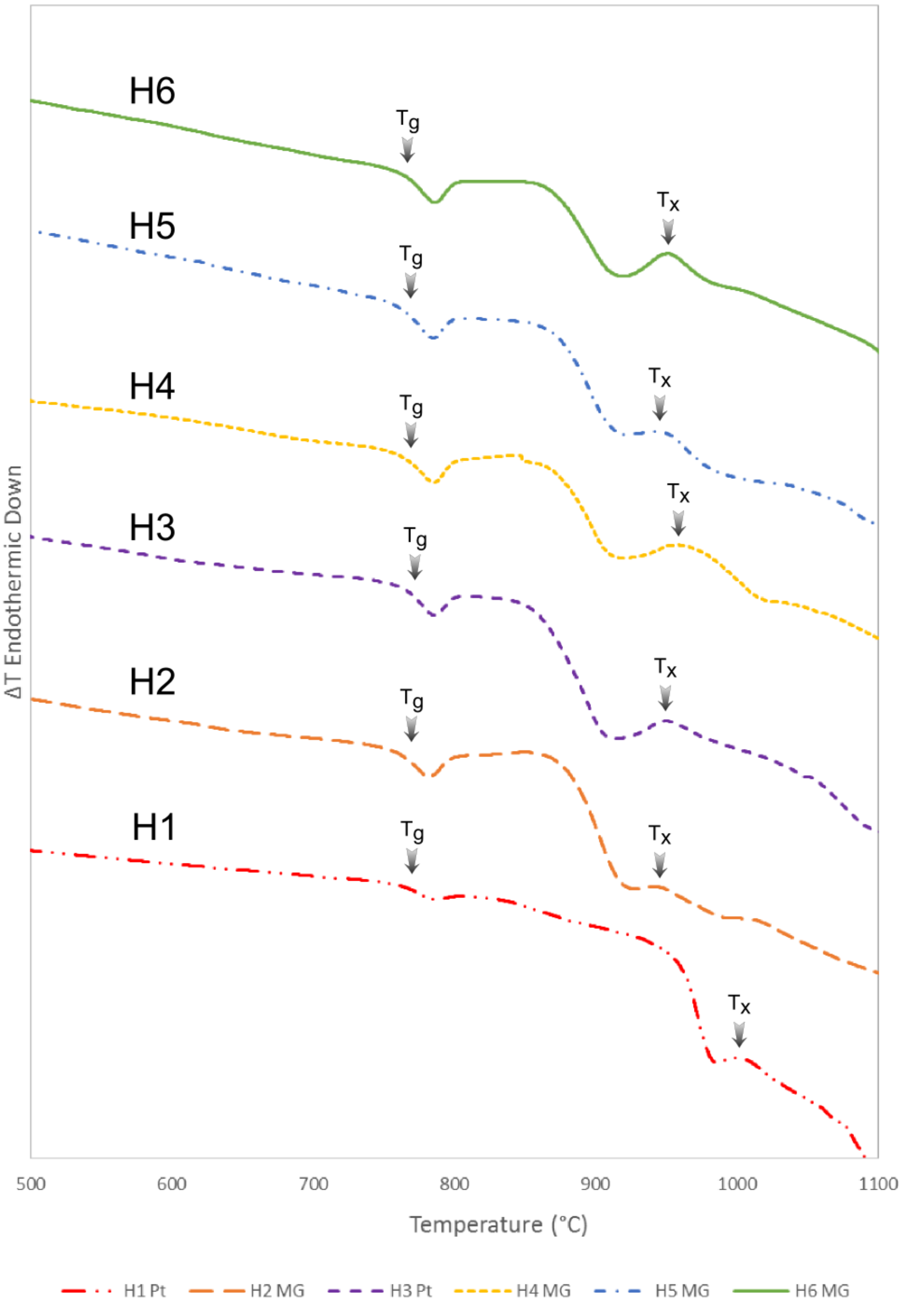

Figure 51 DTA for H-glass type glasses

4.3.2 Viscometer results

Ideally, viscosity data would have been obtained for all of the glasses however, due to machine down-time it was not possible to obtain data for all of the glasses. The two glasses which were measured, H1 Pt and H3 Pt are shown in Figure 52 and Figure 53 respectively. Figure 52 and Figure 53 show the expected increase in viscosity as the melt was cooled in temperature from 1450 °C to 1000 °C. The software converted spindle torque, firstly into Poise and then Log_{10} Poise, which was plotted against sample temperature.

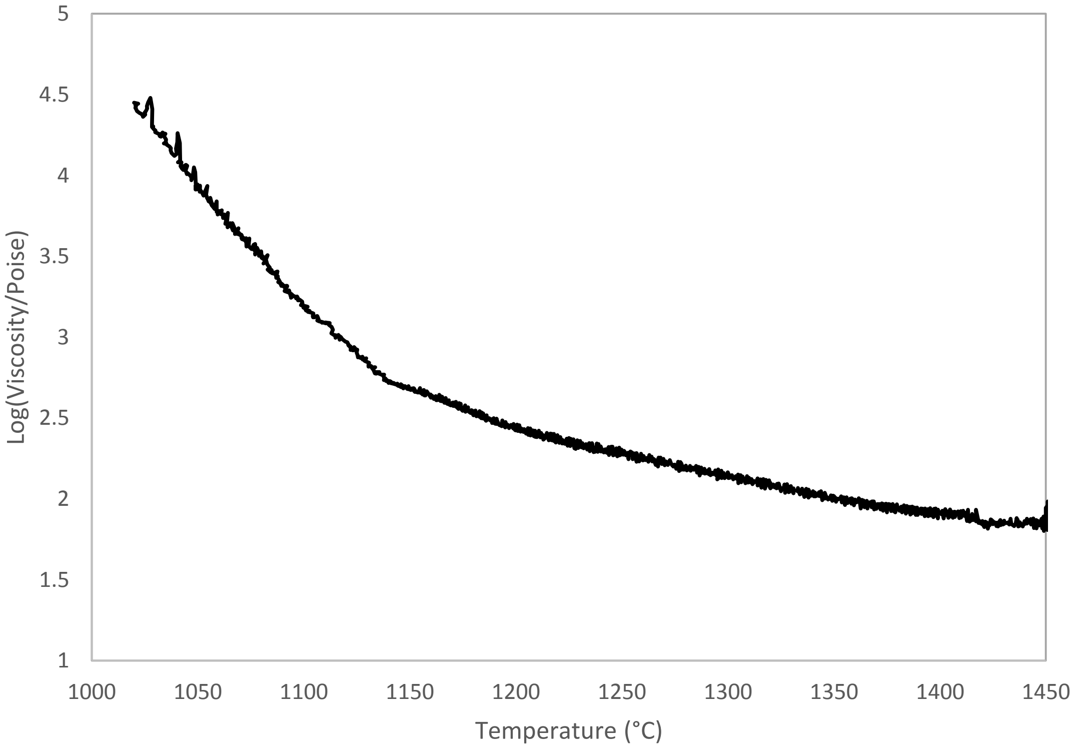

Figure 52 Viscosity trace for H1 Pt glass

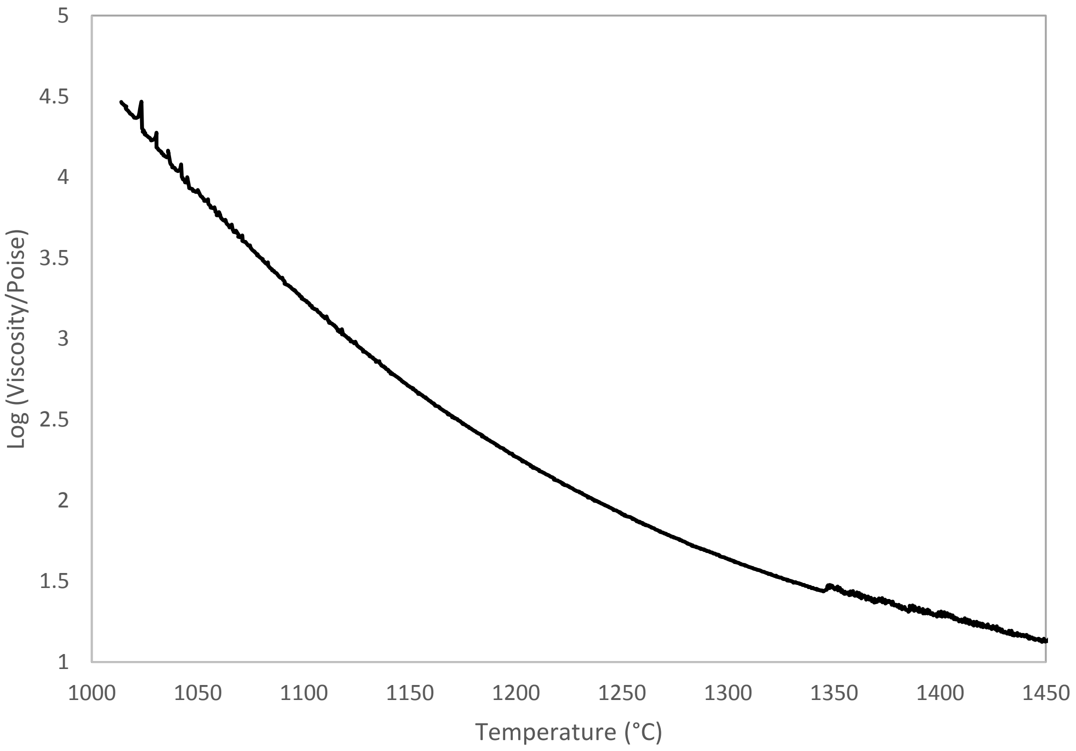

Figure 53 Viscosity trace for H3 Pt glass

4.3.3 Glass thermal analysis

A summary of thermal data is given in Table 25. The glass transition temperatures and crystallisation temperatures were calculated from DTA traces using the Pyris software. Liquidus measurements were taken using temperature extrapolation and accurate crystallisation point measurements, whilst, $Log_{10}(\eta/Poise)=3$ fibre forming points were extracted from the raw viscosity data. The data for these experiments are plotted in Figure 50 - 54 and given in Table 25. A $Log_{10}(\eta/Poise)=3$ fibre forming temperature was taken due to the expectation that a higher viscosity is required for up drawing of fibres than convention fibre production where a $Log_{10}(\eta/Poise)=2.5$ would be used.

Table 25. Results from DTA data for DTA $\Delta T = T_x - T_g$ and liquidus and $Log_{10}(\eta/Poise)=3$ fibre forming from viscometry in poise

	T_g (°C)	**T_x (°C)**	**Tx-Tg (°C)**	**T_L (°C) (±5°C)**	**$T(Log_{10}(\eta/Poise)=3)$ (°C) (±5°C)**	**ΔT**
Li:Nb:Si	547	694	148	1113	-	-
Na:Ti:Si	588	814	225	963	-	-
Ca:Al:Nb:Si	784	993	209	1274	-	-
E-glass -5%Al + 5%Nb	743	965	222	Attempted	-	-
H1 Pt	761	1003	242	1176	1102	-74
H2 GM	761	945	184	-	-	-
H3 Pt	766	951	185	1069	1108	39
H4 GM	763	963	199	-	-	-
H5 GM	763	947	184	-	-	-
H6 GM	765	952	187	-	-	-

Both of the alkali containing systems Li:Nb:Si and Na:Ti:Si show low glass transitions of approximately 546 °C and 588 °C respectively, whereas the alkali free glasses characteristically demonstrate a high T_g >743°C. This is expected due to alkali elements breaking up the Si-O structure enabling glass formation at lower temperatures. All of the glasses show a larger separation between T_x and T_g indicating the formation of stable glasses.

For liquidus experiments, 24 hours was selected as a conservative value which the melt could be held at temperature. As previously stated in Section 2.3.1 the subtraction of the liquidus temperature from the fibre forming point gives a representation of the fibre formability known as ΔT. The larger the ΔT values the more stable the melt is for fiberisation. As stated in section 2.3.1 a composition with a ΔT >50 °C is capable of fibre forming.

The T(log(η/poise)=3) fibre forming temperature (log3 temperature) for H1 Pt was 1102 °C (±5 °C) and the liquidus temperature was 1176 °C (±5 °C). This gave a ΔT of -74 °C demonstrating the instability of H1-glass for fibre drawing.

Li:Nb:Si, Na:Ti:Si and Ca:Al:Nb:Si were all successfully examined for liquidus temperatures however, the lack of viscosity data prevents any statement on the suitability for fibre drawing. E-glass + Nb was attempted over a range of temperatures however, the furnace limit was reached at 1450°C and a stable temperature could not be maintained. Consequently, no value was obtained for E-glass + Nb. However, due to the fibre drawing furnace limit of 1200 °C, E-glass + Nb was not investigated any further.

H3 Pt produced a log3 temperature of 1108°C and a liquidus temperature of 1069°C producing a separation of 39°C which is lower than the desired separation of 50°C. Reference [96] gave a liquidus and T(log(η/poise)=2.5) (log2.5 temperature) for H3 Pt of 1054°C and 1154°C respectively measured in Pt crucibles. The measured log2.5 temperature was 1160°C which is slightly higher than expected which was most likely due to the potential additions of Al_2O_3, Fe_2O_3 and SiO_2 from the alumina crucible causing a viscosity decrease. The liquidus temperature increase suggests that any additions from the mullite such as Al_2O_3, Fe_2O_3 and SiO_2 may have also increased the melt's susceptibility to crystallisation, resulting in a liquidus increase. This suggests that H3 Pt composition would be difficult to draw from a mullite crucible due to a narrowing of the fibre drawing window.

4.4 Fibre drawing

4.4.1 Fibre winding jig development

One of the benefits of glass fibre down-drawing is a large temperature drop beyond the fibre bushing, whereas up drawing requires a controlled state and cooling regime [34]. Initial trials for fibre up drawing, demonstrated that the furnace hot zone was too large, such that the fibre fell back under its own weight due to the glasses low viscosity in the long hot zone. This was initially combated by increasing the height of the plinth using more furnace bricks, taking it further out of the hot zone. This approach was problematic because it was hard to get the melt temperature up to a suitable level for drawing, resulting in a limitation to the maximum fibre drawing temperature. It also gave no flexibility for changing over to differing glass types. As a result, an 8 mm copper pipe was bent around a preform forming a cooling coil. The coil was connected to a submerged pump in a cooled water tank previously shown in Figure 28. The cooling coil produced a sharp drop in temperature allowing the viscosity of the glass to increase rapidly, facilitating stable fibre drawing.

The next issue involved the correct coil height. This was problematic due to the varying level of the glass in the crucible as the fibre was drawn, necessitating various coil heights above the melt. Measuring the glass melt temperature during fibre drawing was impossible due to the obstruction caused by the fibre during drawing. So furnace profiles were taken post fibre drawing as described in Section 3.9.4.

4.4.2 Furnace temperature profiling

The furnace was profiled with a mullite crucible containing Advantex™ glass to simulate the thermal mass of a melt. Measurements were performed from just above the melt and every 3 cm afterwards as shown in Section 3.9.4. The coil was inserted at a different level each time and given 45 minutes to stabilise the temperature before temperature profiling. The temperature was logged over a minute and averaged for each thermocouple producing a range of furnace profiles given in Figure 54.

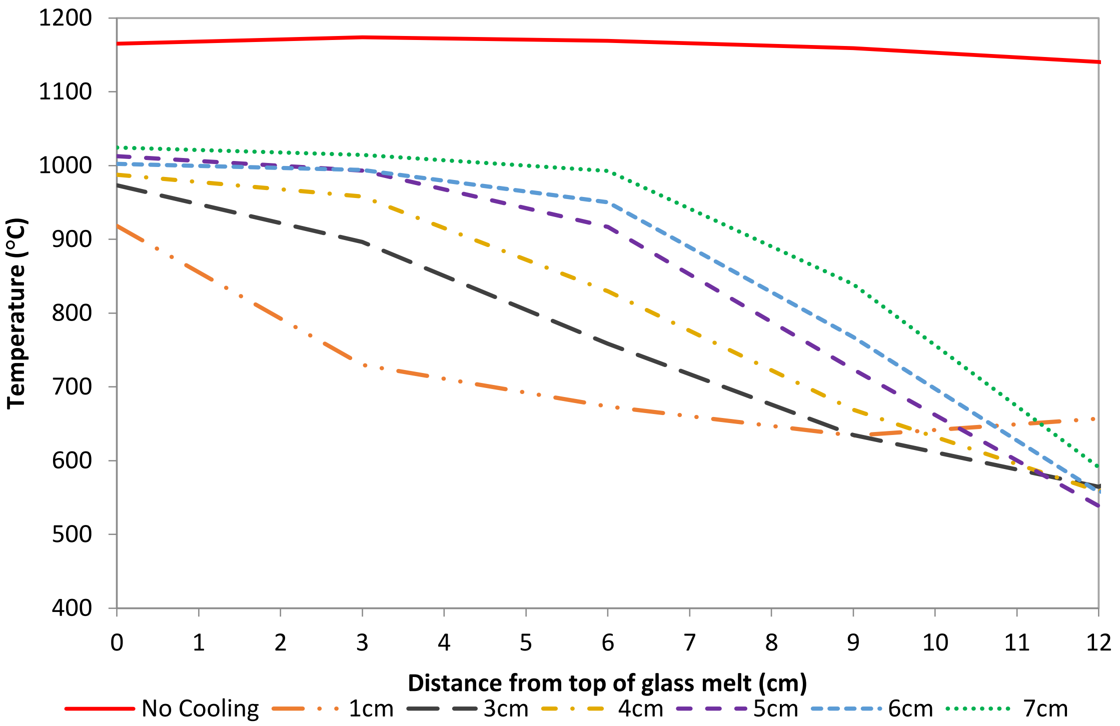

Figure 54 Temperature profiles of the furnace with the cooling coil at different heights above the melt

Figure 54 shows the initial wide hot zone when no cooling coil is used. As the coil is placed at different heights the initial temperature drops as the coil is placed closer to the melt until the coil is 1 cm away with at which point the temperature rises again at 12 cm beyond the melt, this being beyond the 10 cm long coil.

For fibre drawing to be achieved with the produced jig, the fibre drawing temperature would have to be below 1015 °C (±10 °C) using the maximum coil height of 7 cm.

4.5 Fibre drawing

The only glass with a liquidus value below 1015°C was Na:Ti:Si (T_L 963°C) and thus due to the limited access to viscosity measuring equipment it was decided to trial the glass. The cooling coil was left to thermally homogenise for 45 minutes with the coil held at 7 cm above the crucible. The melt remained at too low a viscosity, preventing fibre formation. The coil height was subsequently decreased in height using 10 mm steps. At 6 cm from the melt, 50 cm fibres with a large diameter variability were produced. Reducing the coil further caused crystallisation of the melt. It was concluded that the temperature drop beyond the melt was not sharp enough to form stable fibres. To try and overcome this, the coil was placed 40 mm away from the glass melt and fibre drawing was attempted during the period of cooling down. This further increased the fibre length to 1 to 2 meters with large fibre diameter variation, however continuous lengths were not formed.

The remaining glasses all possess liquidus temperatures >1015 °C. The only remaining method was to place the coil above the melt using the cooling down period to draw fibres. Li:Nb:Si possessed the next highest liquidus temperature. However, due to unsuccessful fibre drawing by hand it was decided not to trial Li:Nb:Si. The next highest liquidus point was H3 Pt at 1069°C with a Log3 temperature of 1108 °C. H3 fibres were drawn using the parameters given in Table 26.

Table 26 Fibre drawing parameters and resulting fibre properties

Distance from top of crucible (mm)	**Thermocouple height from bottom of crucible (mm)**	**Start temperature of fibre draw (°C) (±10°C)**	**Drum speed (m/sec)**	**Average fibre diameter (µm)**	**STDev fibre diameter (µm)**
10	40	-	6.60	261	15
30	40	1098	7.83	124	46
40	47	1109	7.83	55	18

For the first batch of H3 Pt fibres no fibre temperature data was recorded but, for the second and third batches fibres were drawn at log(η/Poise)=3.1 and 3 followed by a viscosity increase as the temperature cooled. This shows a higher viscosity was required to up draw the fibres. This is most likely due to the up drawn fibre having to withstand its own weight as opposed to down drawn fibres which are allowed to fall under gravity and consequently can be drawn at lower viscosities.

After the successful drawing of H3 fibres given in the first row of Table 26 another 3 batches 300 g of H3 Pt were produced for further analysis and fibre drawing.

4.5.1 H3 Pt ultrasonic modulus measurements

The modulus of the glass was determined via ultrasonic measurements in order to determine if the sensing fibres could successfully be used as reinforcing fibres.

Table 27 Modulus measurements taken by ultrasonic methods for H3 Pt samples

Poisson's ratio	**Young's Modulus (GPa)**	**Shear modulus (GPa)**
0.28 (±0.01)	88.3 (±1.0)	34.6 (±0.1)

Modulus values of H3 glass are comparable to those of S-glass fibres at 86.9-91 GPa [31, 32]. H3-glass has lower levels of silica in comparison to S-glass which would result in a lower modulus; however, H3 contains niobium and aluminium increasing networking, resulting in an increased modulus. This should allow H3 fibres to be inserted into glass fibre composites for cure monitoring and potential through life monitoring with no impact on the mechanical performance.

Table. 24 demonstrates H3 Pt has a 39% larger density than Advantex, which would result in a significant increase in final composite mass for a given fibre fraction. For example in a typical Advantex prepreg with 50wt% fibre, if all the fibres were replaced by H3 fibres the total composite would have a total mass increase of 19.5%. This factor would prevent these glasses from being used as the only reinforcing fibre within a composite. However, co-mingling with other structural fibres could produce a composite with sensing capabilities with a minimal impact on the final weight of the composite.

4.5.2 H3 Pt production for fibre drawing

Three identical batches of 300g H3 were batched and melted using the procedure given in Section 3.2. However, two of the three batches resulted in phase separation as shown in Figure 55.

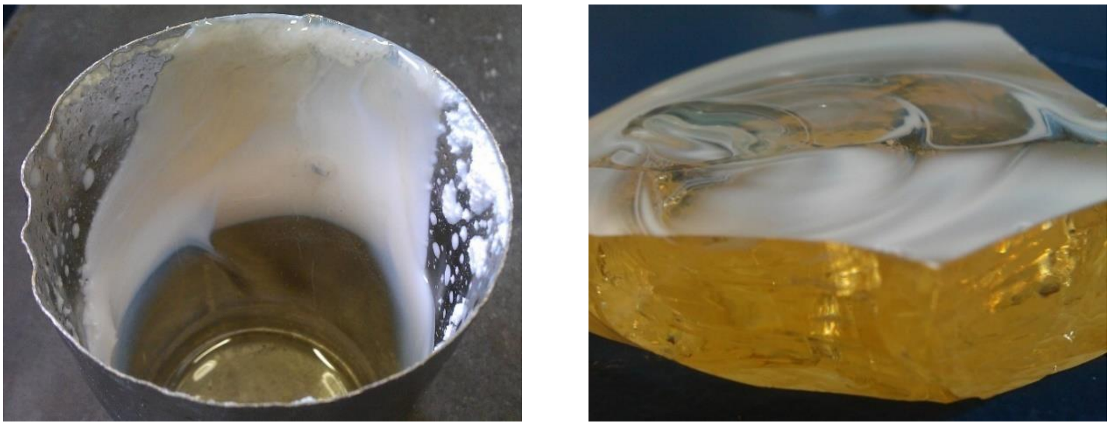

Figure 55 Phase separated H3 Pt glass

A solid white phase separated section was scanned using XRD. To remove the top surface the sample was melted in a Pt crucible. The white section was floated to the top and using a silica rod the top layer was skimmed off and air quenched. The resulting section was powdered according to Section 3.3.3. The XRD scans of the solid and powdered phase separated sections are given in Figure 56. This demonstrates that both of these phase separated portions are x-ray amorphous.

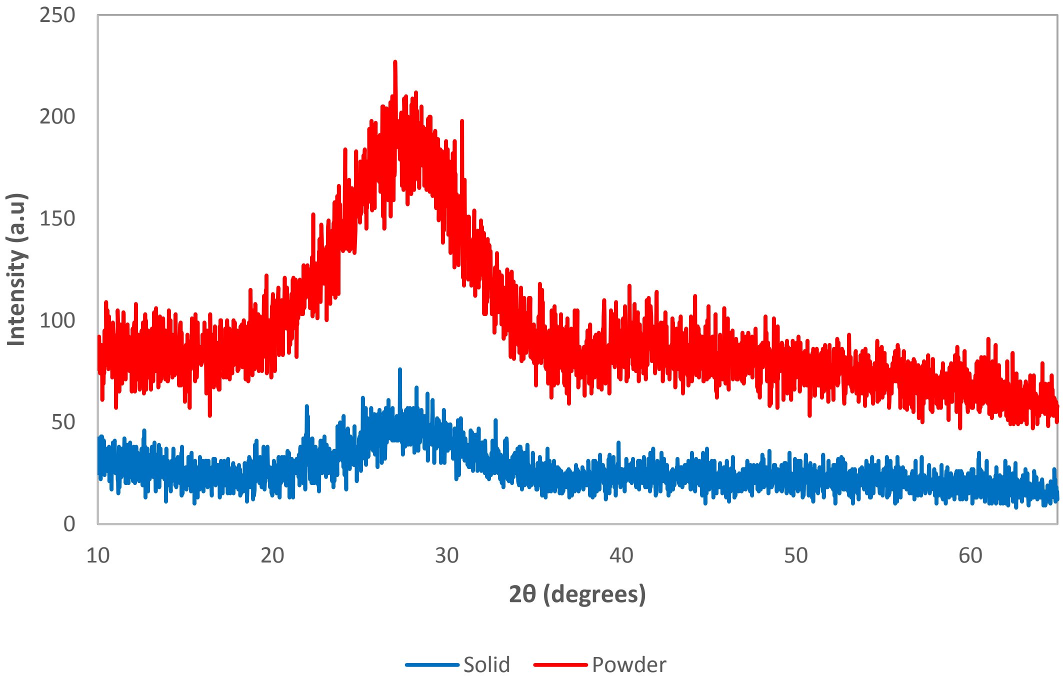

Figure 56 XRD scans of the white phase separated section from H3 glass samples

4.6 Near infra-red experiments

4.6.1 Bentham spectrometer setup

The Bentham fibre spectrometer was optimised to produce the most accurate noise free data. Diffraction grating selection involved balancing a few parameters to optimise the bandwidth and resulting signal level within the desirable sensing wavelength range. The lower line density gratings enabled further transmission into the IR. G306R1U25 grating with 600 grooves/mm produced an 800-2500 nm range, whilst G303R3U0 grating with 600 grooves/mm enabled 1500-5500nm range. The lower the line density of the grating the smaller the slit size and resulting intensity was required for the same bandwidth as shown in Figure 57. Figure 57 gives the bandwidth versus the slit size for the two aforementioned gratings taken from ref [122]. Due to poor signal intensity with 10nm bandwidth using H3 fibres with the 300 line grating, the 600 line grating was selected. This limits the NIR range available, however, it produces the best signal to noise ratio.

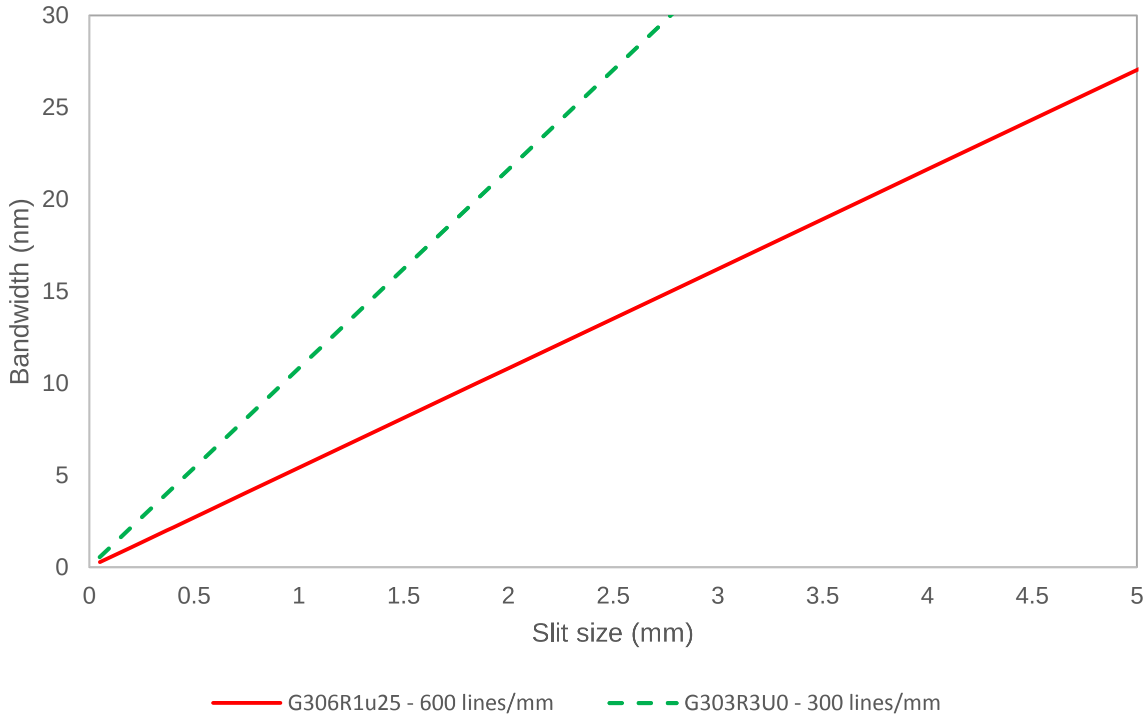

Figure 57 Bandwidth (nm) versus monochromator slit size (mm) for the 600 and 300 lines/mm diffraction gratings.

4.6.2 Detector setup

A PbS sensor was selected for the experiments due to the limited wavelength range of the InGaAs sensor supplied by Bentham optics which extended from 900 to1700 nm. PbS sensors can sense from 1000-3600 nm and were hence ideal for sensing in the NIR. Due to the expense of purchasing a PbS sensor it was decided to produce a PbS sensor, so a box was mounted with a fibre holder and the sensor was soldered into the configuration shown in Figure 58. An external power supply is required for the PbS sensor. A maximum value of 100V supply can be used with the P9217-03 sensor. The higher the supply voltage the greater the signal and signal to noise ratio. Due to limitations of the power supply and voltage stability, a 50V supply was used for all of the testing.

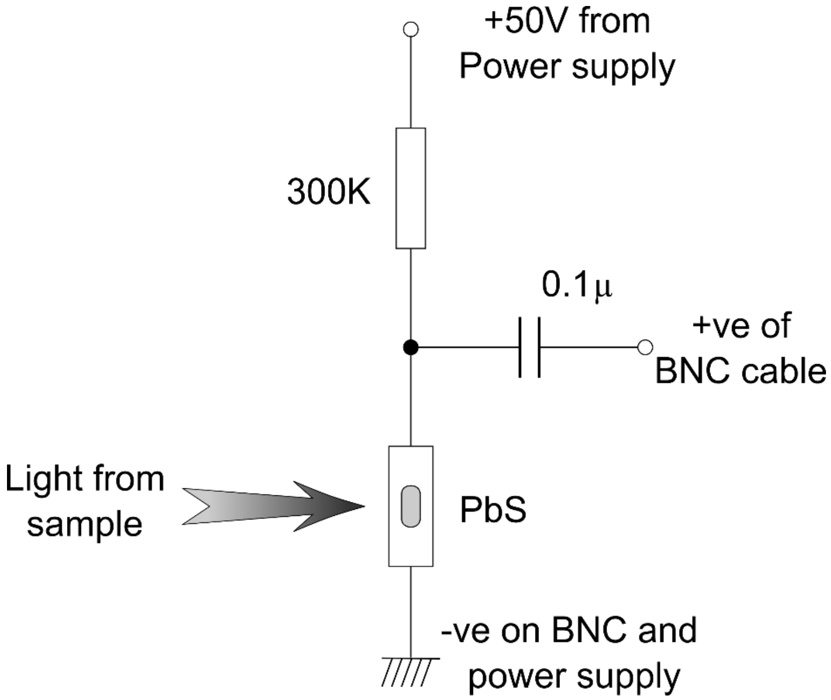

Figure 58 Wiring diagram of PbS sensor, the positive was sent to the Bentham's amplification units.

The resulting averaged scan from the G306R1u25e grating and PbS sensor when placed directly in front of the focusing lens after the monochromator produced the intensity curve shown in *Figure 59*.

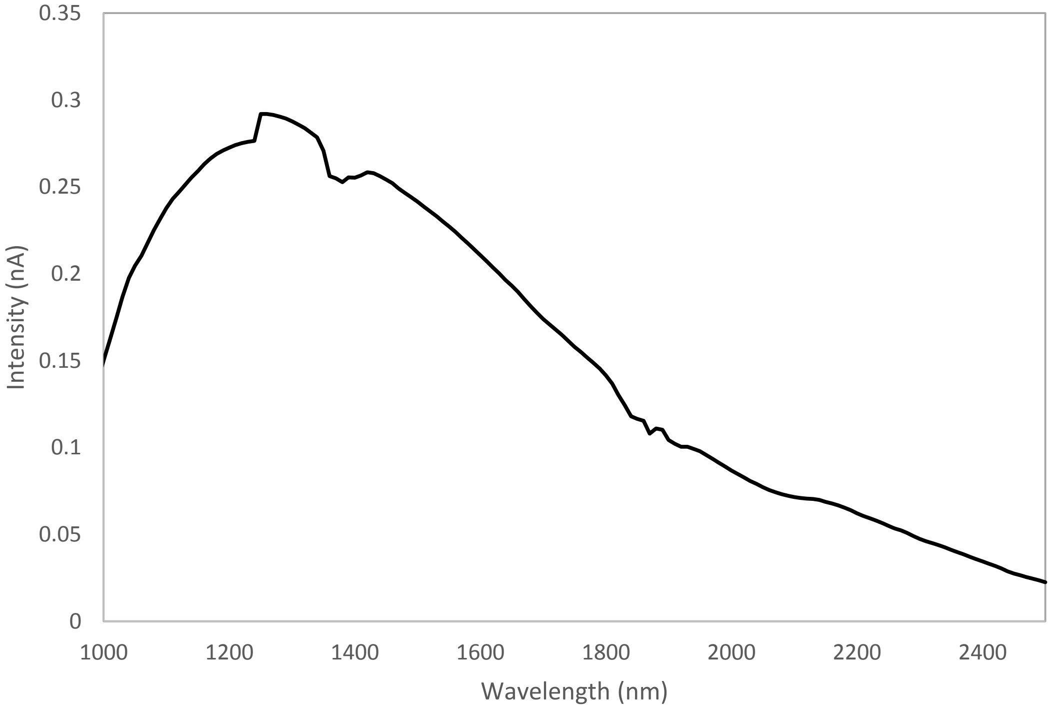

Figure 59 Intensity level of the light source and PbS sensor.

The features of Figure 59 are the result of the lamp, monochromator, diffraction grating, sensor sensitivity and launch optics. The initial slope from 1000 nm to 1200 nm is due to the PbS sensor sensitivity and the continued drop from 1200 nm to 2500 nm is due to the diminishing light intensity from the tungsten halogen light source. The peaks and troughs around 1260, 1370 and 1890 nm are artefacts of the detector which during processing are removed using the Beer-Lambert law.

4.6.3 Calibration - Neutral Density Filters

Neutral density filters (NDF) of 0.04, 0.1, 0.3, 0.5 and 1.0 were used to check the wavelength sensitivity over Bentham fibre spectrometer. Neutral density filters were not supplied with reference scans over the 1000-2500 nm region of interest. To test for uniformity over this region, they were scanned using the UV-Vis spectrometer, producing Figure 60.

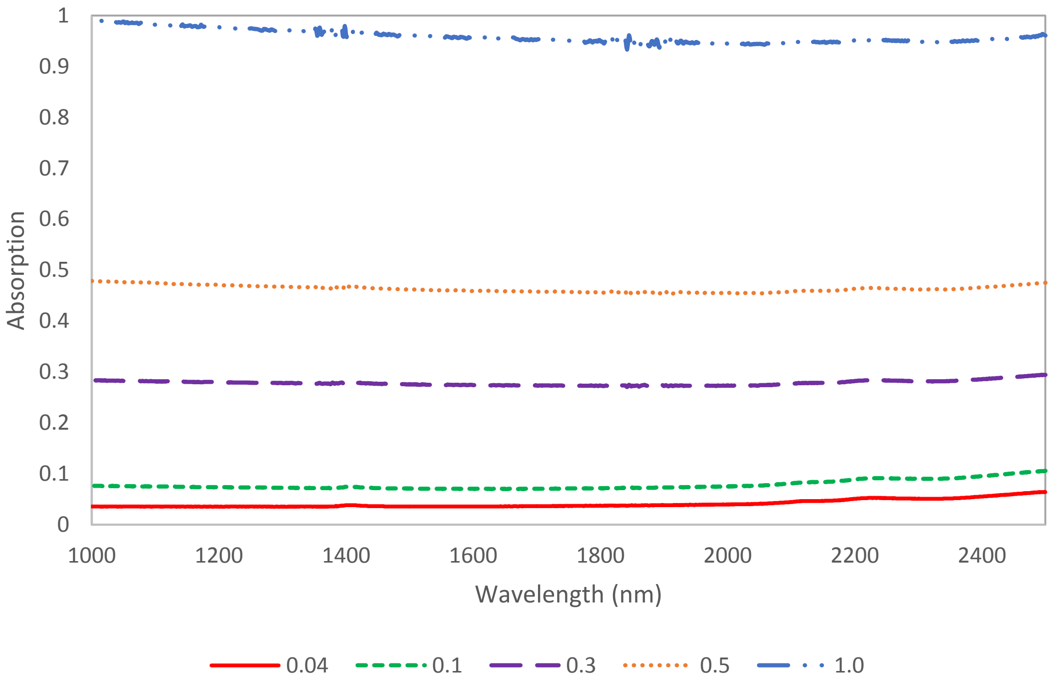

Figure 60 Absorption spectra of NDF using the UV-Vis spectrometer

Figure 60 shows each NDF corresponding to the specified absorption over the 1000-2500 nm region for the UV-vis spectrometer. All of the scans were relatively uniform over the spectrum however, they are all slightly lower than specified absorption. Knowing the uniformity of the NDF they were placed between the Bentham's monochromator optics and PbS detector and scanned 4 times using a 2nm step size. The resulting scans were averaged and are given in Figure 61. The negative log of each filter was taken with respect to the baseline, producing Figure 62. Figure 62 correlates well with the NDF scans using the UV-vis spectrometer in Figure 60, demonstrating the uniformity of the Bentham spectrometer, detectors and success of background removal method.

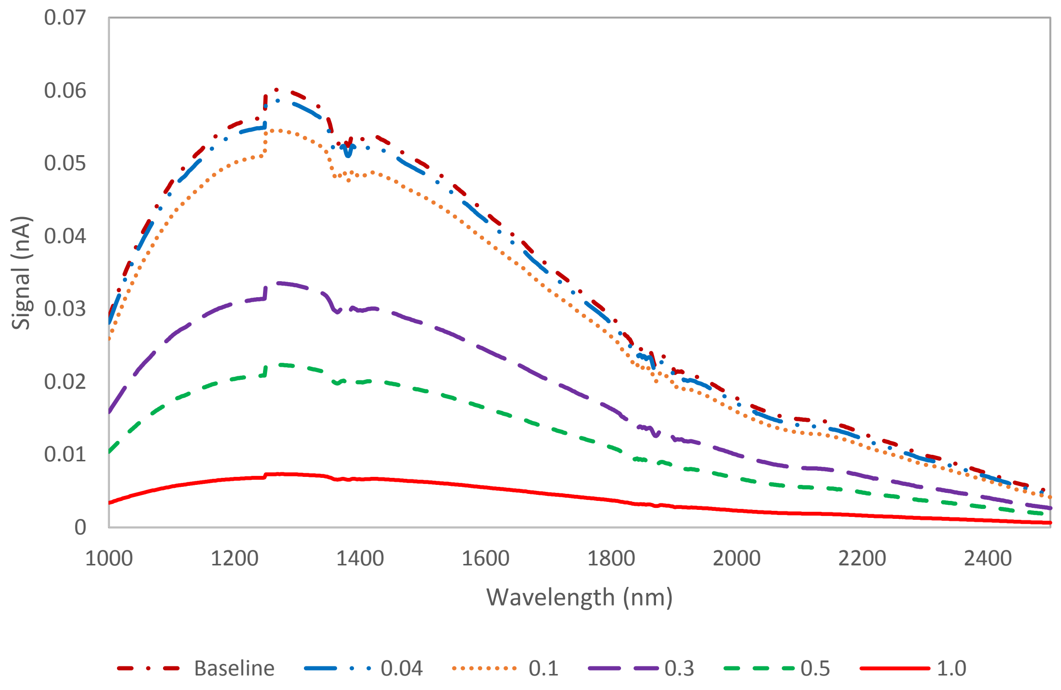

Figure 61 Averages scans of baseline (zero absorption) and NDF using the Bentham fibre spectrometer.

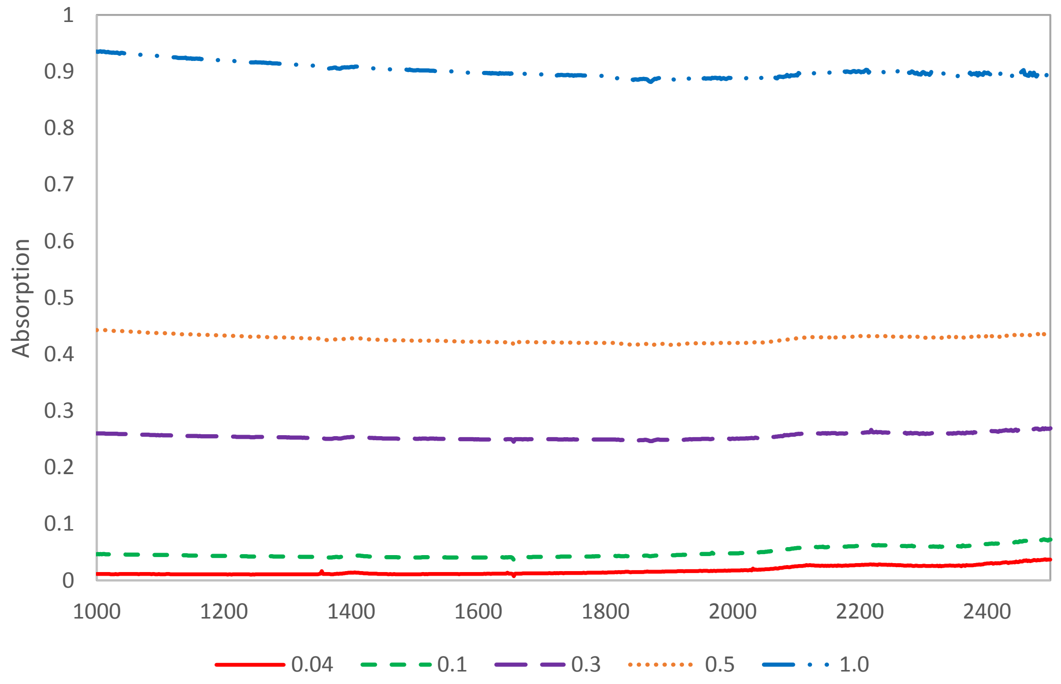

Figure 62 Negative log of NDF with respect to the baseline using the Bentham spectrometer

4.7 Optical absorptions – H3 Glass

4.7.1 UV/Vis/ FTIR Glass absorption spectra

Figure 63 shows a combination of UV Vis and FTIR spectroscopy absorption data for a 1 mm thick piece of parallel H3-glass; the transition from UV Vis to FTIR occurs at 3000 nm. The data naturally contains the reflection losses and any sample misalignment which can cause refractions. The reflection values could not be removed due to the RI values for H3 being unknown over the whole data range. The data has a step change at 875 nm, due to a detector change in the UV-Vis spectrometer. For this thin sample the absorption is at a minimum from 700 nm to approximately 2700 nm. The next prominent feature in the NIR is the absorption band which starts at 2700 nm and slowly drops to 3900 nm before absorption increases to a maximum at around 4300 nm. The prominent broad peak at 2778 nm is due to the fundamental OH vibration [35, 123, 124]. The two peaks at 3450 nm 3525 nm were not fully characterised, however they are suggested to be transition metal hydroxyl vibrations [61, 124]. The final peak part of the absorption around 4300 nm is attributed to hydroxyl groups [61].

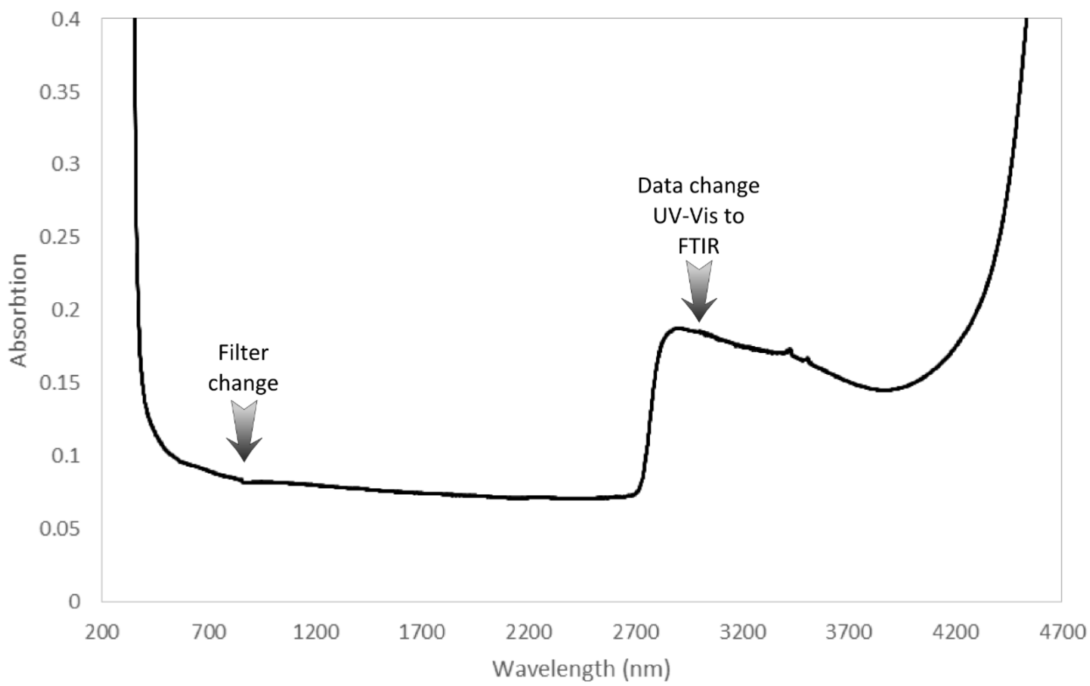

Figure 63 A combination of averaged UV-vis and FTIR spectra of H3-glass changing at 3000 nm.

However, thin samples are not representative of absorptions in the fiberized state and consequently, optical absorptions were also measured using the Bentham fibre spectrometer.

4.7.2 NIR fibre loss spectrums

Fibre loss spectra using the Bentham spectrometer were initially attempted using a single H3 fibre however, due to poor signal level only noise was produced. To increase the signal, bundles of H3 fibres washed in acetone and IPA were threaded through PFTE tubing to facilitate fibre alignment. Fibres were initially lined up at the launch optics and an initial scan was taken. The next scan was taken after cropping the fibres at the detector end. However, during the cropping process the fibres at the launch optics end moved producing a scan of a similar intensity resulting in a loss spectrum of noise. It was then decided to crop back sections of H3 fibres embedded in 828 cured with TETA, as used in the FEWS experiments, this prevented misalignment of the fibres at the launch optics. This however, produced evanescent peaks of the 828/TETA which varied with the embedded length as discussed in Section 2.2.8.1.1, consequently the loss spectrum of H3 was obscured. A unitless loss spectrum of the fibres was produced by subtracting a scan of the H3 fibre bundle from the Bentham's optics and PbS sensor baseline. To give a comparison with loss in dB per mm two sections of H3 bulk glass were scanned and subtracted from each other using the equations given in Section 3.10.4. These scans are given in Figure 64:

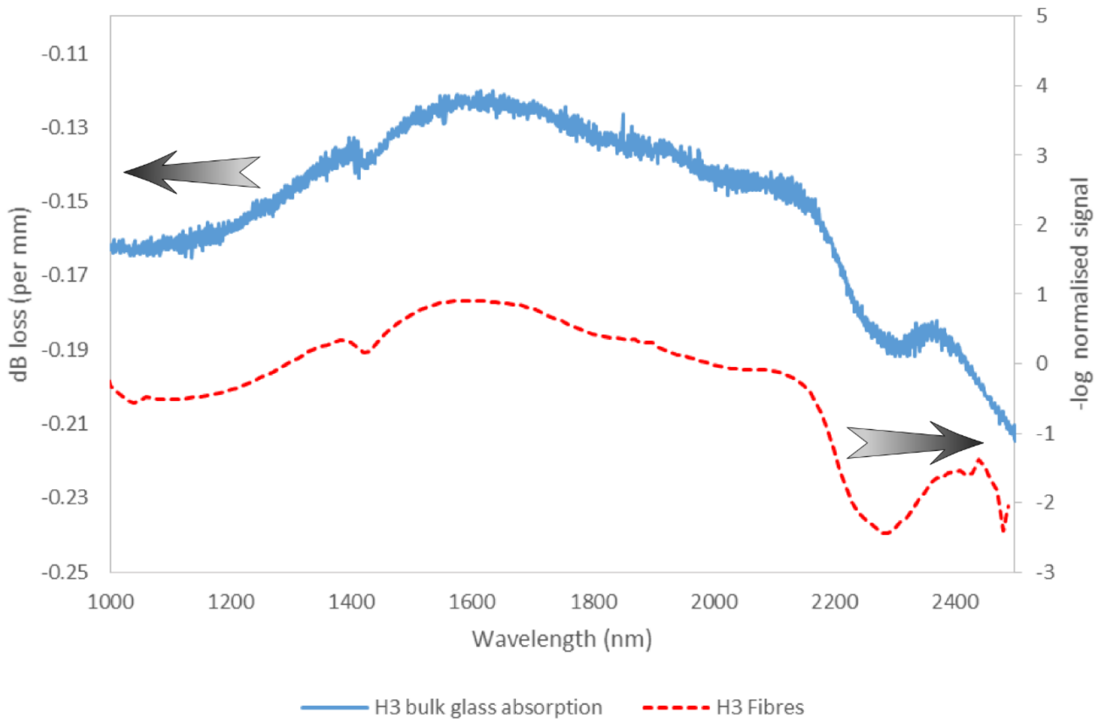

Figure 64 Absorption spectrum of H3 fibres and bulk glass taken from Bentham and UV-Vis spectrometers respectively

The peak around 1420 nm is the first overtone of the free OH vibration [52, 123]. The faint peaks around 1887 - 1923 nm are related to free H_2O and bending H_2O mode whilst 2222-2299 nm are related to free (Si)O–H vibration and bending (Si)O–H mode [123].

The resulting dB loss from UV-Vis bulk glass data does not reflect the resulting final fibres. Using an average dB loss of 0.15dB per mm would result in a power loss of 90% across the spectum at approximately 66 mm of fibre. Seeing as significantly longer fibres of 350 mm were used for FEWS experiments, these values are incorrect. The cause of this inaccuracy is most likely due to the striation in the thick bulk H3 glass sample causing further losses and consequently, an over estimation of the power losses.

4.7.3 Data processing

One of the issues with optical sensors is the intensity variations which can occur throughout an experiment. These can be caused by:

- Fibre movement
    - External environment (air conditioning fans)
    - Resin viscosity changes resulting in fibre movement

    - Vacuum bag pressure
- Refractive index change
    - Cladding RI
    - Reflection from cuvette interface
- Fibre fractures

Consequently, all scans were normalised using feature scaling and setting 1670 nm to a maximum using equation (36). 1670 nm was used seeing as it was the closest peak to the unchanging C-H aromatic vibration overtone peak [6, 12, 113, 114]1668 nm, using the 10 nm bandwidth as shown in Table 28. This was done to remove the previously mentioned intensity variations.

4.7.4 Resin cuvette baseline scans setup

Due to large sensing area of cuvette baseline scans, the signal to noise level was considerably lower in comparison to FEWS experiments. It was decided to use a 2 nm bandwidth enabling good peak detection without taking too long for scans to run producing issues with hot curing samples cooling.

High curing temperature resins were problematic to scan in situ. Both MY721/DDS and MTC801 samples were attempted on a temperature controlled hot-plate; however, this caused the base of the cuvette to fracture and leak. Beyond this, samples were sandwiched between two microscope slides with high temperature tape to hold in the resin, however as the resin was heated the viscosity dropped and the resin leaked.

Finally, the custom-made silica cuvettes filled with epoxy/curing agent blends were oven cured and scanned every hour pausing the curing program for the duration of the 30 minute scan before continuing the cure schedule post scan. However, each scan took 30 minutes to perform due to the 2 nm steps. The oven was paused from the curing schedule; however, this gave time for the resin to cool during the scan, so the scans are not perfectly representative of in situ FEWS cure monitoring.

Baseline NIR scans for PEG300, sunflower oil (SFO), MY721/DDS, 828/TETA and MTC801 as stated in Table 17 are shown in Figure 65, Figure 66, Figure 67, Figure 74 and Figure 85 respectively. Within the resin scans a discontinuity occurs over the expected 2208 nm epoxy CH_2 stretch + epoxy CH_2 deformation such that MTC801 shows the reduction in this band with cure whilst MY721/DDS and 828/TETA have no 2208 nm epoxy peak present. In all cases the cuvette was scanned with no resin as a baseline and all scans when background removed are linear. Background removed cuvette scans are shown in Appendix A. To check for missing 2208 nm peak in both 828/TETA and MY721/DDS were also scanned using FTIR to demonstrate the presence of the 2208 nm peak.

A list of commonly used peaks for cure monitoring of epoxy/amine systems is given in Table 28 [114].

Table 28 NIR peaks of epoxy resins and amines [114]

Wavelength (nm)	**Assignments**
1429	OH stretch overtone
1460	NH_2 asymmetric stretch overtone
1503	NH_2 symmetric + asymmetric stretch
1526	NH_2 symmetric stretch overtone
1648	Epoxy terminal CH_2 stretch overtone
1669	Phenyl CH stretch overtone
1698	Epoxy CH/CH_2 combination
1735 - 1769	CH/CH_2 overtones
1980	NH_2 combination
2045 - 2089	OH combination
2163	Phenyl CH stretch + phenyl conjugated stretch
2208	Epoxy CH_2 stretch + epoxy CH_2 deformation

4.8 Liquid systems fibre evanescent wave spectroscopy and baseline scans

As previously stated, initial scans using H3 fibres were run using single fibres. However, the signal to noise ratio was very poor. Consequently, bundles of H3 fibres containing 6 to 25 fibres were used for FEWS experiments. Fibre bundles were supported using PTFE tubing with a 1 mm internal diameter as shown in Section 3.10.4. Initial scans were trialled with 2 nm step sizes producing a spectrum of noise. An increase to 5 nm step sizes enabled a scan, but the signal to noise level was still too high concealing the evanescent wave peaks in the noise. A bandwidth of 10 nm was chosen providing the lowest practical signal to noise whilst still maintaining a bandwidth suitable for peak detection.

For the initial experiments using fibres with diameter >150 µm a fibre optic cleaver was used, which clamps the fibre between two supports and then a diamond blade scores the edge of the fibre and a final support bends the clamped fibres producing an ideal cleave. Smaller diameter fibres in later experiments were problematic to cleave using a fibre cleaver. Consequently fibres were pre-tensioned around a cylinder and cleaved using a fresh razor blade as performed in [55]. The fibre optical cleaver produced a significant intensity increase when compared to scalpel cropping in larger fibres however, the cleaver could not be adjusted for use with <150 µm fibres.

4.8.1 PEG300 – Poly(ethylene glycol)

Figure 65 shows the baseline cuvette scan of PEG300 and the subtraction of H3 FEW experiment. The FEWS experiment demonstrates no evanescent wave peaks. The absence of evanescent wave peaks is related to the large average fibre diameter of 261 nm. PEG300 has a low refractive index of 1.465 n_D which reduces the level of evanescent peaks as stated in Section 2.2.8.1.1. The short embedded length of 60 mm will have also contributed to the absence of the peaks.

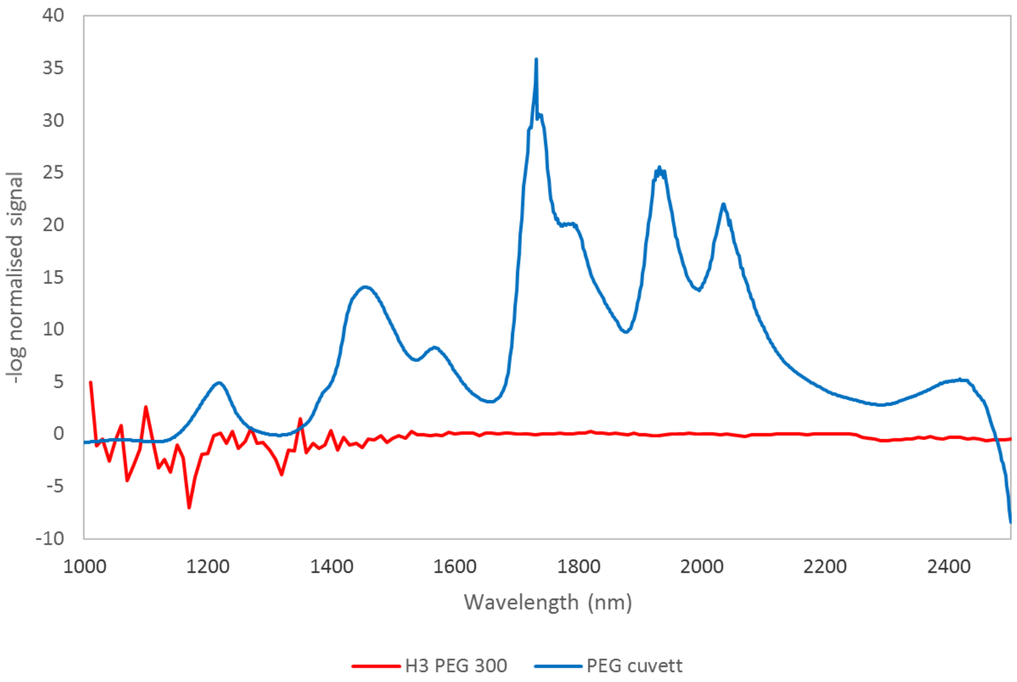

Figure 65 NIR Spectra of PEG300 by H3 fibres FEWS and scan of cuvette

4.8.2 Sunflower oil (SFO) experiments

Due to the poor results of initial PEG300 FEWS scans, it was decided to produce finer fibres more suitable for FEW monitoring. SFO possessed a marginally higher refractive index 1.472-1.474 n_D [125] than PEG300, promoting evanescent waves. A custom-made cuvette filled with SFO was scanned using the Bentham spectrometer for NIR peaks. A H3 fibre bundle was then scanned with SFO applied to the fibres surface producing a 130 mm pool. The resulting Beer Lambert processed H3 FEWS and UV-Vis scans are shown in Figure 66.

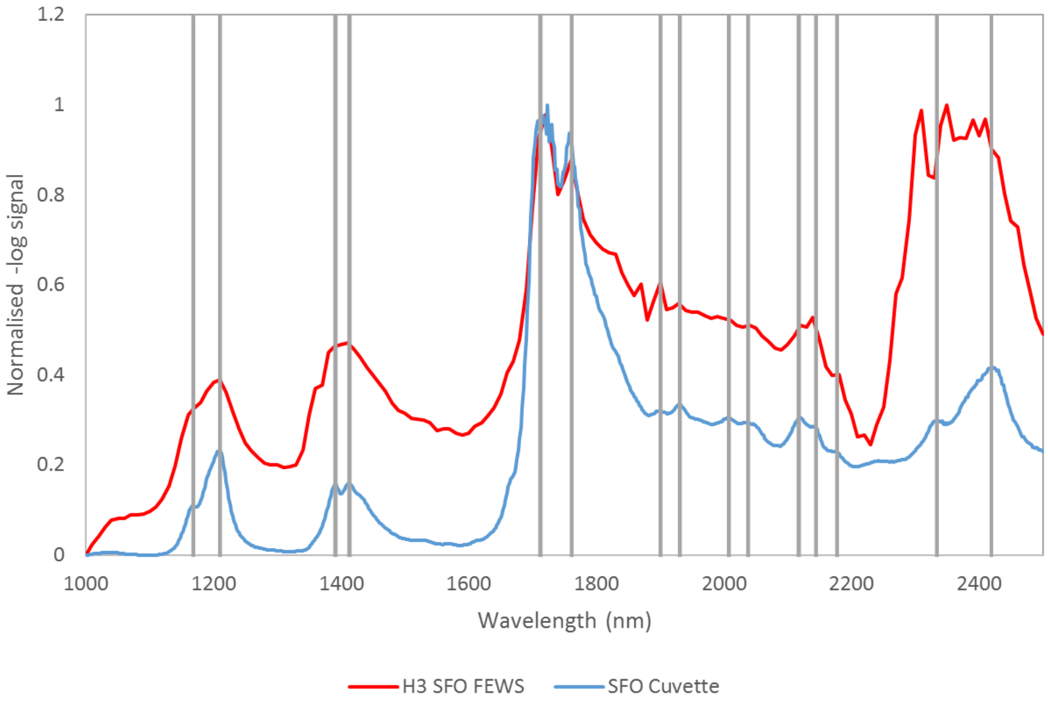

Figure 66 H3 FEWS and baseline cuvette spectrometra of sunflower oil with highlighted peaks showing correlated peaks.

Figure 66 shows a good correlation between the evanescent wave peaks and the UV Vis spectrum, demonstrating H3 fibre FEWS sensing with fibres <125 µm from 1000-2230 nm. As stated in Section 2.2.8.1.1 the finer the fibre the stronger the evanescent field and resulting absorption spectra. This is beneficial from an integration into PMC allowing for finer fibres which possess superior compressive properties and prevent resin rich regions which form around large diameter fibres. The peak mismatches below 2230 nm suggest that the 2222-2299 nm sillica hydroxly vibrations have an intense abosorption band preventing H3 fibres from cure monitoring any higher than this band.

4.8.3 MY721/DDS

The greatest evanescent peak intensity is produced when the RI of the cladding and core are closely matching as stated in Section 2.2.8.1.1. Consequently, H3 FEWS was performed with MY721/DDS resin system over a hot plate set at 200 °C as stated in Section 3.10.4.

The pure resin baseline scan was difficult to attain for MY721/DDS. During the initial stages of cure the resin was a liquid and scans followed a similar spectrum. However, once the sample had been cured for two hours the sample was at 200 °C and upon removal from the oven the resin darkened and the cuvette thermally shocked. The resulting scans shown in Figure 67 demonstrate a dramatic shift in peaks between 2 to 3 hours.

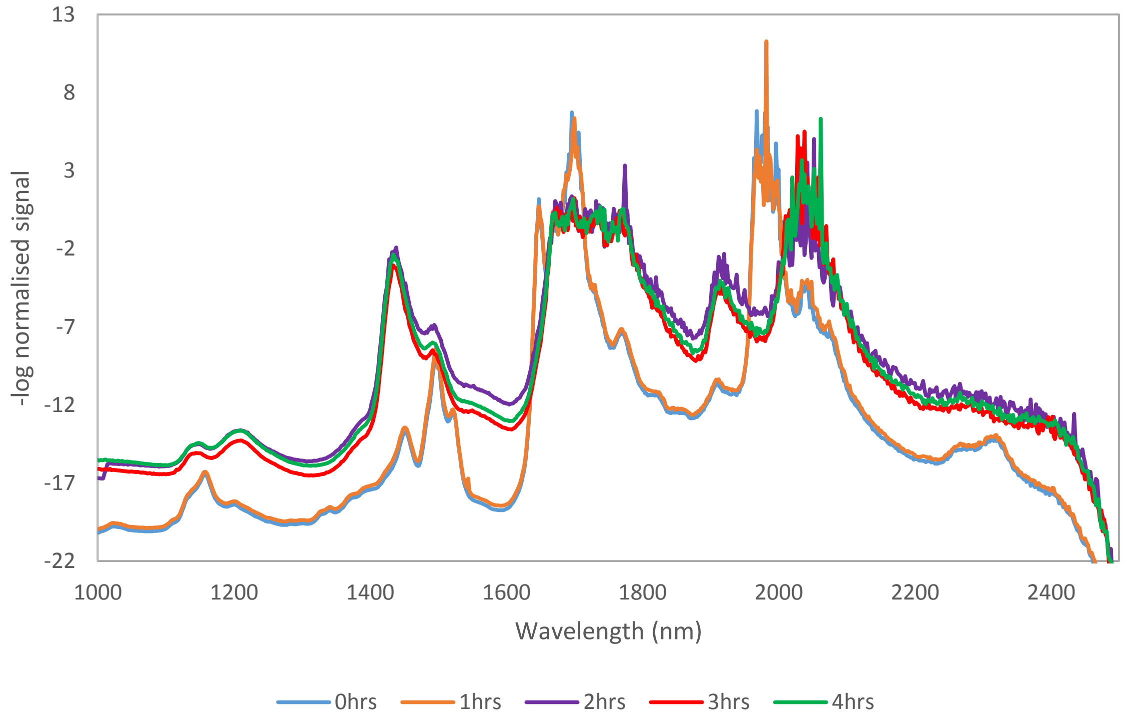

Figure 67 Baseline NIR peaks of oven cured MY721/DDS in a custom cuvette

There are many peaks in Figure 67 however, the dramatic shift in intensity due to thermal shocking of the cuvette made data normalisation difficult. The scan was repeated for the first 2 hours followed by a scan of a cast cured sample which is shown in Figure 68.

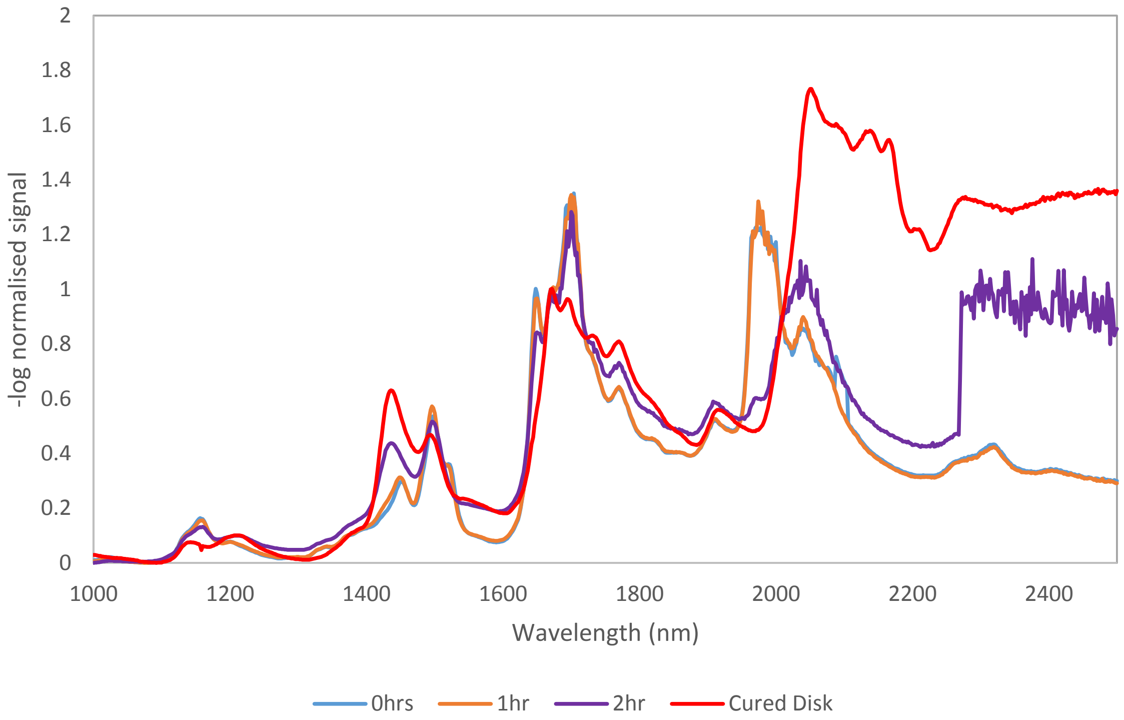

Figure 68 Normalised and baseline subtracted NIR peaks of oven cured MY721/DDS in a custom-made cuvette from 0 to 2 hour followed by a scan of a fully cured resin sample

Figure 68 demonstrates the largest peak shift in the 2042 nm band and the 1974 nm band which correspond to the OH combination and NH_2 combination vibrations respectively [52]. As expected from the curing reaction of amines with epoxies shown in Figure 3 the NH_2 band decreases with time whilst it reacts with the epoxy groups and the OH group will increase as epoxy groups generate hydroxyl groups. The ideal frequency given by George *et al* [52] for the cure monitoring of MY721/DDS is 1974 nm (5067 cm^{-1}). In both Figure 67 and Figure 68 there is an absence of the 2208 nm epoxy peak which in DDS cured systems should combine with the 2205 nm primary amine from DDS [126, 127] producing a strong peak for sensing. To check for the absence a small amount of MY721/DDS was added to a potassium bromide (KBr) disk and scanned in the NIR region producing Figure 69.

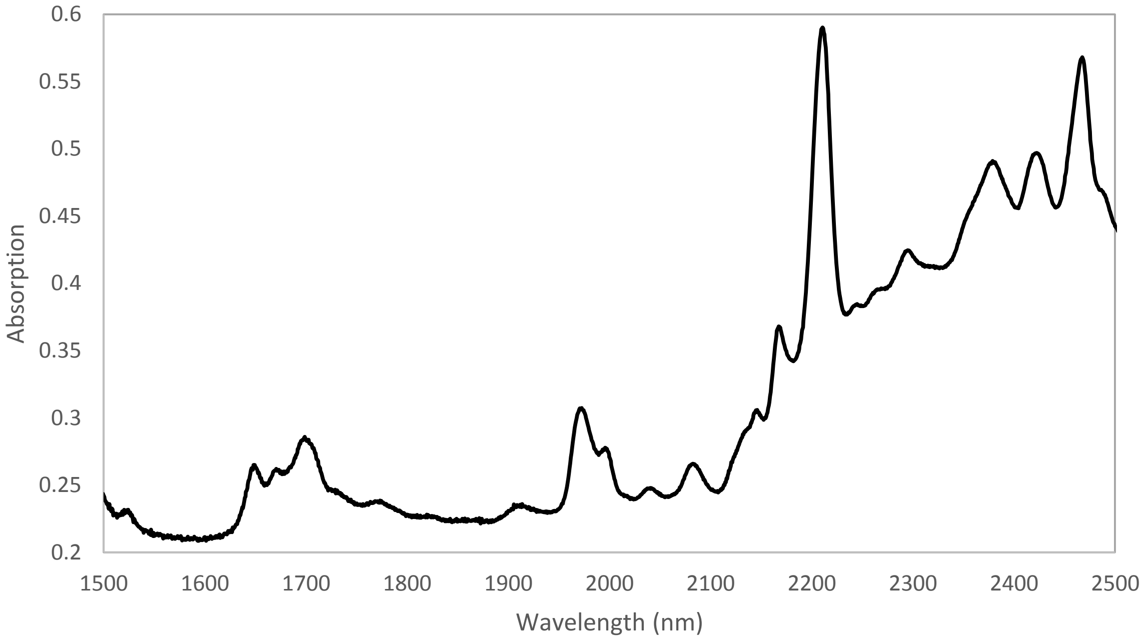

Figure 69 FTIR spectrum of MY721/DDS smear on a KBr disk in the NIR region

Figure 69 shows the existence of the 2205/2208nm DDS primary amine/epoxy peak. FEWS cure monitoring of MY721/DDS with H3 fibre bundles was then attempted using a hot-plate set to 200 °C covered in PTFE. The processed data is shown in Figure 70.

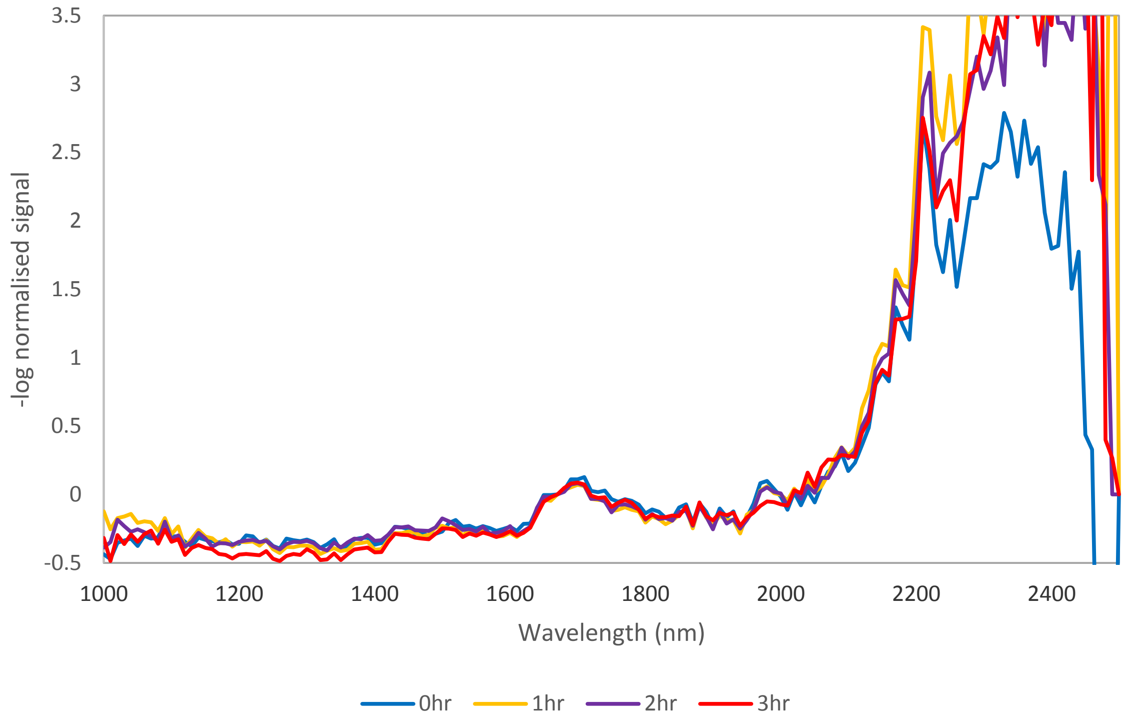

Figure 70 H3 FEWS cure monitoring of MY721/DDS cured at 200°C

The OH band at 2040 nm shows a small increase in intensity however, the cure was not monitored for long enough to see a significant rise in this peak as shown in Figure 68. Consequently, the results are inconclusive regarding the suitability of the hydroxyl combination vibration for cure monitoring.

As with the FTIR spectrum the H3 fibre allows the 2210 nm epoxy peak to become visible. However, the expected trend is not produced with the initial scan showing a low epoxy level that the 3 hours. However, beyond this initial anomaly the 1-3 hr peak reduces in level as the epoxy groups are used up. An explanation for this is a high signal to noise ratio over the scan.

The NH_2 peak at 1970 nm (1970 nm was used due to 10 nm step size limiting use of the exact 1974 nm peak) shows a decrease with time demonstrating FEWS cure monitoring of MY721/DDS. Figure 71 shows the normalised 1970 nm peak intensity plotted against time. Previously cure monitoring has been demonstrated using the peak area [128] however, due to the high noise levels and low bandwidth it was decided that the plot of peak height gave a better measure of reactive group intensity.

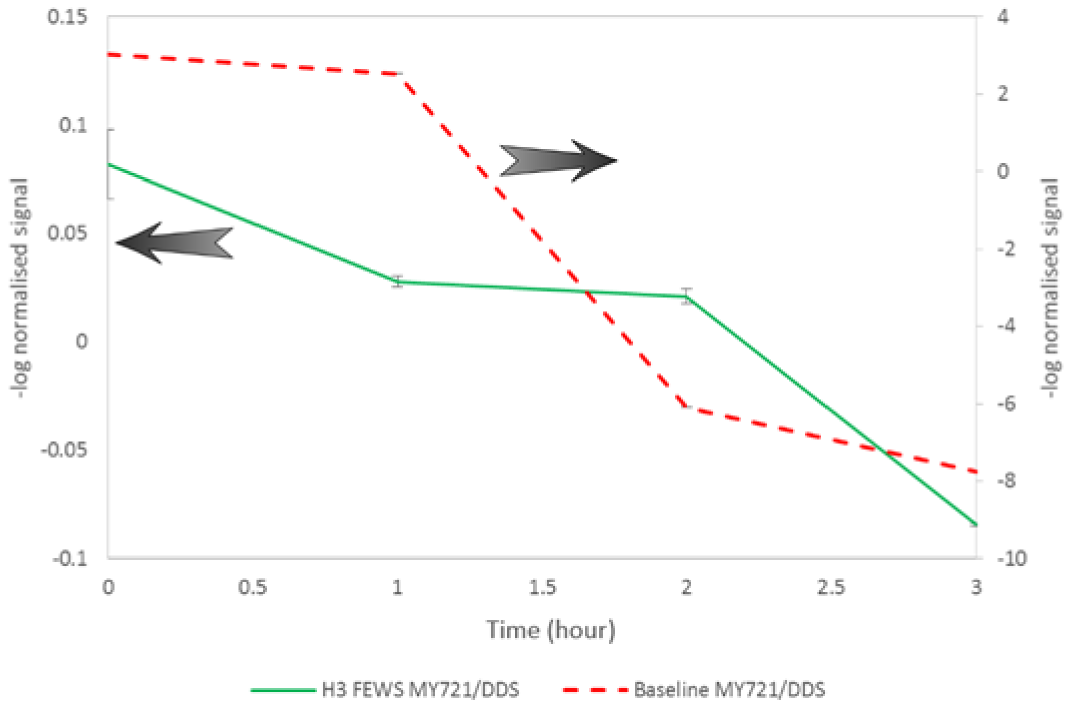

Figure 71 Progression of MY721/DDS H3 FEWS cure monitor and baseline scan using the normalised 1970nm peak intensity. Error bars show standard deviation of the data

Figure 71 demonstrates the reduction in the NH_2 peak of both the baseline and FEWS monitoring with time. The error bars show a good correlation of the NH_2 reduction demonstrating the concept of cure monitoring in high RI resins.

DSC was performed on the as-mixed MY721 and DDS resin system. The raw data is shown in Figure 72 and the resulting extent of conversion from equation 34 is given in Figure 73. Whilst Figure 71 demonstrates a decrease in amines, not enough data was gathered due to a computer failure. Consequently, no comparison can be made with the DSC extent of reaction.

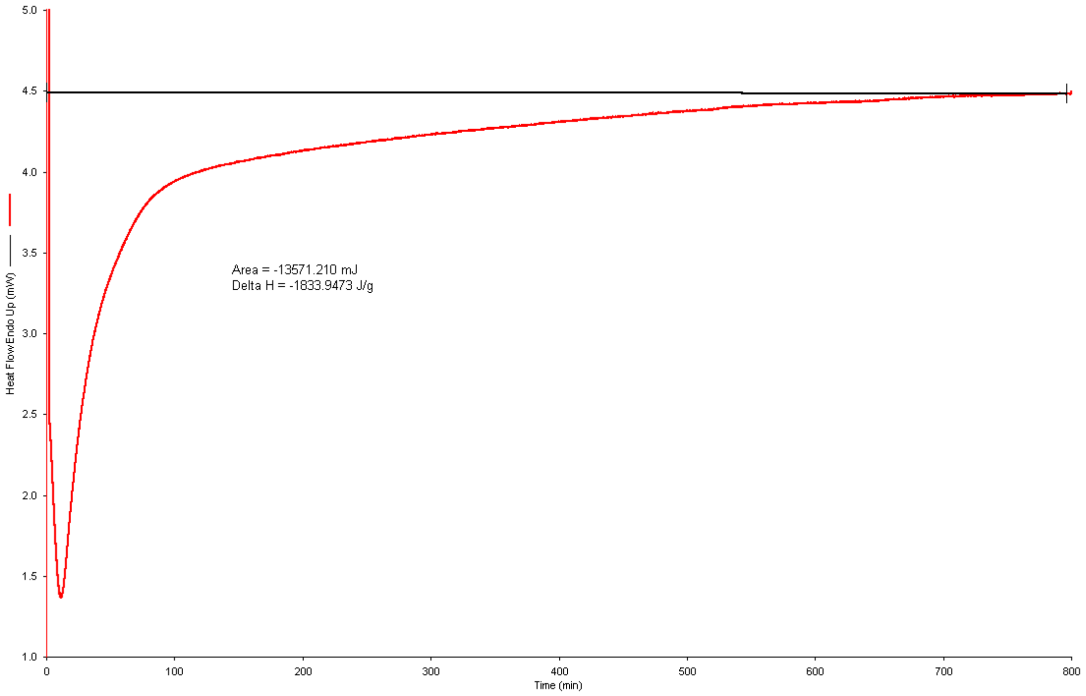

Figure 72 Raw isothermal DSC data from MY721 DDS cureing at 200 °C

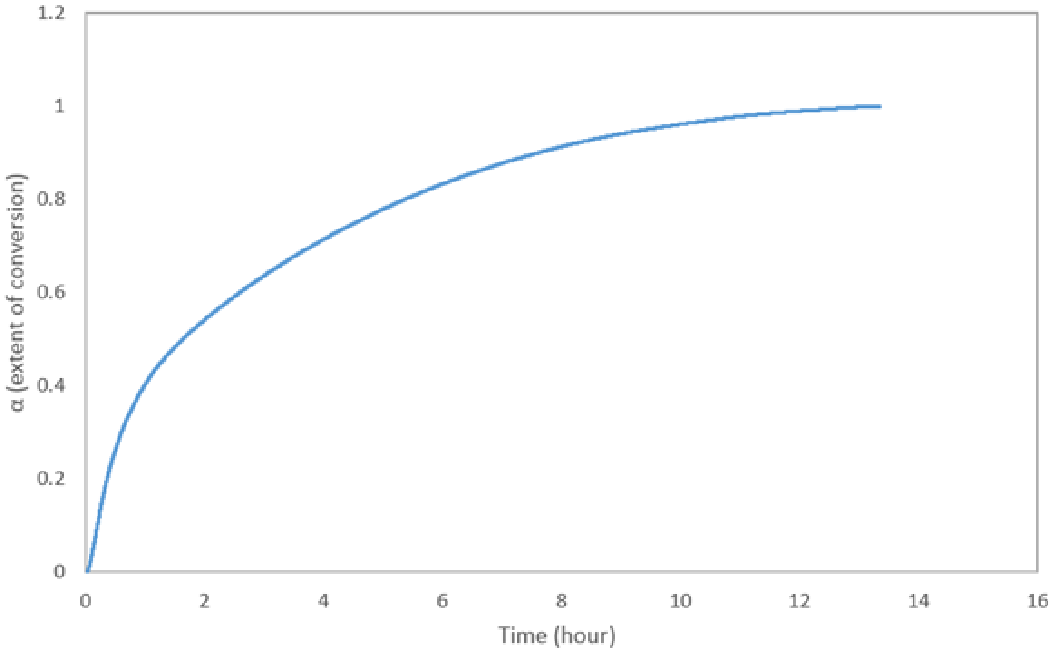

Figure 73 Extent of conversion from isothermal DSC of MY721 DDS at 200 °C

4.8.4 828/TETA

828/TETA was investigated to demonstrate cure monitoring with a lower RI epoxy resin using an aliphatic curing agent. A baseline NIR scan of 828/TETA curing in a glass slide cuvette at room temperature is shown in Figure 74. The two highly prominent peaks shown are at 1540 nm which shift towards 1550 nm as the resin cures and the 2025 nm peak. These are allocated to the 1543 nm aliphatic secondary amine overtone stretch and the 2025 nm primary amine combination overtone stretch [12, 129].

Figure 74 has no 2208 nm epoxy peak, and to check for the existence of the 2208 nm peak 828/TETA was added to a potassium bromide (KBr) disk and scanned in the NIR region using FTIR producing Figure 75. Figure 75 shows a 2208 nm epoxy peak exists for 828 TETA samples.

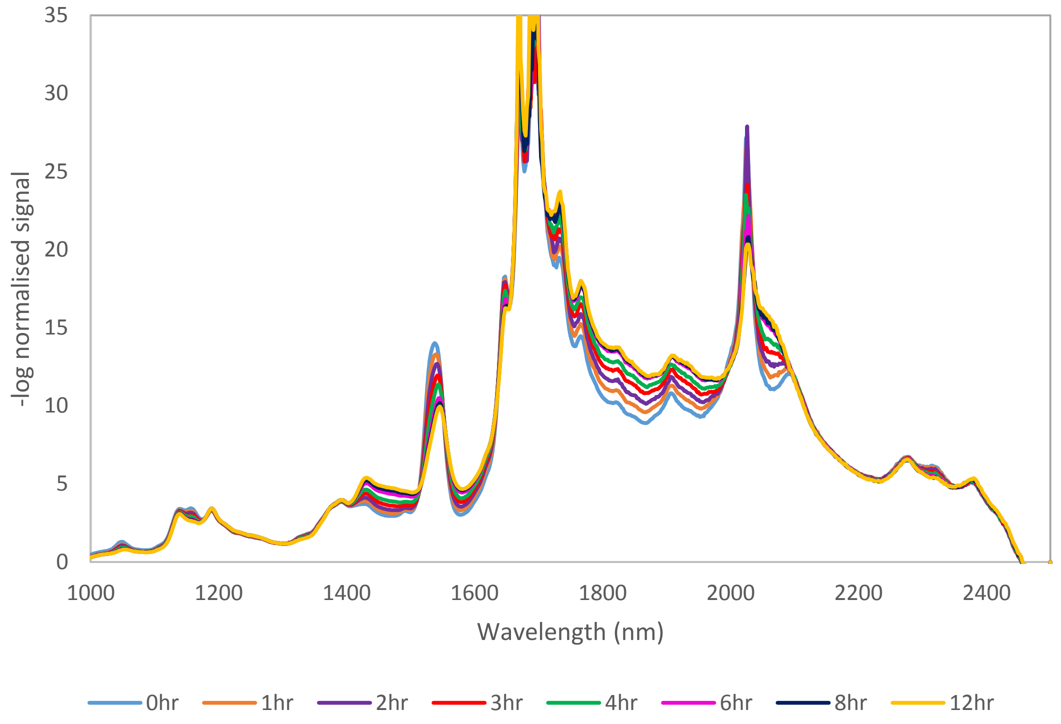

Figure 74 NIR baseline scans of 828/TETA through a glass slide cuvette

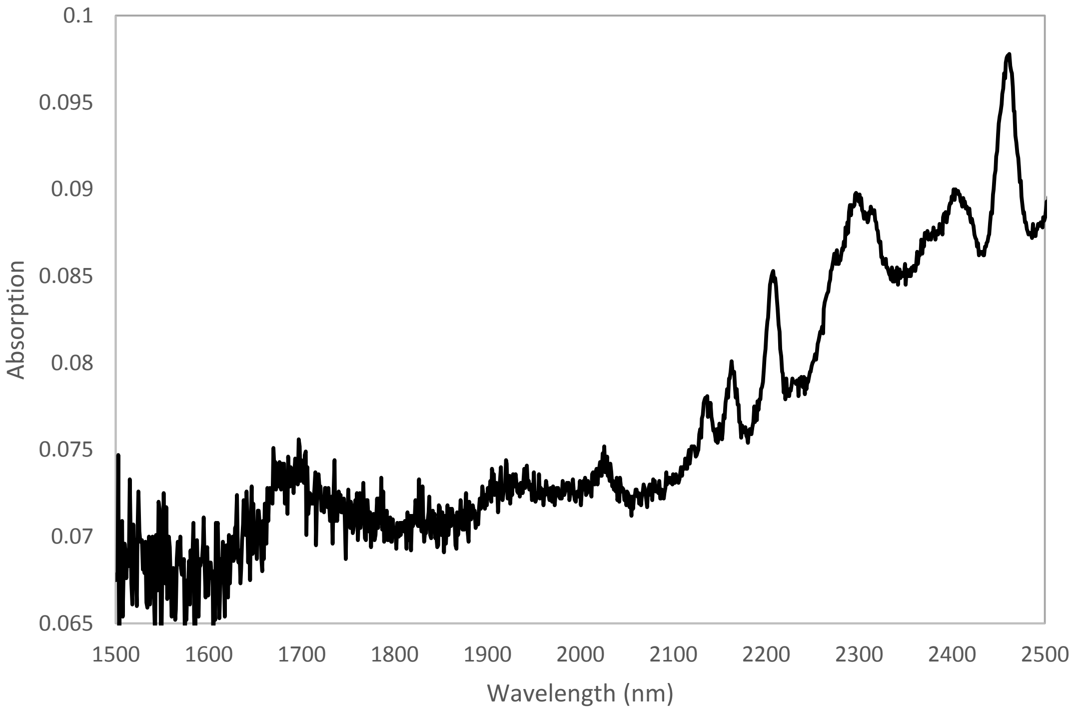

Figure 75 FTIR scan of 828/TETA smear on a KBr disk in the NIR region

Due to 828/TETA cure monitoring being at room temperature, many experiments were tested using this resin system, the parameters are given in Table 18. Samples 828/TETA 1 to 3 all produced poor results and final graphs are shown in the Appendix B. The reasoning for these scans producing poorly defined peaks is due to the limited transmitted signal and large fibre diameters. H3 FEWS scans of 828/TETA 3, 4 and 5 had finer fibres with larger embedded lengths producing defined peaks. These resulting spectra are given in Figure 76 – 79 respectively.

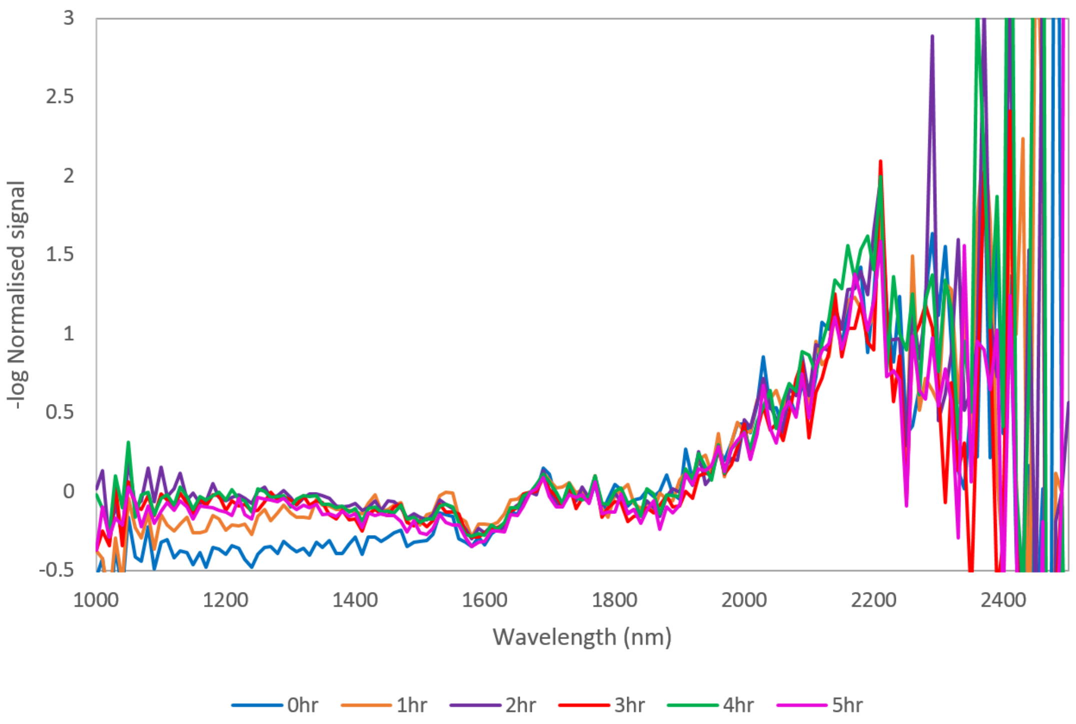

Figure 76 H3 FEWS cure monitoring of 828/TETA 4

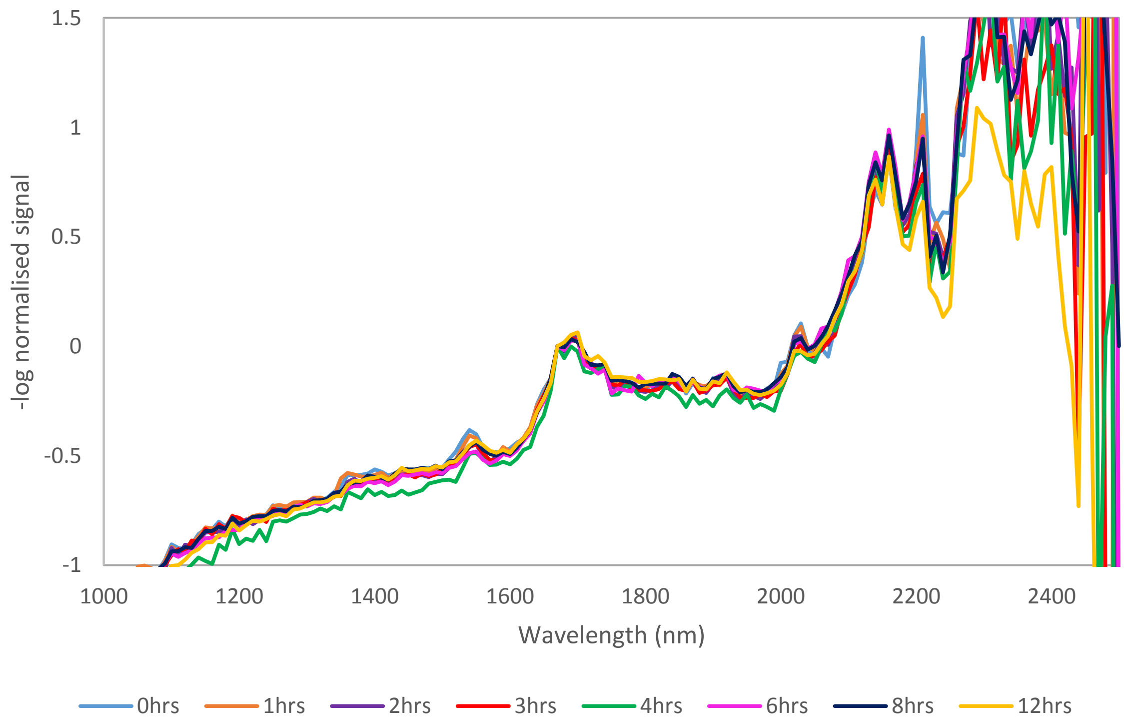

Figure 77 H3 FEWS cure monitoring of 828/TETA 5

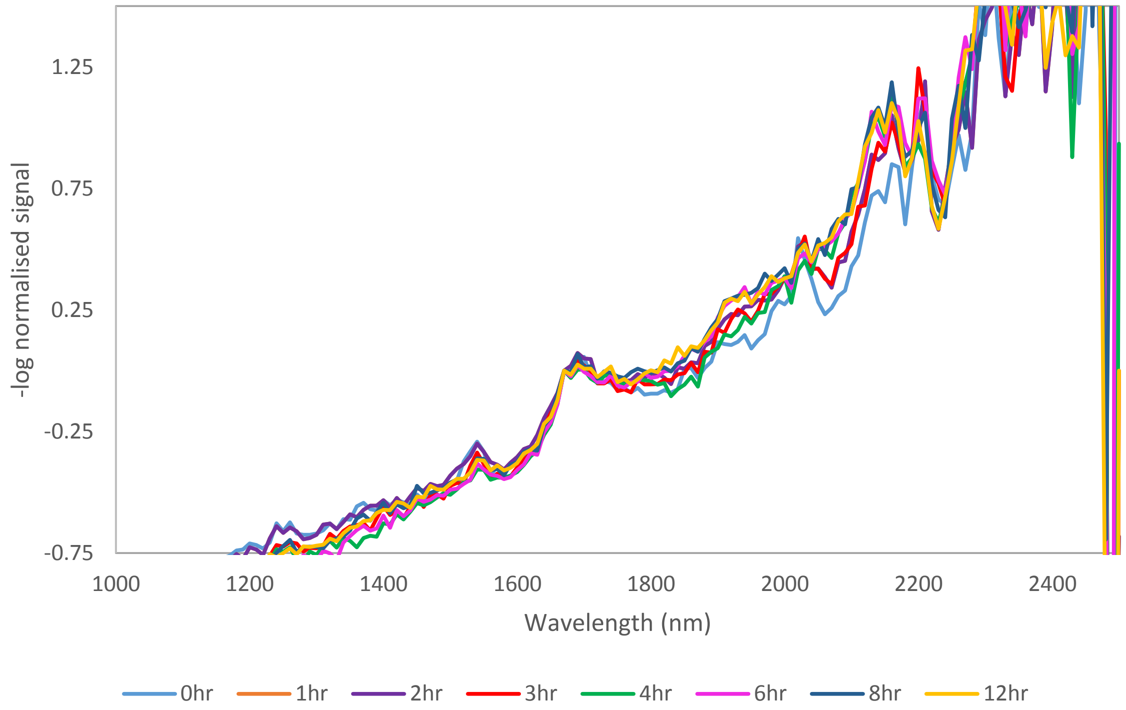

Figure 78 H3 FEWS cure monitoring of 828/TETA 6 cured at 150°C

Figure 76, Figure 77 and Figure 78 all show the 1543 nm aliphatic secondary amine overtone stretch, the 2025 nm primary amine combination overtone stretch and 2208 nm epoxy peak. These peaks were examined for the expected intensity drop with time/cure. The aforementioned peaks progression was plotted with time and shown in Figure 79, Figure 80 and Figure 81 respectively.

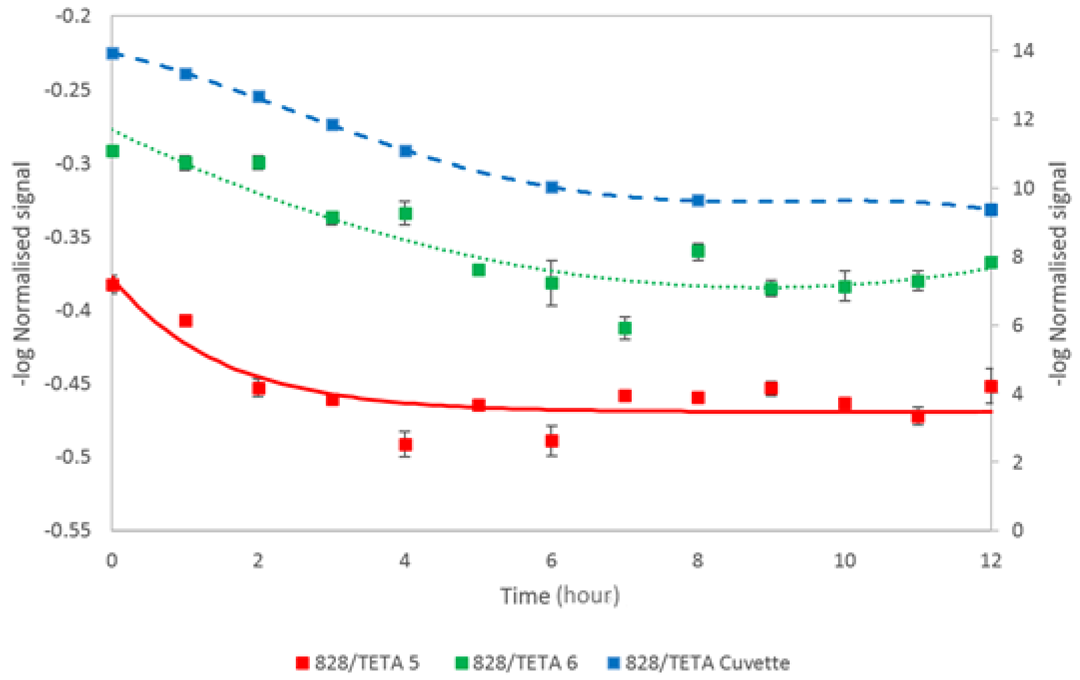

Figure 79 Progression of 828/TETA 5 and 6 H3 FEWS cure monitoring and baseline scan using the normalised 1540nm peak intensity. Error bars show standard deviation. (use hour or hr instead of hrs in the x-axis title to keep the unit consistent in the thesis)

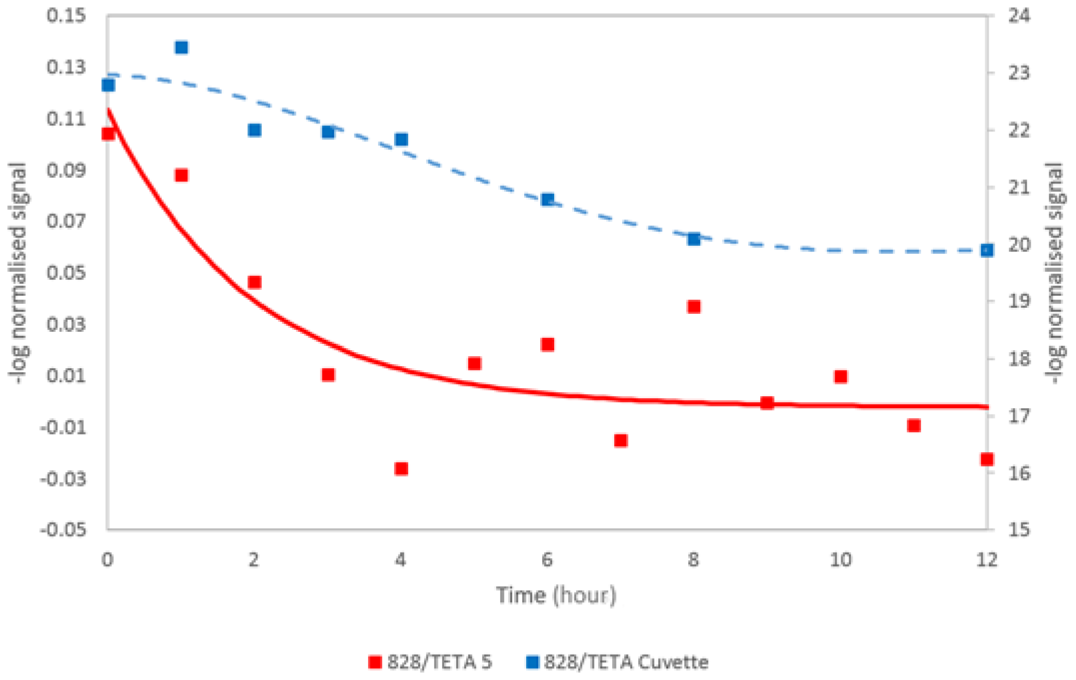

Figure 80 Progression of 828/TETA 5 cure monitoring and baseline scan using the normalised 2030 nm peak intensity. With an exponential decay trend line. Error bars show standard deviation

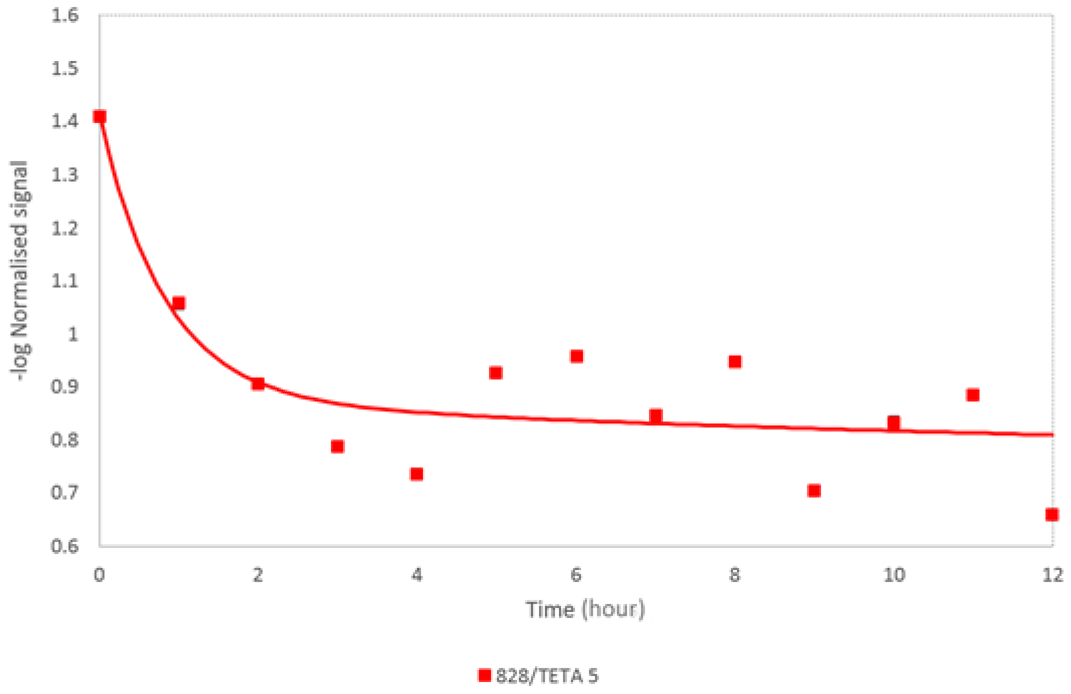

Figure 81 Progression of 828/TETA 5 cure monitoring using the normalised 2210 nm peak intensity. With an exponential decay trend line. Error bars show 1 standard deviation.

Figure 79, Figure 80 and Figure 81 all show a general drop in peak intensity over the first 6 hours followed by a levelling of the signal. This levelling of the signal demonstrates a maximum level of cure.

The only scan which demonstrated a reduction of peaks during the cure was 828/TETA 5 whilst 828/TETA 4 and 6 have a large noise level and resulting time plots show no trend. 828/TETA 5 had the least noise in the data enabling the determination of a trend. However, it is clear from Figure 79, Figure 80 and Figure 81 that an exact quantitative cure was not possible due to the noise level. The FEWS peaks trend lines follow a very similar trend to the baseline cuvette scan for 1540 nm and 2030 nm peaks. The 2210 nm epoxy peak in 828/TETA 5 produces the largest intensity drop demonstrating it as the most suitable peak for cure monitoring of 828/TETA in this case.

DSC was performed on the 828/TETA system. The raw data is shown in Figure 83 and the resulting extent of conversion from equation 34 is given in Figure 83.

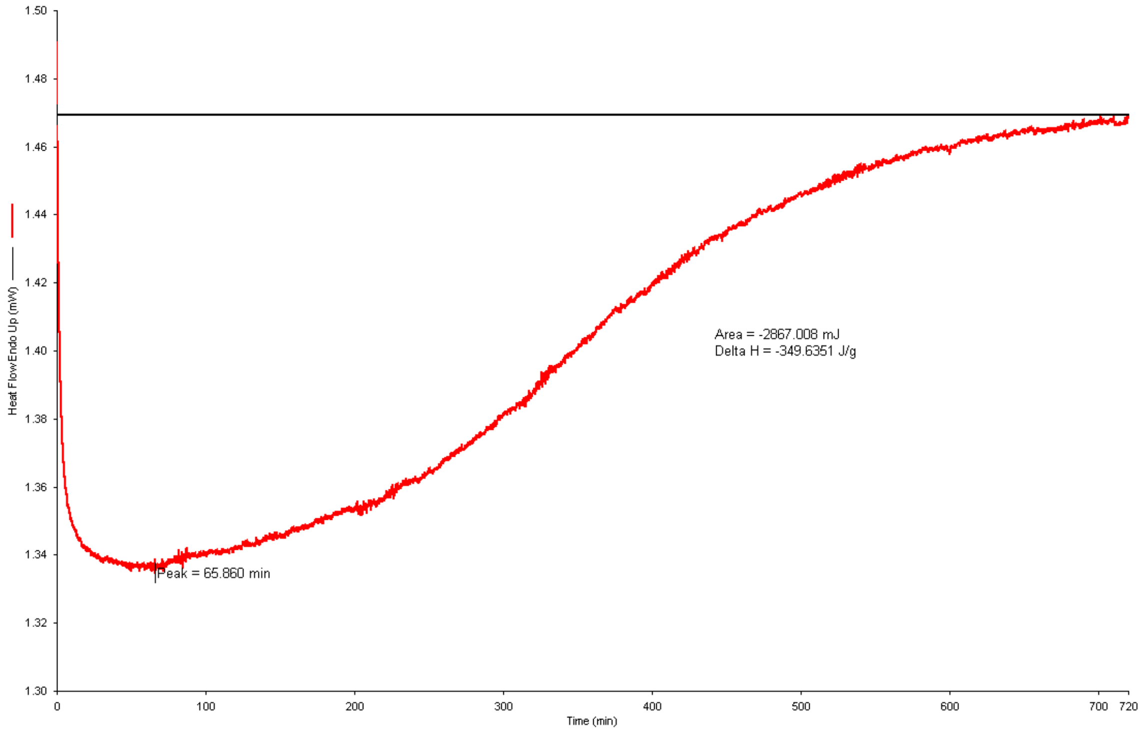

Figure 82 Raw isothermal DSC data from 828 TETA cureing at 20 °C

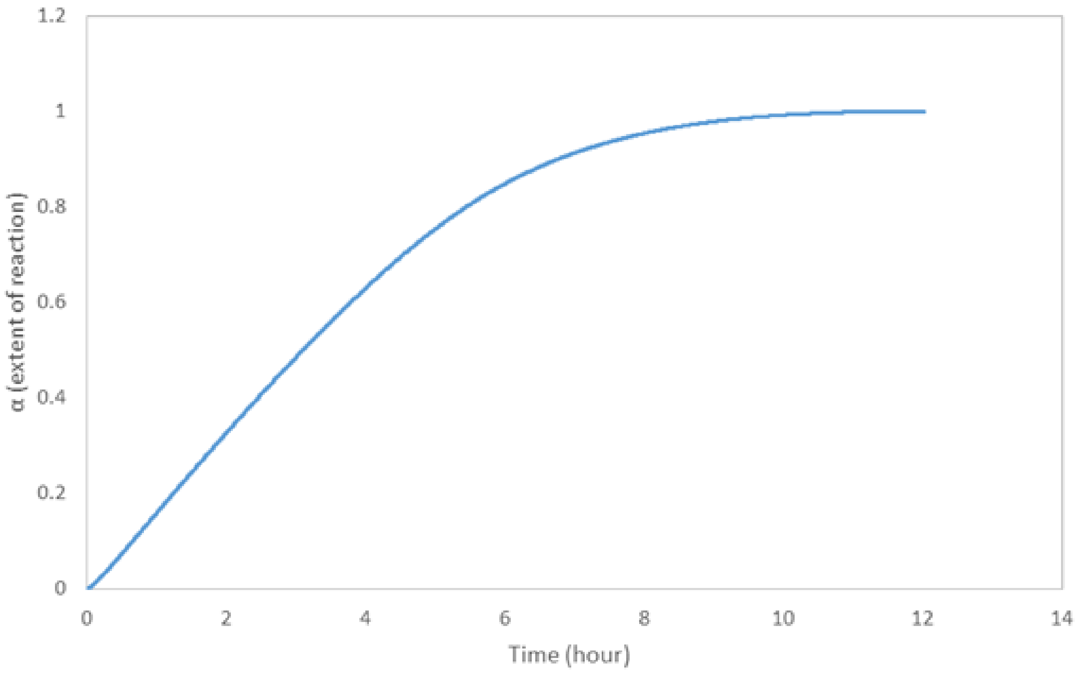

Figure 83 Extent of conversion from isothermal DSC of 828 TETA at 20 °C

The normalised peak intensities from Figure 79, Figure 80 and Figure 81 were plotted against the extent of conversion from isothermal DSC of 828/TETA from Figure 83 resulting in extent of conversion plot shown in Figure 84.

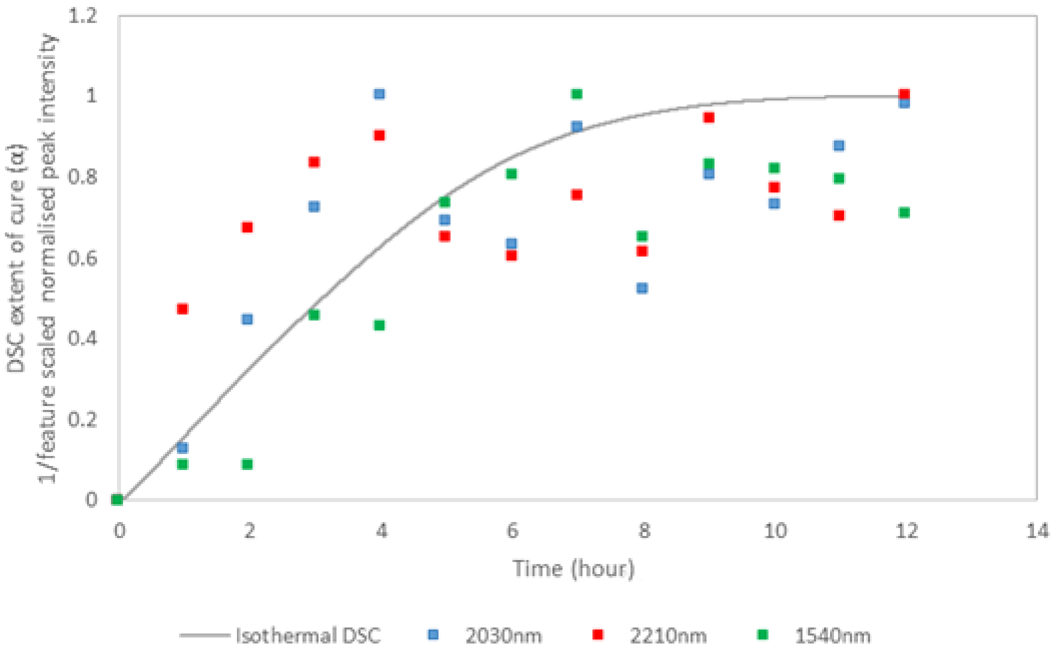

Figure 84 Extent of reaction using DSC against 1- (feature scaled, peak intensity verse time) for 2030, 2210 and 1540 nm peaks from the 828 TETA 5 FEWS experiment

Figure 84 further demonstrates that the peak intensity generally follow the DSC extent of reaction; however, due to high level of noise no clear kinetic data could be observed.

4.9 Electrically cured MTC801 FEWS

4.9.1 Vacuum bag construction

Many methods of vacuum bagging of electrically cured composites were trialled during experimentation. Initially, PTFE tubing had only covered the sections of the H3 fibres running through the tacky tape. This method provided sharp angles over the tacky tape and into the composite resulting in many fractured fibres during the application of vacuum. The next attempt was to cover the fibre bundles in PTFE tubing apart from the exposed section for FEWS; PTFE tubing was placed into the composites 10 mm either side of the composite edge. This was done to reduce the angle on the fibres and to seal the tube and resulting vacuum bag upon heating and resin flow into the tube. To minimise disruption to the composites during cure, a slit was placed 5 mm up the end of the tube inside the composite, this enabled a smaller entrance to block. As the panel heated and resin started to flow, the vacuum sealed enabling consolidation of the panel.

4.9.2 MTC801 NIR baseline spectra

Figure 85 shows the baseline cure of MTC801 resin system. As the resin cured it turned from white to clear during the first hour due to the thermoplastic toughening agent dissolving into the epoxy. The raw data show a significant intensity increase when the thermoplastic dissolves into the resin. This is passed onto the baseline scan in Figure 85 of the 0 hr scans having a different intensity followed by a uniform spectrum beyond the first hour. Although some of the peaks vary over the course of curing, the greatest intensity change occurs at 2208 nm which corresponds to epoxy CH_2 stretch and epoxy CH_2 deformation [114].

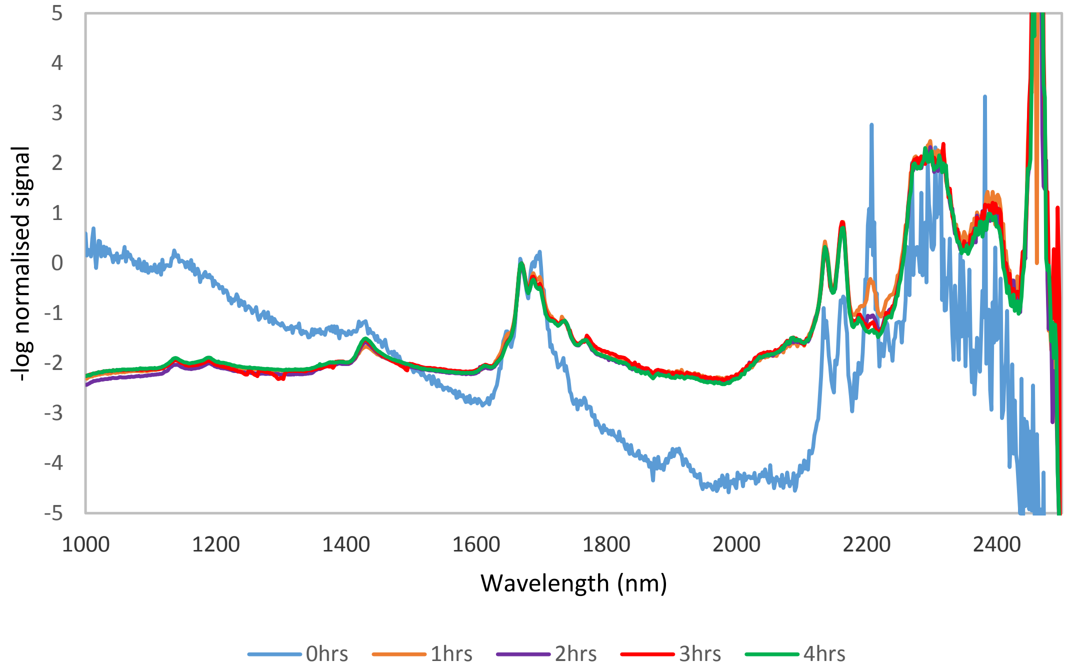

Figure 85 Baseline NIR spectra of DCM extracted MTC801 resin

4.9.3 MTC801 NIR FEWS spectra

Electrical cured FEWS MTC801 spectra are shown in Figure 86 and Figure 87. It was worth noting that very poor signal level was attained for both electrically cured panels.

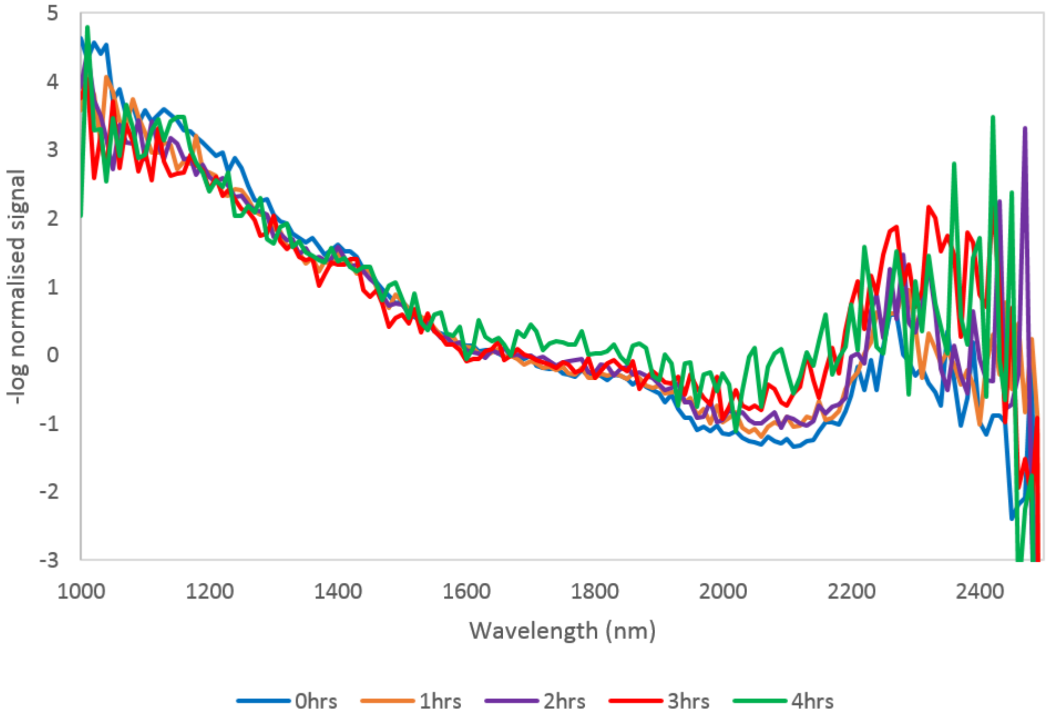

Figure 86 FEWS cure monitoring of electrically cured MTC801 carbon pre-preg (no vacuum pressure)

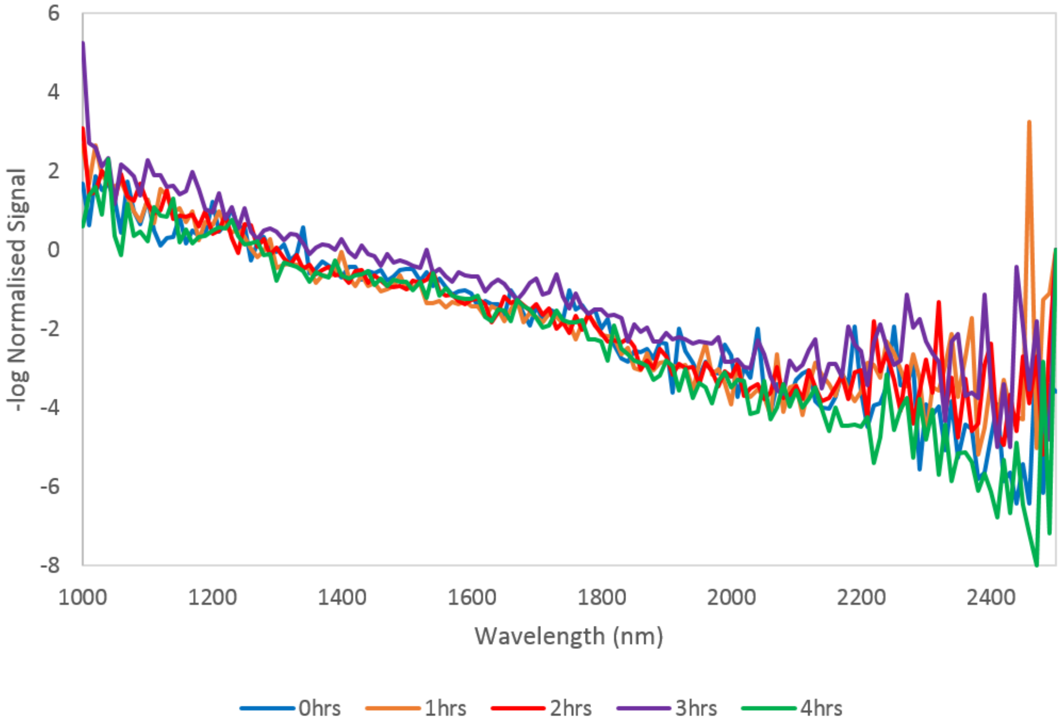

Figure 87 FEWS cure monitoring of electrically cured MTC801 carbon pre-preg (vacuum bag pressure)

The curing temperature profile and actual panel temperature for the FEWS panel is shown in Section 3.10.7. Figure 86 was cured using no vacuum to maximise the signal level preventing bending of the H3 fibres whilst, Figure 87 was cured under vacuum pressure. As previously stated in Section 3.10.7, due to limited availability to take a baseline scan of the H3 fibres prior to FEWS cure monitoring an averaged H3 fibre baseline from the same batch of glass fibres was used for Beer Lambert processing. This would have enable visualisation of any evanescent wave peaks in the resulting spectra.

Figure 86 and Figure 87 demonstrate no peaks with no correlation to Figure 85. This could be due to a combination of problems including the initial low signal intensity causing a large signal to noise ratio obscuring any peaks. The justification for poor signal is due to the H3 fibres contact with carbon fibres. The carbon fibres will inherently absorb the light. Another issue could have been the embedded length which was only 80 mm in both cases; curing a larger area would have produced greater evanescent wave peak intensity. However, the length of fibre and embedded area was balanced to maximised signal, considering the extra fibre length required to run the fibres through a vacuum bag. It is believed that using a significantly larger fibre bundle (>50 fibres), would have protected some of the internal fibres from carbon fibre absorptions until the resin flowed through the bundle, resulting in scans with evanescent wave peaks. However, due to a limitation of remaining fibres, further experiments were not possible.

Despite the high noise level and absence of evanescent peaks, a sharp increase in intensity was produced as the panel heated up during the first 30 minutes as shown in Figure 88. This is due to the thermoplastic dissolving into the resin system. The light intensity remains relatively constant until 3 hours where the intensity starts to reduce. This reduction in intensity is due to the curing of the resin in which the RI and density increase. This demonstrates H3 fibres can be used as an intensity based cure monitoring sensor.

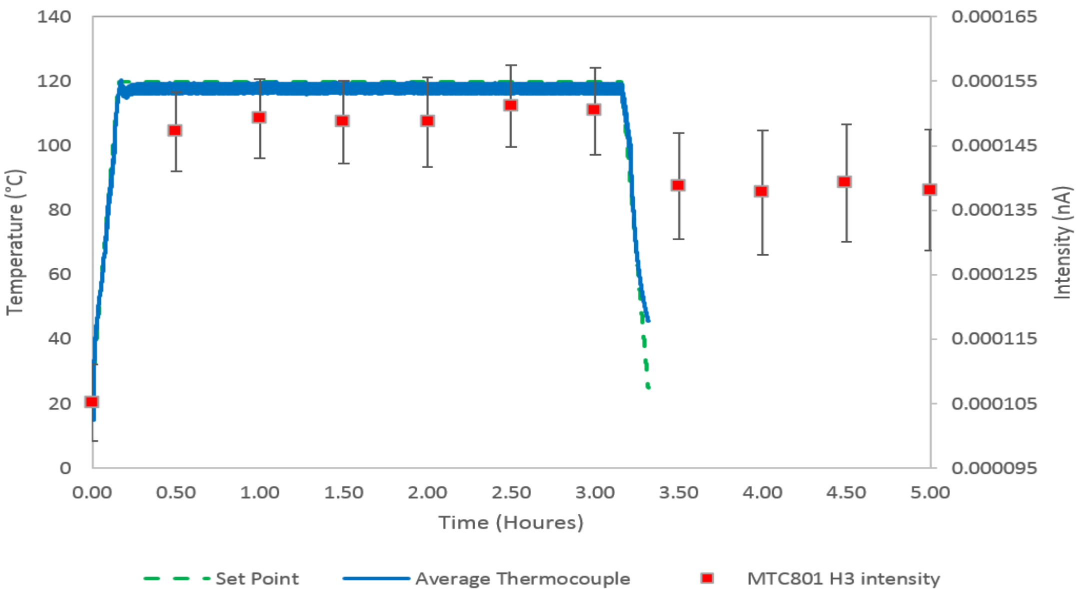

Figure 88 Optical Intensity from H3 fibres and temperature profile of MTC801 electrically cured panel under vacuum bag pressure. MTC801 H3 intensity is on the right y-axis which set point and average thermocouple temperature are on the left y-axis. Error bars are standard deviation of the data

4.10 H3 fibres suitability for cure monitoring

H3 fibres were first demonstrated as capable of FEWS using SFO. Throughout all of the FEWS work it was demonstrated as a requirement to have fine fibres <120 µm for a large enough evanescent wave to be sensed. This is beneficial due to reducing fibre diameter mismatch and the associated mechanical properties drop off as stated in Section 2.2.4.

H3 fibres have been demonstrated as capable of FEWS cure monitoring using MY721/DDS and 828/TETA monitoring using a range of peaks. The MY721/DDS system was monitored using the reduction in the 1970 nm NH_2 peak. The 828/TETA was monitored using a range of peaks. However, in cure monitoring thermoplastic toughened epoxy matrix carbon pre-pregs, the absorption of the carbon fibre prevented any peaks from being observed due to a high signal to noise ratio.

H3 fibres in all cases have shown a poor peak matching beyond the silica hydroxyl 2222-2299nm band limiting the maximum sensing capacity. The other dominant absorptions, mentioned in Section 4.7.2, did not affect any of the peak matching used within the resin systems. Consequently, they are not considered an issue for FEWS cure monitoring using H3 fibres and the current sensing window provides a suitable NIR window for cure monitoring of epoxy resins.

5 CONCLUSIONS

The aim of the project was to produce a high refractive index silicate glass suitable for near infra-red (NIR) fibre evanescent wave spectroscopy (FEWS) cure monitoring for a wide range of epoxy systems throughout the entire cure, whilst maintaining mechanical properties suitable for reinforcement.

Initial work focused on producing a range of resin and glass systems, for refractive index determination with ellipsometry. Ellipsometry was tested with a variety of differing RI glasses, demonstrating a range of ellipsometers have an error of ±0.015 RI when using direct measurement techniques on bulk samples. Ellipsometry has been demonstrated as an effective method of measuring the RI of a range of materials including polymers, preventing absorption of contact solutions in other techniques such as Abbé refractometry. A range of epoxy resin systems refractive indices were investigated as a minimum refractive index requirement for glass systems. The highest refractive index out of the epoxy resin systems was MY721 with DDS providing a minimum baseline for glass systems.

Two groups of glasses were produced: alkali containing and alkali-free silicate glasses. All glass systems were tested for being X-ray amorphous using XRD. The glass samples which did not instantly crystallise upon pouring were demonstrated as being X-ray amorphous. The X-ray amorphous glass systems demonstrated a higher RI than the epoxy systems.

Many of the alkali containing systems crystallised upon pouring, whilst both the sodium titanium silicate and lithium niobium silicate glasses formed glass blocks with suitable RI values for FEWS cure monitoring. However, during fibre drawing experiments both glasses crystallised, demonstrating a low separation between the fibre forming viscosity and liquidus.

Alkali-free silicates included two calcium aluminosilicate reinforcing fibre compositions modified with niobium to increase the refractive index, whilst a range of high dielectric constant compositions were investigated for suitability. The modified calcium aluminosilicate glasses produced bulk glasses; however, the modified E-glass composition possessed a RI too close to the epoxy RI borderline and the Ca:Al:Nb:Si glass possessed a liquidus temperature beyond the capability of the fibre drawing jig. High dielectric constant compositions produced suitable RI values and, in the case of H3 Pt glass, a separation between the liquidus and fibre forming.

The glass systems were thermally analysed using DTA. The most promising glasses were then analysed for liquidus and ($\mathrm{Log}_{10}(\eta/\mathrm{Poise})=3$) viscosity temperatures. The separation between the liquidus and ($\mathrm{Log}_{10}(\eta/\mathrm{Poise})=3$) viscosity temperatures were calculated to give the compositions ability to be fiberised.

An up drawing glass fibre jig was constructed and thermally characterised at differing cooling coil heights. It was found that none of the compositions could be drawn using the cooling coil dwelled at different heights for long periods of time. H3 fibres were produced using a time window when the coil was inserted until the melt became too cool.

The mechanical properties of the H3 system were characterised using an ultrasonic technique. This demonstrated that H3 glass had suitable mechanical properties to be used as a reinforcing fibre.

The H3 fibres were subsequently tested for suitability as a NIR FEWS sensor using sunflower oil. This demonstrated that small diameter fibres were required to produce an evanescent wave and the resulting absorption peaks. After the formation of evanescent peaks, H3 fibres were tested using MY721/DDS and 828/TETA liquid epoxy resin systems. In both cases peak intensities decreased with time, which were correlated with NIR baseline cuvette resin scans. In the case of MY721/DDS not enough data was gathered to give a comparison to kinetic isothermal DSC data of the resin systems. However, in the case of 828/TETA normalised peak high was compared to with kinetic isothermal DSC data of the resin system; but, due to high level of noise no clear kinetic data could be observed.

FEWS cure monitoring of electrically cured MTC801 carbon fibre/thermoplastic toughened epoxy pre-preg systems was investigated; however, due to carbon fibres intrinsic absorptions, signal to noise ratio was poor preventing any evanescent wave peaks from forming. However, intensity based cure monitoring was observed in pre-preg systems.

6 FUTURE WORK

To further develop the project beyond the successful demonstration of FEWS cure monitoring with high RI, H3 glass investigations should include:

- Investigate other high RI silicate glass systems with larger fibre forming windows
- Viscosity and liquidus measurement of remaining un-characterised glasses
- Further mechanical analysis of glasses
- Production of a down drawing glass fibre jig to enable easier fibre formation
- Investigation into the causes and phase identification of phase separated H3 Pt
- Further improvement to sensing equipment replacing current light source and the purchasing of an extended range InGaAs detector, improving signal to noise ratio
- Characterisation of the NIR fibre loss of the H3 fibres to investigate the limitation of the sensing FEWS system
- Increase H3 fibre bundle size and attempt different fibre end preparation to minimise signal to noise ratio
- Further investigate the issues with FEWS cure monitoring of electrically cured carbon fibre/epoxy pre-preg systems
- Intensity based damage sensing with H3 fibres to produce through-life monitoring of PMC.

Beyond the silicate glass family another glass family of potential interest is the oxynitride glasses. By adding nitrogen into the glass structure, a 3-coordinated nitrogen bond is formed between bridging silica tetrahedra increasing the elastic modulus [35]. Modulus and strength values have previously been attained for continuous "transparent" SiCaAiON fibres of 130 GPa and 3000-5000 MPa [130] potentially giving sensing fibres with mechanical properties on the low end of carbon fibres. Oxynitrides have RI values ranging from 1.45 Si-O to ~2 for Si-N [131]. They are non-trivial to manufacture, although it is possible they could be produced using standard reinforcing processing routes and then nitrided. This project could produce interesting glass systems with desirable chemical resistance [132], optical properties (NIR Transmission/RI) and mechanical properties for integration into PMC.

7 REFERENCES

1. Hull, D. and T.W. Clyne, *An introduction to composite materials*. 1996: Cambridge University Press.

2. Jones, R.M., *Mechanics Of Composite Materials*. 1998: Taylor & Francis.

3. Ellis, B., *Chemistry and technology of epoxy resins*. 1993: Blackie Academic & Professional.

4. Badcock, R.A. and G.F. Fernando, *An intensity-based optical fibre sensor for fatigue damage detection in advanced fibre-reinforced composites.* Smart Materials & Structures, 1995. **4**(4): p. 223-230.

5. Victrex *VICTREX® PEEK 150UF10* 2014.

6. González, M.G., J.C. Cabanelas and J. Baselga, *Applications of FTIR on Epoxy Resins–Identification, Monitoring the Curing Process, Phase Separation and Water Uptake.* Infrared Spectroscopy–Materials Science, Engineering and Technology, 2012.

7. Behzadi, S., *Role of Matrix Yield in Composite Performance*. 2006: University of Sheffield, Department of Engineering Materials.

8. Hara, O., *Curing Agents for Epoxy Resin* ThreeBond Technical News, 1990. **32**.

9. Burton, B.L., *Amine-Blushing Problems? No Sweat!*, in *Epoxy Formulators 2001*. 2001, Huntsman Corporation: The Woodlands, Texas. p. 17.

10. Powell, G.R., P.A. Crosby, G.F. Fernando, C.M. France, R.C. Spooncer and D.N. Waters. *Optical fiber evanescent-wave cure monitoring of epoxy resins*. 1996.

11. Crosby, P., G. Powell, G. Fernando, C. France, R. Spooncer and D. Waters, *In situ cure monitoring of epoxy resins using optical fibre sensors.* Smart materials and structures, 1996. **5**(4): p. 415.

12. Fernando, G.F. and B. Degamber, *Process monitoring of fibre reinforced composites using optical fibre sensors.* International Materials Reviews, 2006. **51**(2): p. 65-106.

13. White, S.R. and H.T. Hahn, *Cure Cycle Optimization for the Reduction of Processing-Induced Residual - Stresses in Composite Materials.* Journal of Composite Materials, 1993. **27**(14): p. 1352-1378.

14. Konstantopoulos, S., E. Fauster and R. Schledjewski, *Monitoring the production of FRP composites: A review of in-line sensing methods.* Express Polymer Letters, 2014. **8**(11): p. 823-840.

15. Schubel, P.J., R.J. Crossley, E.K.G. Boateng and J.R. Hutchinson, *Review of structural health and cure monitoring techniques for large wind turbine blades.* Renewable Energy, 2013. **51**: p. 113-123.

16. Powell, G.R., P.A. Crosby, D.N. Waters, C.M. France, R.C. Spooncer and G.F. Fernando, *In-situ cure monitoring using optical fibre sensors - a comparative study*. Smart Materials and Structures, 1998. **7**(4): p. 557.

17. Doyle, C., A. Martin, T. Liu, M. Wu, S. Hayes, P. Crosby, G. Powell, D. Brooks and G. Fernando, *In-situ process and condition monitoring of advanced fibre-reinforced composite materials using optical fibre sensors*. Smart materials and structures, 1998. **7**(2): p. 145.

18. Woerdeman, D.L., K.M. Flynn, J.P. Dunkers and R.S. Parnas, *The use of evanescent wave fluorescence spectroscopy for control of the liquid molding process*. Journal of reinforced plastics and composites, 1996. **15**(9): p. 922-943.

19. Zhou, G. and L.M. Sim, *Damage detection and assessment in fibre-reinforced composite structures with embedded fibre optic sensors - review*. Smart Materials & Structures, 2002. **11**(6): p. 925-939.

20. Fernando, G.F., *Fibre optic sensor systems for monitoring composite structures*. Reinforced Plastics, 2005. **49**(11): p. 41-49.

21. Feynman, R., *QED: The Strange Theory Of Light And Matter*. 1985: Universities Press (India) Pvt. Ltd.

22. Hecht, E., *Optics (4th Edition)*. 2001: Addison Wesley.

23. Callister, W.D., *Materials science and engineering: an introduction*. 2007: John Wiley and Sons.

24. Tilley, R.J.D., ed. *Understanding solids: the science of materials*. 2004, John Wiley & Sons.

25. Rauf, A., *Optical health monitoring of composites using self-sensing E-glass fibre waveguides*, in *Material Science and Engineering*. 2011, The Uniuversity of Sheffield: Sheffield. p. 179.

26. Seippel, R.G., *Fiber optics*. 1984: Reston Pub. Co.

27. Snyder, A.W. and J. Love, *Optical Waveguide Theory*. 1983: Springer.

28. Agrawal, G.P., *Fiber-optic communication systems*. 2002: Wiley-Interscience.

29. Rauf, A., R.J. Hand and S.A. Hayes, *Optical self-sensing of impact damage in composites using E-glass cloth*. Smart Materials and Structures, 2012. **21**(4).

30. Liu, H.W. and W.F. Su, *Fabrication of hybrid surface-modified titania-epoxy nanocomposite films*. J Phys Chem Solids, 2009. **70**(10): p. 5-5.

31. F T. Wallenberger, J.C.W., H Li and PPG Industries, Inc., *Glass fibers*, in *ASM Handbook Volume 21, Composites*. 2001, ASM international. p. 27-34.

32. David Hartman, M.E.G.a.D.M.M. *High Strength Glass Fibers*. 1996.

33. Kinsella, M., D. Murray, D. Crane, J. Mancinelli and M. Kranjc, *Mechanical properties of polymeric composites reinforced with high strength glass fibers*, in

Advancing Affordable Materials Technology, A. Falcone, et al., Editors. 2001, Soc Advancement Material & Process Engineering: Covina. p. 1644-1657.

34. Wallenberger, F.T. and P.A. Bingham, *Fiberglass and Glass Technology: Energy-Friendly Compositions and Applications*. 2009: Springer.

35. Shelby, J.E., *Introduction to Glass Science and Technology*. 2005: Royal Society of Chemistry.

36. Hayes, S., T. Liu, D. Brooks, S. Monteith, B. Ralph, S. Vickers and G.F. Fernando, *In situ self-sensing fibre reinforced composites.* Smart Materials & Structures, 1997. **6**(4): p. 432-440.

37. Silva, J.M.A., T.C. Devezas, A.P. Silva and J.A.M. Ferreira, *Mechanical characterization of composites with embedded optical fibers.* Journal of Composite Materials, 2005. **39**(14): p. 1261-1281.

38. Leng, J.S. and A. Asundi, *Real-time cure monitoring of smart composite materials using extrinsic Fabry-Perot interferometer and fiber Bragg grating sensors.* Smart Materials and Structures, 2002. **11**(2): p. 249.

39. Leng, J.S. and A. Asundi, *Real-time cure monitoring of smart composite materials using extrinsic Fabry-Perot interferometer and fiber Bragg grating sensors.* Smart Materials & Structures, 2002. **11**(2): p. 249-255.

40. Parsons, A.F., *Keynotes in organic chemistry*. 2003: Blackwell Science.

41. Takeda, N., Y. Okabe and T. Mizutani, *Damage detection in composites using optical fibre sensors.* Proceedings of the Institution of Mechanical Engineers Part G-Journal of Aerospace Engineering, 2007. **221**(G4): p. 497-508.

42. Chung, D.D.L., *Damage detection using self-sensing concepts.* Proceedings of the Institution of Mechanical Engineers Part G-Journal of Aerospace Engineering, 2007. **221**(G4): p. 509-520.

43. Kister, G., L. Wang, B. Ralph and G.F. Fernando, *Self-sensing E-glass fibres.* Optical Materials, 2003. **21**(4): p. 713-727.

44. Chung, D. and S. Wang, *Self-sensing of damage and strain in carbon fiber polymer-matrix structural composites by electrical resistance measurement.* Polymers and Polymer Composites, 2003. **11**(7): p. 515-525.

45. Wang, L., G. Kister, B. Ralph, J.D.R. Talbot and G.F. Fernando, *Conventional E-glass fibre light guides: self-sensing composite based on cladding.* Smart Materials & Structures, 2004. **13**(1): p. 73-81.

46. Wang, L., S. Malik, D. Harris and G.F. Fernando, *Self-sensing composites: in-situ cure monitoring - art. no. 64231F*, in *International Conference on Smart Materials and Nanotechnology in Engineering, Pts 1-3*, S.L.J.A.A.K. Du, Editor. 2007. p. F4231-F4231.

47. Wang, S. and D. Chung, *Self-sensing of flexural strain and damage in carbon fiber polymer-matrix composite by electrical resistance measurement.* Carbon, 2006. **44**(13): p. 2739-2751.

48. Hayes, S., T. Liu, D. Brooks, S. Monteith, B. Ralph, S. Vickers and G. Fernando, *In situ self-sensing fibre reinforced composites.* Smart materials and structures, 1997. **6**(4): p. 432.

49. Spectronic, T. *Basic UV-Vis theory, concepts and applications*. 2012 [cited 2014 20/10/14].

50. Primer, A., *Fundamentals of UV-visible spectroscopy.* Copyright Hewlett-Packard Company, Hewlett-Packard publication, (12-5965).

51. Ltd, M.U.K. *NIR Spectroscopy – a guide to near-infrared spectroscopic analysis of industrial manufacturing processes*. 2013. 44.

52. George, G.A., P. Cole-Clarke, N. St. John and G. Friend, *Real-time monitoring of the cure reaction of a TGDDM/DDS epoxy resin using fiber optic FT-IR.* Journal of Applied Polymer Science, 1991. **42**(3): p. 643-657.

53. Fouchal, F., J.A.G. Knight and P.M. Dickens, *Monitoring the polymerization of a diglycidyl ether bisphenol-A/2,2′-dimethyl-4,4′-methylenebis (cyclohexylamine) matrix with a Fourier transform infrared optical fibre sensor.* Proceedings of the Institution of Mechanical Engineers, Part L: Journal of Materials Design and Applications, 2004. **218**(4): p. 331-342.

54. Harrick, N.J., *Internal Reflection Spectroscopy*. 1967: Interscience Publishers.

55. Bailey, P., *Through life monitoring of composites using embedded evanescent wave spectroscopy*, in *Material Science and Engineering*. 2010, The University of Sheffield: Sheffield. p. 226.

56. Kapila, V., L. Kjerengtroen, W.M. Cross, F. Johnson and J.J. Kellar. *Strain monitoring by evanascent wave spectroscopy*. in *1999 Symposium on Smart Structures and Materials*. 1999. International Society for Optics and Photonics.

57. Murphy J. A, *Evanescent wave spectrscopy using multimode optical fibres*, in *Physics*. 1990, Dublin City: Ireland. p. 142.

58. Ungar, S., *Fibre optics: theory and applications*. 1990: John Wiley and Sons.

59. Bamford, C.R., *Colour Generation and Control in Glass*. 1977: Elsevier Scientific Publishing Company : distributors for the U.S. and Canada, Elsevier North-Holland.

60. Florence, J.M., C.C. Allshouse, F.W. Glaze and C.H. Hahner, *Absorption of near-infrared energy by certain glasses.* Journal of Research of the National Bureau of Standards, 1950. **45**(2): p. 121-128.

61. Kitamura, R., L. Pilon and M. Jonasz, *Optical constants of silica glass from extreme ultraviolet to far infrared at near room temperature.* Applied Optics, 2007. **46**(33): p. 8118-8133.

62. Carteret, C., *Mid- and Near-Infrared Study of Hydroxyl Groups at a Silica Surface: H-Bond Effect.* The Journal of Physical Chemistry C, 2009. **113**(30): p. 13300-13308.

63. Wang, L., S. Pandita, V.R. Machavaram, S. Malik, D. Harris and G.F. Fernando, *Characterisation of the cross-linking process in an E-glass fibre/epoxy composite using evanescent wave spectroscopy.* Composites Science and Technology, 2009. **69**(13): p. 2069-2074.

64. Bailey, P.B.S., S.A. Hayes, R.J. Hand and B. Zhang, *Chemical Monitoring of Composite Matrices by Evanescent Wave Spectroscopy*, in *Emboding Intelligence in Structures and Integrated Systems*, P. Vincenzini and F. Casciati, Editors. 2009, Trans Tech Publications Ltd: Stafa-Zurich. p. 297-302.

65. Anne, M.L., E.L. La Salle, B. Bureau, J. Tristant, F. Brochot, C. Boussard-Pledel, H.L. Ma, X.H. Zhang and J.L. Adam, *Polymerisation of an industrial resin monitored by infrared fiber evanescent wave spectroscopy.* Sensors and Actuators B-Chemical, 2009. **137**(2): p. 687-691.

66. Powell, G.R., *In-situ cure monitoring of epoxy resin systems* in *Department of Materials Engineering*. 1998, Brunel University p. 197.

67. Druy, M., L. Elandjian and W. Stevenson, *In Situ (Autoclave) Cure Monitoring of Composites with IR Transmitting Optical Fibers*, in *Review of Progress in Quantitative Nondestructive Evaluation*, D. Thompson and D. Chimenti, Editors. 1990, Springer US. p. 2039-2046.

68. Margalit, E., H. Dodiuk, E.M. Kosower and A. Katzir. *Infrared Fiber Evanescent Wave Spectroscopy For In-Situ Monitoring Of Chemical Processes*. 1989.

69. Johnson, F.J., W.M. Cross, D.A. Boyles and J.J. Kellar, *"Complete" system monitoring of polymer matrix composites.* Composites Part A: Applied Science and Manufacturing, 2000. **31**(9): p. 959-968.

70. Connell, M.E., W.M. Cross, T.G. Snyder, R.M. Winter and J.J. Kellar, *Direct monitoring of silane/epoxy interphase chemistry.* Composites Part A: Applied Science and Manufacturing (Incorporating Composites and Composites Manufacturing), 1998. **29**(5): p. 495-502.

71. Cross, W., W. Cross, L. Kjerengtroen and J. Kellar, *Interphase variation in silane-treated glass-fiber-reinforced epoxy composites.* Journal of adhesion science and technology, 2005. **19**(3-5): p. 279-290.

72. Cross, W.M., F. Johnson, J. Mathison, C. Griswold, J.J. Kellar and L. Kjerengtroen, *The effect of interphase curing on interphase properties and formation.* The Journal of Adhesion, 2002. **78**(7): p. 571-590.

73. Cossins S., Connell M. E., Cross B., Winter R. and Kellar J. J, *In Situ Near-IR Cure Monitoring of a Model Epoxy Matrix Composite.* Applied Spectroscopy, 1996. **50**(7): p. 900-905.

74. Wang, L., A. Tomlin, S. Pandita, V. Machavaram, R. Mahendran, E. Redmore, D. Harris, M. Paget and G. Fernando, *Effect of silane treatment of E-glass on the cross-linking kinetics of an epoxy resin.*

75. Wallenberger, F.T. and A. Smrcek, *The Liquidus Temperature; Its Critical Role in Glass Manufacturing (vol 1, pg 151, 2010).* International Journal of Applied Glass Science, 2010. **1**(3): p. 338-339.

76. Wallenberger, F.T., J.B. MacChesney, R. Naslain and H.D. Ackler, *Advanced Inorganic Fibers: Processes — Structure — Properties — Applications*. 2011: Kluwer Academic.

77. Krishan Kumar Chawla Chawla, K.K., *Fibers and fiber products*. 1998: Cambridge University Press.

78. Saleh, B.E.A. and M.C. Teich, *Fiber Optics*, in *Fundamentals of photonics*. 1991, John Wiley and Sons.

79. Kittel, C., *Introduction to solid state physics*. 2005: John Wiley and Sons.

80. Meeteen, G.H., *The Measurement, Instrumentation, and Sensors: Handbook - Chapter 61 Refractive Index Measurement*. 1999: CRC Press.

81. Mark, H.F. and J.I. Kroschwitz, *Encyclopedia of polymer science and engineering*. 1989: John Wiley and Sons.

82. Stanley, G.F., ed. *Refractometers Basic Principles*. 1 ed. Vol. 1. 1989, Bellingham and Stanley: Kent. 64.

83. Tompkins, H.G., *A user's guide to ellipsometry*. 1993: Academic Press.

84. Horbia *Stectroscopic Ellipsometry - User guide*. 2008.

85. Smith, C. *http://www.tcd.ie/Physics/Surfaces/ellipsometry2.php ,Trinity College Dublin*. 2012 [cited 2014 16th Oct].

86. Hayton, D.J. and T.E. Jenkins, *On the frustration of back-surface reflection from transparent substrates in ellipsometry*. Measurement Science and Technology, 2004. **15**(2): p. N17.

87. Synowicki, R.A., *Suppression of backside reflections from transparent substrates.* physica status solidi (c), 2008. **5**(5): p. 1085-1088.

88. Masuno, A., H. Inoue, J. Yu and Y. Arai, *Refractive index dispersion, optical transmittance, and Raman scattering of BaTi2O5 glass.* Journal of Applied Physics, 2010. **108**(6).

89. Masuno, A. and H. Inoue, *High Refractive Index of 0.30La2O3 - 0.70Nb2O5 Glass Prepared by Containerless Processing.* Applied Physics Express, 2010. **3**(Copyright (c) 2010 The Japan Society of Applied Physics): p. 102601.

90. Dumbaugh, W.H. and J.C. Lapp, *Heavy-Metal Oxide Glasses*. Journal of the American Ceramic Society, 1992. **75**(9): p. 2315-2326.

91. Fujino, S., H. Takebe and K. Morinaga, *Measurements of Refractive Indexes and Factors Affecting Dispersion in Oxide Glasses*. Journal of the American Ceramic Society, 1995. **78**(5): p. 1179-1184.

92. Dorosz, D., *Rare earth ions doped aluminosilicate and phosphate double clad optical fibres.* Bulletin of the Polish Academy of Sciences-Technical Sciences, 2008. **56**(2): p. 103-111.

93. Paul, A., *Chemical durability of glasses; a thermodynamic approach.* Journal of Materials Science, 1977. **12**(11): p. 2246-2268.

94. Enomoto, I., Y. Benino, T. Fujiwara and T. Komatsu, *Synthesis of nanocrystals in KNb(Ge,Si)O5 glasses and chemical etching of nanocrystallized glass fibers.* Journal of Solid State Chemistry, 2006. **179**(6): p. 1821-1829.

95. F.T. Wallenburg, J.C.W., H.Li *ASM Handbook, Volume 21 - Composites - Glass fibers*. 2001, ASM International. p. 27-34.

96. Komori, K., S. Yamakawa, S.S.C. Yamamoto, J. Naka and T. Kokubo, *Glass fiber forming composition, glass fibers obtained from the composition and substrate for circuit board including the glass fibers as reinforcing material*. 1992, Google Patents.

97. Aronne, A., E. Fanelli, V. Califano, A. Fragneto, A. Vergara, V.N. Sigaev and P. Pernice, *Structure and crystallization behavior of mixed potassium-lithium niobiosilicate glasses.* Journal of Non-Crystalline Solids, 2008. **354**(45–46): p. 5041-5046.

98. Dai, S., J. Wu, J. Zhang, G. Wang and Z. Jiang, *The spectroscopic properties of Er3+-doped TeO2–Nb2O5 glasses with high mechanical strength performance.* Spectrochimica Acta Part A: Molecular and Biomolecular Spectroscopy, 2005. **62**(1–3): p. 431-437.

99. Naka, J., S. Yamamoto, K. Komori, S. Yamakawa and T. Kokubo, *Development of glass fiber with high dielectric constant.* Journal of Non-Crystalline Solids, 1994. **177**(0): p. 420-426.

100. Sigaev, V.N., N.V. Golubev, S.Y. Stefanovich, T. Komatsu, Y. Benino, P. Pernice, A. Aronne, E. Fanelli, B. Champagnon, V. Califano, D. Vouagner, T.E. Konstantinova and V.A. Glazunova, *Second-order optical non-linearity initiated in Li2O–Nb2O5–SiO2 and Li2O–ZnO–Nb2O5–SiO2 glasses by formation of polar and centrosymmetric nanostructures.* Journal of Non-Crystalline Solids, 2008. **354**(10–11): p. 873-881.

101. Spierings, G., *The Influence of Nb2O5 on the properties of sodium borosilicate glass.* Journal of Non-Crystalline Solids, 1982. **47**(3): p. 421-425.

102. Todorovic, M. and L. Radonjic, *Lithium-niobate ferroelectric material obtained by glass crystallization.* Ceramics International, 1997. **23**(1): p. 55-60.

103. Srikumar, T., M.G. Brik, C. Srinivasa Rao, Y. Gandhi, D. Krishna Rao, V. Ravi Kumar and N. Veeraiah, *Spectral and fluorescent kinetics features of Nd3+ ion in Nb2O5, Ta2O5 and La2O3 mixed lithium zirconium silicate glasses.* Spectrochimica Acta Part A: Molecular and Biomolecular Spectroscopy, 2011. **81**(1): p. 498-503.

104. Vogel, W., *Glass chemistry*. 1994: Springer-Verlag.

105. Hamilton, E.H. and G.W. Cleek, *Properties of Sodium Titanium Silicate Glasses.* Journal of Research of the National Bureau of Standards, 1958. **61**(2): p. 89-94.

106. Schofield, J.M., P.A. Bingham and R.J. Hand, *The Immobilisation of a Chloride Containing Actinide Waste Surrogate in Calcium Aluminosilicate Glasses*, in *Environmental Issues and Waste Management Technologies in the Materials and Nuclear Industries Xii*, A. Cozzi and T. Ohji, Editors. 2009, Amer Ceramic Soc: Westerville. p. 69-80.

107. Penn, L.S. and H. Wang, *Epoxy Resins*, in *Handbook of Composites*, S.T. Peters, Editor. 1998, Springer US. p. 48-74.

108. Grainger, R., *Development of manufacturing processes for solid state self-healing composites*, in *Material Science*. 2014, The University of Sheffield: Sheffield.

109. Garcia, F.G., B.G. Soares, V.J.R.R. Pita, R. Sánchez and J. Rieumont, *Mechanical properties of epoxy networks based on DGEBA and aliphatic amines.* Journal of Applied Polymer Science, 2007. **106**(3): p. 2047-2055.

110. Wisanrakkit, G. and J.K. Gillham, *The glass transition temperature (Tg) as an index of chemical conversion for a high-Tg amine/epoxy system: Chemical and diffusion-controlled reaction kinetics.* Journal of Applied Polymer Science, 1990. **41**(11-12): p. 2885-2929.

111. Simmons, C.J. and O.H. El-Bayoumi, *Experimental techniques of glass science*. 1993: American Ceramic Society.

112. S. A. Hayes, A. D. Lafferty, G. Altinkurt, P. R. Wilson, M. Collinson and P. Duchene, *Direct electrical cure of carbon fiber composites.* Advance Manufacturing: Polymer and Composites Science, 2015. **0**(0): p. 1-8.

113. Cholake, S.T., M.R. Mada, R.K.S. Raman, Y. Bai, X.L. Zhao, S. Rizkalla and S. Bandyopadhyay, *Quantitative Analysis of Curing Mechanisms of Epoxy Resin by Mid- and Near-Fourier Transform Infra Red Spectroscopy.* Defence Science Journal, 2014. **64**(3): p. 314-321.

114. Li, L., Q. Wu, S. Li and P. Wu, *Study of the Infrared Spectral Features of an Epoxy Curing Mechanism.* Applied Spectroscopy, 2008. **62**(10): p. 1129-1136.

115. Di Pomponio, A. and A. Continenza, *Structural properties of alpha-quartz under high pressure and amorphization effects.* Physical Review B, 1993. **48**(17): p. 12558-12565.

116. Doremus, R.H., *Glass science*. 1973: John Wiley and Sons.

117. Malitson, I.H., *Interspecimen comparison of the refractive index of fused silica.* J. Opt. Soc. Am., 1965. **55**(10): p. 1205.

118. Optics, U. *SCHOTT BK7 Data Sheet*. [cited 2013 05/07].

119. Optics, U. *SCHOTT SK10 Data Sheet*. [cited 2013 05/07].

120. Optics, U. *SCHOTT SF10 Data Sheet*. [cited 2013 05/07].

121. Optics, U. *SCHOTT SF6 Data Sheet*. [cited 2013 05/07].

122. Optics, B. *M300 Single Monochromator: User guide*. 20.

123. Efimov, A.M., V.G. Pogareva and A.V. Shashkin, *Water-related bands in the IR absorption spectra of silicate glasses.* Journal of Non-Crystalline Solids, 2003. **332**(1–3): p. 93-114.

124. Efimov, A.M. and V.G. Pogareva, *Water-related IR absorption spectra for some phosphate and silicate glasses.* Journal of Non-Crystalline Solids, 2000. **275**(3): p. 189-198.

125. Gonzalez, C., J.M. Resa, J. Lanz and M.A. Fanega, *Excess molar volumes and refractive indices of mixtures formed by acetates with sunflower oil at different temperatures.* Journal of the American Oil Chemists Society, 2002. **79**(6): p. 539-542.

126. Min, B.G., Z.H. Stachurski, J.H. Hodgkin and G.R. Heath, *Quantitative-Analysis of the Cure Reaction of DGEBA DDS Epoxy-Resins without and with Thermoplastic Polysulfone Modifier using Near-Infrared spectroscopy.* Polymer, 1993. **34**(17): p. 3620-3627.

127. Musto, P., E. Martuscelli, G. Ragosta and P. Russo, *The curing process and moisture transport in a tetrafunctional epoxy resin as investigated by FT-NIR spectroscopy.* High Performance Polymers, 2000. **12**(1): p. 155-168.

128. Pandita, S.D., L. Wang, R.S. Mahendran, V.R. Machavaram, M.S. Irfan, D. Harris and G.F. Fernando, *Simultaneous DSC-FTIR spectroscopy: Comparison of cross-linking kinetics of an epoxy/amine resin system.* Thermochimica Acta, 2012. **543**: p. 9-17.

129. Norteman, W.E. and F.H. Lohman, *Determination of Primary and Secondard Aliphatic Amines by Near-Infra-red Spectrophotometry.* Spectrochimica Acta, 1962. **18**(6): p. 884-884.

130. Iba, H., T. Naganuma, K. Matsumura and Y. Kagawa, *Fabrication of transparent continuous oxynitride glass fiber-reinforced glass matrix composite.* Journal of Materials Science, 1999. **34**(23): p. 5701-5705.

131. Landgrebe, A.R., K.B. Sundaram, E.S.D. Science, T. Division and E.S.H.T.M. Division, *Silicon Nitride and Silicon Dioxide Thin Insulating Films: Proceedings of the Sixth International Symposium*. 2001: Electrochemical Society.

132. Das, T., *Oxynitride glasses—An overview.* Bulletin of Materials Science, 2000. **23**(6): p. 499-507.

8 APPENDICES

8.1 Appendix A – 1

SiO_2	CaO	SrO	BaO	TiO_2	ZrO_2	Nb_2O_5	Tan δ (1GHz)	ϵ (1GHz)	T fibre 2.5 Poise °C	T Liq °C	ΔT
60	10	10	20	-	-	-	35	9.4		1228	
60	7.5	7.5	15	8.2	1.8	-	25	9.4		1144	
50	10	10	20	8.2	1.8	-	33	11		>1300	
40	10	10	20	16.5	3.5	-	37	12.8		>1300	
30	7.5	7.5	15	32.8	7.2	-	40	16.3		>1300	
55	7.5	7.5	15	12.4	2.6	-	29	10.3	1119	1168	-49
55.41	7.56	7.56	15.11	11.18	2.42	0.76	30	10.3	1122	1139	-17
55.85	7.61	7.61	15.23	10.05	2.13	1.52	30	10.3	1121	1117	4
56.27	7.67	7.67	15.35	8.9	1.84	2.3	28	10.5	1125	1126	-1
56.71	7.73	7.73	15.46	7.63	1.65	3.09	27	10.6	1129	1200	-71
50	7.5	7.5	15	16.5	3.5	-	29	11.4	1098	1180	-82
50.5	7.58	7.58	15.15	14.95	3.23	1.01	29	11.4	1098	1132	-34
51.02	7.65	7.65	15.31	13.47	2.86	2.04	30	11.5	1099	1100	-1
51.56	7.73	7.73	15.46	11.96	2.47	3.09	29	11.6	1098	1067	31
52.08	7.81	7.81	15.63	10.31	2.19	4.17	28	11.6	1097	1075	22
52.64	7.89	7.89	15.79	8.63	1.89	5.26	30	11.6	1098	1120	-22
40	7.5	7.5	15	24.7	5.3	-	34	13.7	1051	1180	-129
40.4	7.58	7.58	15.15	23.33	4.95	1.01	34	13.7	1052	1165	-113
40.82	7.65	7.65	15.31	21.84	4.69	2.04	35	13.9	1050	1141	-91
41.24	7.73	7.73	15.46	20.41	4.33	3.09	34	13.9	1047	1122	-75
41.67	7.81	7.81	15.62	18.85	4.06	4.17	35	14.1	1042	1100	-58
42.11	7.89	7.89	15.79	17.37	3.68	5.26	37	14.3	1048	1085	-37

8.2 Appendix A – 2

SiO_2	CaO	SrO	BaO	TiO_2	ZrO_2	Nb_2O_5	MgO	CeO_2	ZnO	La_2O_3	Ta_2O_5	Al_2O_3	Li_2O	Na_2O	K_2O	ϵ (1MHz)	ϵ (1GHz)	T fibre 2.5 Poise °C	TLiq °C	ΔT
56.56	9.25	6.17	15.42	8.02	1.75	1.54	0.00	0.00	0.00	0.00	0.00	1.29	0.00	0.00	0.00	10.10	10.10	1199	1085	114
52.36	9.42	6.28	15.71	9.53	1.99	3.14	0.00	0.00	0.00	0.00	0.00	1.57	0.00	0.00	0.00	11.00	11.00	1166	1060	106
50.79	9.52	6.35	15.87	9.63	2.01	3.17	0.00	0.00	0.00	0.00	0.00	2.65	0.00	0.00	0.00	11.00	11.00	1160	1057	103
52.36	7.12	7.12	14.03	12.04	2.62	3.14	0.00	0.00	0.00	0.00	0.00	1.57	0.00	0.00	0.00	11.00	11.00	1164	1064	100
52.08	9.38	6.25	15.63	10.31	2.19	3.13	0.00	0.00	0.00	0.00	0.00	1.04	0.00	0.00	0.00	11.20	11.20	1154	1054	100
52.22	9.40	6.27	15.67	9.92	2.09	3.13	0.00	0.00	0.00	0.00	0.00	1.31	0.00	0.00	0.00	11.10	11.10	1162	1063	99
52.22	7.83	7.83	15.67	9.92	2.09	3.13	0.00	0.00	0.00	0.00	0.00	1.31	0.00	0.00	0.00	11.10	11.10	1160	1065	95
52.22	7.21	7.21	14.31	12.01	2.61	3.13	0.00	0.00	0.00	0.00	0.00	1.31	0.00	0.00	0.00	11.00	11.00	1158	1070	88
51.56	7.73	7.73	15.46	11.91	2.52	3.09	0.00	0.00	0.00	0.00	0.00	0.00	0.00	0.00	0.00	11.6	11.6	1153	1070	83
51.55	9.28	6.19	15.46	11.91	2.52	3.09	0.00	0.00	0.00	0.00	0.00	0.00	0.00	0.00	0.00	11.5	11.5	1149	1066	83
51.83	7.77	7.77	15.54	11.11	2.35	3.63	0.00	0.00	0.00	0.00	0.00	0.00	0.00	0.00	0.00	11.6	11.6	1150	1071	79
51.29	7.69	7.69	15.38	12.70	2.69	2.56	0.00	0.00	0.00	0.00	0.00	0.00	0.00	0.00	0.00	11.5	11.5	1155	1080	75
53.83	9.54	6.36	15.89	9.77	2.07	2.54	0.00	0.00	0.00	0.00	0.00	0.00	0.00	0.00	0.00	11	10.9	1164	1096	68
52.35	7.86	7.85	15.71	9.51	2.01	4.71	0.00	0.00	0.00	0.00	0.00	0.00	0.00	0.00	0.00	11.7	11.7	1147	1080	67
51.95	7.79	7.79	15.59	11.95	2.60	2.34	0.00	0.00	0.00	0.00	0.78	0.00	0.00	0.00	0.00	11.2	11.2	1153	1090	63
51.55	7.73	7.73	15.46	11.04	3.40	3.09	0.00	0.00	0.00	0.00	0.00	0.00	0.00	0.00	0.00	11.2	11.2	1152	1090	62

55.84	7.62	7.61	15.23	10.05	2.13	1.52	0.00	0.00	0.00	0.00	0.00	0.00	0.00	0.00	0.00	10.4	10.4	1175	1117	58
51.00	7.66	7.66	15.31	13.47	2.86	2.04	0.00	0.00	0.00	0.00	0.00	0.00	0.00	0.00	0.00	11.5	11.5	1151	1095	56
56.26	7.68	7.67	15.35	8.90	1.84	2.30	0.00	0.00	0.00	0.00	0.00	0.00	0.00	0.00	0.00	10.5	10.5	1180	1126	54
51.95	6.75	6.75	13.51	15.43	3.27	1.04	4.16	0.00	0.00	0.00	0.00	0.00	0.00	0.00	0.00	11.2	11.2	1149	1095	54
50.00	7.50	7.50	15.00	14.85	3.15	2.00	0.00	0.00	0.00	0.00	0.00	0.00	0.00	0.00	0.00	12.3	12.3	1136	1085	51
49.00	7.30	7.30	14.60	14.49	3.40	3.90	0.00	0.00	0.00	0.00	0.00	0.00	0.00	0.00	0.00	12.3	12.3	1136	1085	51
49.97	7.45	7.45	14.89	14.79	3.47	1.99	0.00	0.00	0.00	0.00	0.00	0.00	0.00	0.00	0.00	11.8	11.8	1157	1112	45
53.83	7.95	7.95	15.89	9.77	2.07	2.54	0.00	0.00	0.00	0.00	0.00	0.00	0.00	0.00	0.00	10.9	10.9	1168	1124	44
56.04	7.65	7.64	15.28	9.46	2.01	1.92	0.00	0.00	0.00	0.00	0.00	0.00	0.00	0.00	0.00	10.5	10.4	1173	1130	43
50.01	7.49	7.49	15.01	14.85	3.15	2.00	0.00	0.00	0.00	0.00	0.00	0.00	0.00	0.00	0.00	11.9	11.8	1145	1102	43
49.99	7.51	7.50	15.00	14.85	3.15	2.00	0.00	0.00	0.00	0.00	0.00	0.00	0.00	0.00	0.00	11.5	11.5	1158	1120	38
51.95	7.17	7.17	14.23	11.95	2.60	3.12	0.00	0.00	0.00	1.30	0.00	0.00	0.00	0.00	0.00	11.4	11.4	1145	1115	30
51.55	7.11	7.11	14.12	11.86	2.58	3.09	0.00	2.58	0.00	0.00	0.00	0.00	0.00	0.00	0.00	11.50	11.50	1145	1118	27
51.55	7.11	7.11	14.12	11.86	2.58	3.09	0.00	0.00	2.58	0.00	0.00	0.00	0.00	0.00	0.00	11.10	11.10	1136	1130	6
52.88	7.93	7.93	15.86	7.88	1.69	5.82	0.00	0.00	0.00	0.00	0.00	0.00	0.00	0.00	0.00	11.70	11.70	1142	1140	2
51.55	7.01	7.01	13.81	11.86	2.58	3.09	0.00	0.00	0.00	0.00	0.00	0.00	1.03	1.03	1.03	11.10	11.10	1080	1078	2
41.88	9.42	6.28	15.71	18.15	3.84	4.71	0.00	0.00	0.00	0.00	0.00	0.00	0.00	0.00	0.00	14.10	14.10	1090	1089	1
51.55	9.28	6.19	15.46	2.58	0.00	0.00	11.86	0.00	0.00	0.00	0.00	3.09	0.00	0.00	0.00	10.60	10.60	1176	1203	-27
50.00	7.50	7.50	15.00	16.50	3.50	0.00	0.00	0.00	0.00	0.00	0.00	0.00	0.00	0.00	0.00	11.00	11.00	1147	1204	-57
40.00	7.50	7.50	15.00	23.00	7.00	0.00	0.00	0.00	0.00	0.00	0.00	0.00	0.00	0.00	0.00	13.50	13.50	1077	1214	-137

8.3 Appendix B

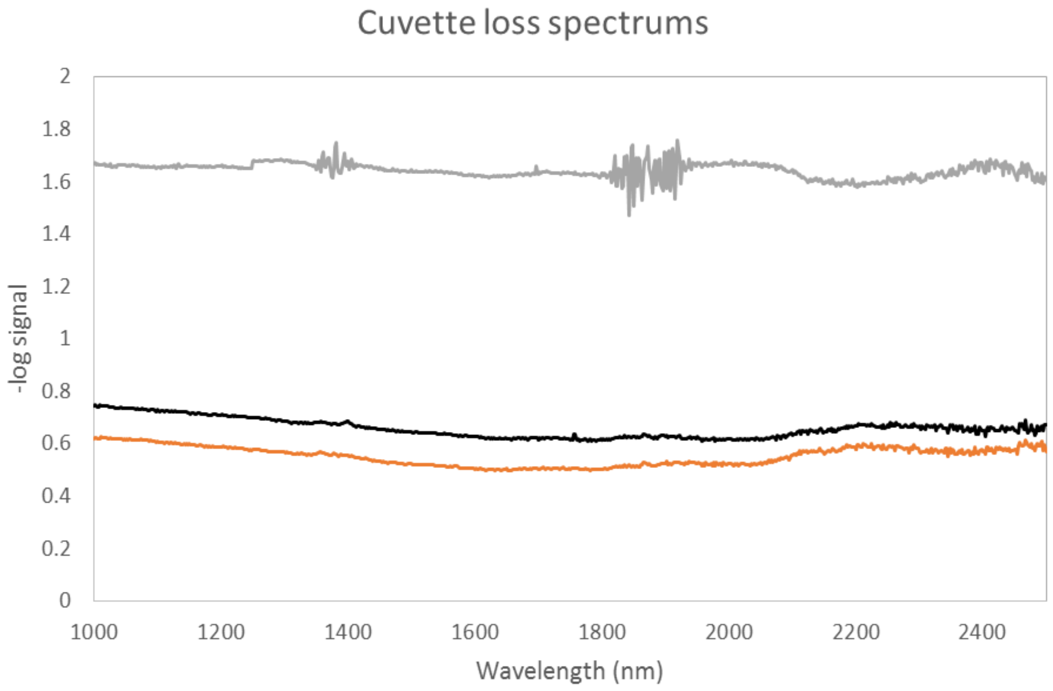

8.4 Appendix C

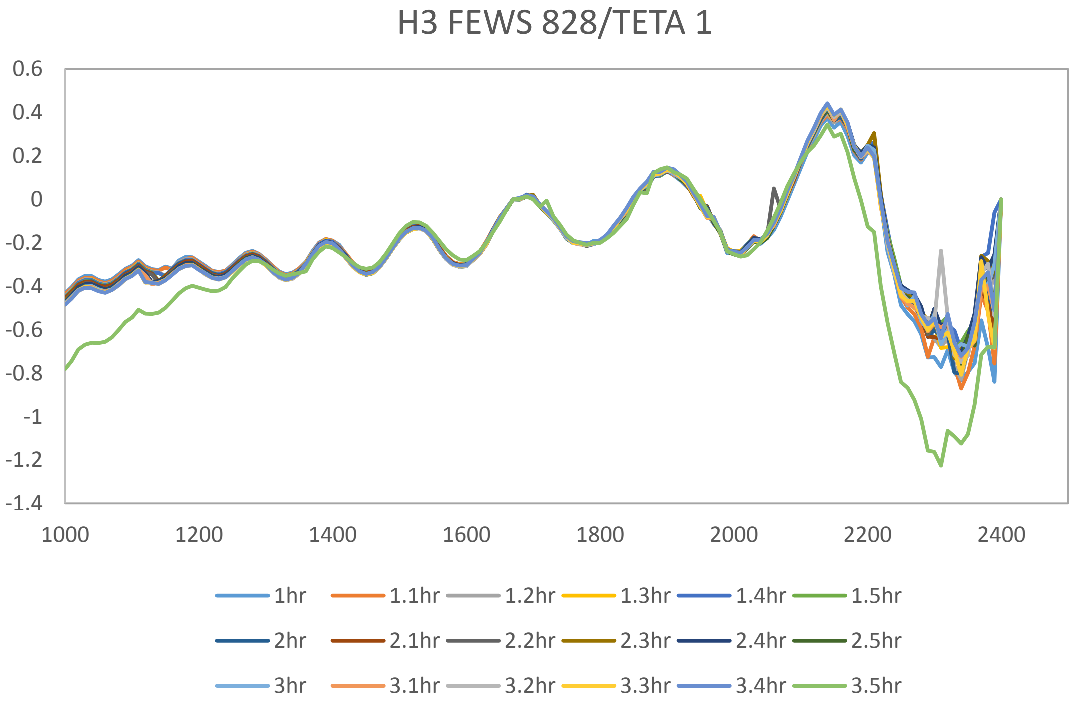

H3 FEWS 828/TETA 2

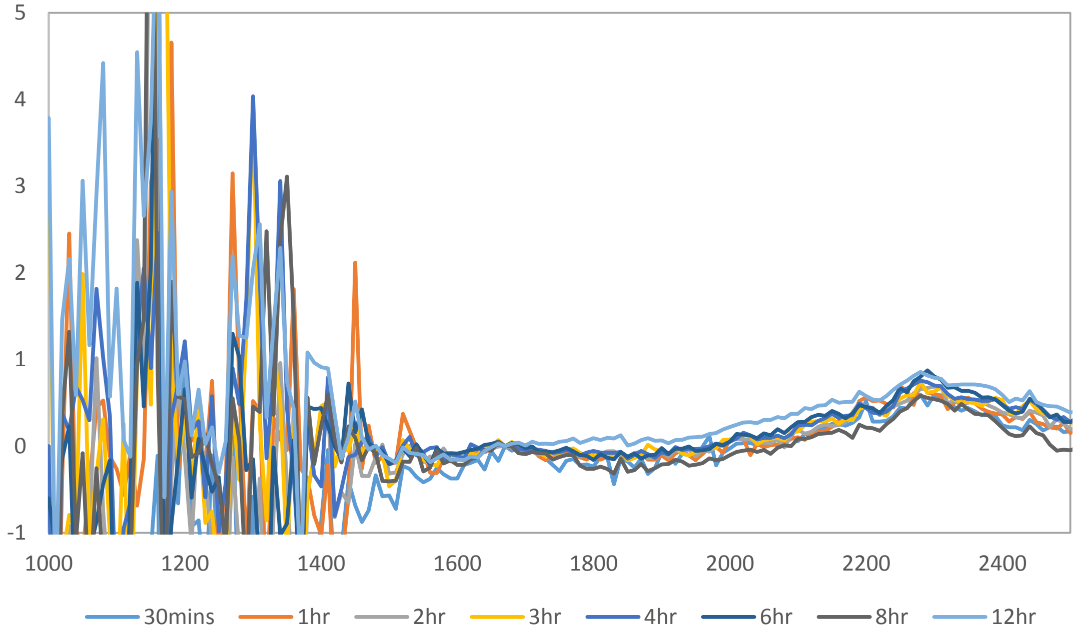

H3 FEWS 828/TETA 3